UNIVERSITY OF LIVERPOOL

Epitaxy on quasicrystals: metals, semi-metals and molecules

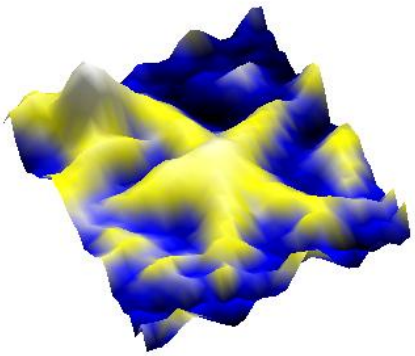

Thesis submitted in accordance with the requirements of the University of Liverpool for the degree of Doctor in Philosophy

By Kirsty M. Young

November 2012

Abstract

The research described in this doctoral thesis involves the experimental investigation of heteroepitaxial growth at quasicrystal surfaces. The aim is to further extend fundamental surface growth studies to such complex intermetallics and to form high quality, single-component quasicrystalline layers. The experiments included involve deposition of Cu, Bi, pentacene and carbon–60 on quasiperiodic surfaces. The formation and structure of these adsorbate layers on different quasicrystalline surfaces are analysed with surface science techniques.

X–ray photoelectron spectroscopy measurements confirmed complete first layer followed by island growth mode of Bi on *i*–Al–Pd–Mn. Upon heating of the layer, stable monolayer and submonolayer coverages were observed supporting a strongly bound layer and the initial nucleation of stable, pentagonal clusters. Low energy electron diffraction patterns of the multilayer show that the {111}–rhombohedral islands are rotationally epitaxial with the substrate while the {012}–rhombohedral islands are not. The atomic structure and size of islands are measured with scanning tunnelling microscopy. A higher flux of Bi is found to inhibit the morphological transformation of the thin film to {111}–rhombohedral islands.

Scanning tunnelling microscopy of pentacene adsorption on *i*–Al–Pd–Mn found the molecules to be chemisorbed in a disordered, flat layer at the surface. The same arrangement of molecules is observed for adsorption on a quasicrystalline Bi monolayer, while ordered rows of molecules are evidenced on the flatter {012}–rhombohedral Bi islands.

Pentacene formed incommensurate layers – composed of dense, periodic rows, – on the aperiodic vicinal Cu structure on *i*–Al–Pd–Mn. DFT calculations of naphthalene adsorption at the surface supported and detailed the adsorption sites of the acene along the rows.

Cu exhibited 3-D cluster growth on *i*–Ag–In–Yb and on a pseudomorphic Bi layer at this surface. The Cu absorbs on the truncated, rhombic triacontrahedral clusters leading to some initial ordering. A pentacene monolayer on *i*–Ag–In–Yb successfully formed the first epitaxial, quasiperiodic molecular overlayer to be observed experimentally. The layer is composed of many clusters with pentagonal symmetry and a large degree of orientational alignment along high symmetry directions of the substrate is observed. C_{60} grew in a disordered fashion on a Bi monolayer at *i*–Ag–In–Yb, although some local partial C_{60} clusters possessing 5– and 10–fold symmetry were observed at low submonolayer coverage.

Acknowledgments

The last three years have been a brilliant experience in which I have grown overall, personally and professionally. Foremost, I would like to thank my supervisor, Prof. Ronan McGrath for his calm, valuable guidance and the opportunity to carry out my research. It has been a pleasure to learn from and work with Dr. Hem Raj Sharma and Dr. Joseph Smerdon, who are both very dedicated scientists. I am grateful for other members of my research group for being outstanding colleagues - Dr. Joseph Parle, Peter Nugent, Ian McLeod and several masters and bachelor undergraduate degree project students. I would also like to thank all the staff and students at the Surface Science Research Centre and Department of Physics, University of Liverpool for helping to provide such a good work environment. I am thankful for the advice and help of Dr. Sam Haq, Dr. Vinod Dhanak and Paul Unsworth, who are most proficient with UHV systems.

I would like to thank the UK Engineering and Physical Sciences Research Council (EPSRC) for the financial support. It has been an honour to be part of the international community of research into aperiodic crystals for the past several years. I have immensely enjoyed meeting many people at summer schools and conferences that I have attended on an international and national level. It has been a joy to partake in experiments abroad at the ESRF, France (beamlines ID32 and BM28) and ASTRID, University of Aarhus, Denmark. Furthermore, I would like to extend my thanks to the European network of Complex Metallic Alloy and Compounds for organising intellectually stimulating meetings and schools.

I am most grateful for my friends and family in Liverpool and further afield. I would like to thank Yan-Jie for listening to and supporting me while I wrote my thesis. I am very thankful for my loving father, Ken, for his constant support. Finally, I would like to dedicate this doctoral thesis to my late mother, Carol, who was very proud of everything her family achieved.

Kirsty Moray Young, 2012

Contents

1 Introduction **1**

2 Quasicrystals and their surfaces **3**

2.1 Introduction to quasicrystals . . . 3
2.2 Crystallography basics . . . 5
2.3 Aperiodic order and the golden mean . . . 8
2.4 Penrose tiling . . . 9
2.5 Higher dimensional crystallography . . . 10
2.6 Approximants . . . 12
2.7 Cluster models . . . 13
2.8 Icosahedral quasicrystals . . . 14
2.8.1 Icosahedral Aluminium–Palladium–Manganese (i–Al–Pd–Mn) quasicrystal . . . 14
2.8.2 Icosahedral Silver–Indium–Ytterbium (i–Ag–In–Yb) Quasicrystal . . . 18

3 Adsorption and growth on quasicrystal surfaces **22**

3.1 Growth of thin films at surfaces . . . 22
3.2 Adsorption studies on quasicrystal surfaces . . . 25
3.3 Pentacene . . . 30
3.3.1 Pentacene thin film studies . . . 32
3.4 carbon–60 . . . 34
3.4.1 C_{60} thin film studies . . . 34

4 Experimental Methodology **37**

4.1 UHV chamber . . . 38
4.2 Vacuum pumps . . . 38
4.2.1 Roughing/Backing Pumps . . . 38
4.2.2 Turbomolecular pump . . . 39
4.2.3 Titanium sublimation pump (TSP) . . . 39
4.2.4 Ion pump . . . 40
4.3 Pressure gauges . . . 40
4.4 Mass spectrometer . . . 41
4.5 Instrumentation . . . 42
4.5.1 X–ray photoelectron spectroscopy . . . 42

4.5.2 Low energy electron diffraction . . . 46
4.5.3 Scanning tunnelling microscopy . . . 51
4.6 Sample preparation . . . 54
4.7 In-situ evaporation . . . 57

5 Growth of Bi on the fivefold surface of *i*–Al–Pd–Mn 58
5.1 Introduction . . . 58
5.2 Experimental details . . . 60
5.3 Results . . . 62
5.4 Discussion . . . 69
5.5 Summary . . . 71

6 Pentacene adsorption on the fivefold surface of *i*–Al–Pd–Mn 72
6.1 Introduction . . . 72
6.2 Experimental details . . . 72
6.3 Results . . . 73
6.3.1 Pentacene growth on *i*–Al–Pd–Mn . . . 73
6.3.2 Pentacene growth on the quasicrystalline monolayer and nanoscale crystalline islands of Bi on *i*–Al–Pd–Mn . . . 76
6.4 Discussion . . . 77
6.5 Summary . . . 80

7 Pentacene adsorption on the uniaxially aperiodic Cu multilayer formed on *i*–Al–Pd–Mn 81
7.1 Introduction . . . 81
7.2 Experimental details . . . 81
7.3 DFT calculation details . . . 81
7.4 Results . . . 82
7.4.1 Experiment results . . . 82
7.4.2 Theoretical results . . . 87
7.5 Discussion . . . 92
7.6 Conclusions . . . 94

8 Metal adsorption on the fivefold surface of *i*–Ag–In–Yb 95
8.1 Introduction . . . 95
8.2 Experimental details . . . 95
8.3 Bi growth on *i*–Ag–In–Yb . . . 97

8.3.1 Results . . . 97
8.3.2 Discussion and conclusions . . . 98
8.4 Cu growth on *i*-Ag–In–Yb and on Bi/*i*–Ag–In–Yb . . . 100
8.4.1 Introduction . . . 100
8.4.2 Results . . . 100
8.4.3 Discussion . . . 105
8.4.4 Conclusions . . . 107

9 Molecular adsorption studies on the fivefold surface of *i*–Ag–In–Yb 108
9.1 Introduction . . . 108
9.2 Experimental Details . . . 108
9.3 Pentacene growth on *i*–Ag–In–Yb . . . 108
9.3.1 Introduction . . . 108
9.3.2 Results . . . 109
9.3.3 Discussion . . . 117
9.3.4 Summary . . . 118
9.4 C_{60} growth on the quasicrystalline Bi monolayer on *i*–Ag–In–Yb . . . 118
9.4.1 Introduction . . . 118
9.4.2 Results . . . 119
9.4.3 Conclusions . . . 120

10 Summary and future work 122

1 Introduction

The study of surface physics is of utmost importance for the development of materials and devices with new sets of mechanical, electrical and thermodynamic properties and in the discovery of new quantum phenomena. The surface of a solid is where crystal growth occurs and therefore can be exploited to create artificial thin films and structures that cater for our industrial needs.

The discovery of complex intermetallics – such as quasicrystals – provided many new challenges for researchers. The surfaces of quasicrystals and epitaxial thin films possess properties of technological interest. Additionally, it is difficult to probe the complicated bulk structure of quasicrystals and therefore bulk terminated surfaces provide an easier way to observe this structure. Epitaxial growth studies at these heterogeneous surfaces can examine the formation of quasicrystals, study the factors governing epitaxial growth and develop the understanding of the self–assembly of nanostructures.

This thesis has 3 main themes:

- ◇ The study of the different growth modes of a semi-metal, a noble metal and a number of molecules at the surfaces of two different icosahedral quasicrystals.

- ◇ The formation of quasiperiodic molecular overlayers using different molecules and surfaces.

- ◇ The effect of an interfacial quasicrystalline Bi monolayer on the arrangement of metals and molecules at a quasicrystal surface.

The research involves deposition in ultra-high vacuum conditions. The interaction, growth and structure of Cu, Bi, pentacene and carbon-60 at quasiperiodic surfaces are investigated. The techniques of scanning tunnelling microscopy, low energy electron diffraction and x-ray photoelectron spectroscopy are utilised to achieve this.

Chapter 2 provides an introduction to quasicrystals. Some crystallographic concepts are introduced and the structural descriptions and properties of quasicrystals are reviewed. The bulk and surface structure of the two quasicrystals used for experimental investigations in this thesis are described. In chapter 3 heteroepitaxial

growth studies at quasicrystal surfaces to date are reviewed. The two molecules deposited at surfaces in this thesis (pentacene and carbon-60) are introduced, and previous thin film studies involving them are discussed. UHV studies and experimental equipment are described in Chapter 4.

The results of the growth of Bi on the fivefold surface of *i*–Al–Pd–Mn investigated with XPS, LEED and STM are presented and discussed in Chapter 5. The results of pentacene adsorption on *i*–Al–Pd–Mn quasicrystal and on the Bi film of Chapter 5 are presented in Chapter 6. Chapter 7 shows the results of pentacene adsorption on the uniaxially aperiodic Cu multilayer formed on the *i*–Al–Pd–Mn.

Chapter 8 and 9 present the results of several epitaxial growth studies involving the *i*–Ag–In–Yb quasicrystal. An STM study of Bi and Cu growth at this surface is presented. Pentacene and carbon–60 growth on a pseudomorphic Bi monolayer on this surface are investigated. An overall summary of the scientific results and the proposal of future research is given in Chapter 10.

2 Quasicrystals and their surfaces

2.1 Introduction to quasicrystals

Quasi-periodic crystals – or quasicrystals,– are intermetallic alloys that possess long-range atomic ordering but with a unit cell which is infinite as there is no translational invariance of the structure. The high degree of ordering in quasicrystals is apparent through their diffraction patterns, which display intense, distinct spots. These observed patterns are usually of classically forbidden symmetry; i.e. not allowed by any Bravais lattice characterization in traditional crystallography. Such complex intermetallics can be considered as a third state of solid matter – the others being crystalline and amorphous.

Quasicrystals were first discovered in 1982 by Dan Shechtman in an electron microscopy study of a rapidly solidified alloy of aluminium (Al) and 14% manganese (Mn) [1]. The result was a metastable quasicrystal displaying a diffraction pattern with ten–fold rotational symmetry. For a few years thereafter some scientists dismissed quasicrystals as repeated, twinned crystal arrangements but further experiments showed the unusual symmetry of the quasicrystal is due to an icosahedral form of atomic arrangement [2]. The discovery and recognition of quasicrystals as a form of highly–ordered solid led to the redefinition of a crystal from 'a solid having translational invariance' to 'any solid having an essentially discrete diffraction pattern'. It also promoted renewed interest in other types of aperiodic crystals (modulated structures and composites) and led to Shechtman being awarded the Nobel Prize in Chemistry in 2011.

Quasicrystals are found in alloys of specific stoichiometry and hence it is difficult to predict their compositions. The binary transition metal–based quasicrystals are stabilised by the addition of a third or more constituent metals [3]. To date there are over one hundred binary, ternary and quaternary stable quasicrystal systems; samples of 5–, 8–, 10– and 12– fold rotational symmetry have been synthesised (8– and 12–fold examples are meta-stable) [4–6]. The high order of symmetry can be macroscopically observable in the grain morphology of samples – see Figure 1. In 2009, natural micrometre sized quasicrystal grains were found in the mineral khatyrkite [7] further re-inforcing the idea that the ground state of matter is not always a periodic crystalline arrangement. It was later suggested that this sample was of extraterrestrial origin [8].

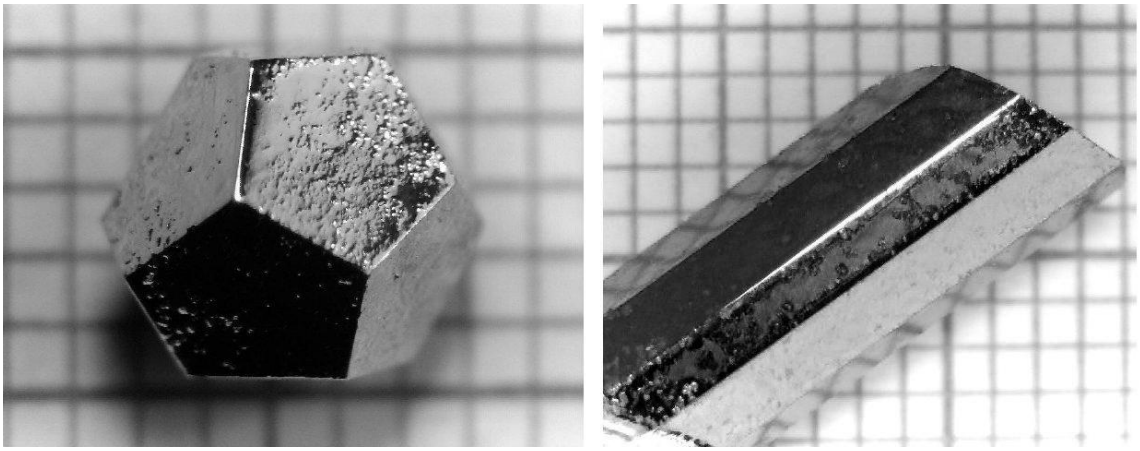

Figure 1: Macroscopic morphology of as–grown quasicrystal samples. Left: single grain of the *i*–Zn–Mg–Ho quasicrystal Right: *d*–Al–Ni–Co quasicrystal ingot. Courtesy of cmp.physics.iastate.edu/canfield/photos.html.

Quasicrystals have been found to have unusual material properties for an alloy of their constituent elements. These properties include: low electrical and thermal conductivity ($\sigma \approx 10^2\ \Omega^{-1}cm^{-1}$, $\kappa \approx 3\ W/mK$), a negative temperature coefficient of resistance, high hardness ($H_v \approx 700$), brittleness, corrosion and oxidation resistance and a low coefficient of friction ($\mu \approx 0.2$). The poor electrical conduction behaviour and the stabilisation mechanism of quasicrystals is due to a minimum in the electronic density of states observed at the Fermi level termed the 'pseudogap'. The origin of the pseudogap is strong electron scattering by the structure leading to hybridisation of the electronic states at the atomic cluster level.

Potential applications of quasicrystals are hard non–stick coatings, frictionless coatings for combustion engines, reinforced composite materials, solar–selective absorbers and hydrogen storage. Previous patents include the use of quasicrystal precipitates to strengthen surgical instruments (Sandvik Materials Technology©) and for hard, non–stick coatings in frying pans (Cybernox®) [9]. One of the main questions posed in relation to quasicrystals is whether their anomalous properties are a result of their complex chemical nature or their aperiodic order. In this thesis, the surfaces of quasicrystals provide a complex template to explore reactivity and the epitaxial growth of adsorbing particles.

To better understand aperiodic structures some basic crystallographic concepts will first be introduced.

2.2 Crystallography basics

Crystals exist due to overall Coulomb attractive forces between atoms and a repulsive short range force (as a result of Pauli repulsion). Prior to the discovery of quasicrystals, a periodic structure was considered the state of minimum energy for crystalline matter. A crystal is described by a combination of a lattice of points in space and a basis of atoms/molecules positioned at these points. In 3D, a repeated parallelepiped used to describe the structural arrangement is termed the unit cell. This is formed from three basic lattice vectors (constants) $\vec{a_1}$, $\vec{a_2}$, $\vec{a_3}$ and the angles between these vectors α, β, γ as shown in Figure 2.

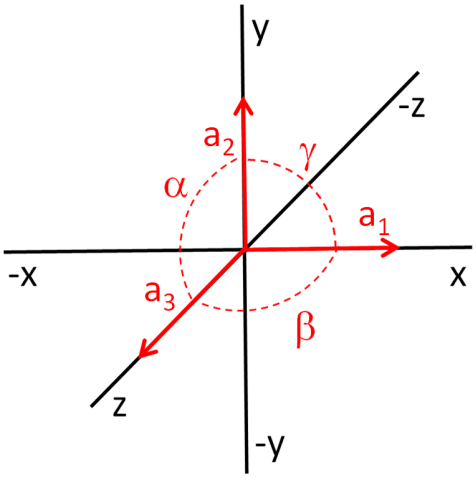

Figure 2: Crystallographic axes in 3-dimensional space. Lattice vectors $\vec{a_1}$, $\vec{a_2}$, $\vec{a_3}$ and angles α, β, γ are used to describe the unit cell of a crystal structure. Hence $\vec{a_1}$,$\vec{a_2}$,$\vec{a_3}$ do not necessarily have to be orthogonal.

$$\vec{R} = n_1\vec{a_1} + n_2\vec{a_2} + n_3\vec{a_3} \tag{1}$$

Using integer values for n_1, n_2, n_3 the translation vector ($\vec{R}$) in Eqn. 1 transforms the cell to an identical environment. All the possible periodic crystal systems are classified according to translational symmetry (totalling 7). When combined with different centering for the 3–D unit cell they are termed the 14 Bravais lattices. Adding a basis to the lattice and combining with the possible symmetry operations (rotation, inversion, reflection, screw plane, glide plane) gives the space group of the structure. The choice of a unit cell is not unique and the smallest unit cells containing one lattice point are called primitive unit cells. The Wigner-Seitz unit

cell is a common primitive unit cell formed by taking perpendicular bisectors from a lattice point to all the nearest-neighbour lattice points.

Only periodic crystals with rotational symmetry based on $\pi, 2\pi/3, \pi/2$, and $\pi/3$ are allowed. For example, visualise a 2–D plane or 3–D space to be filled exactly with one type of tile or polyhedron without overlapping. Examining Figure 3 one can see that squares, rectangles, triangles and hexagons fill the plane and cuboids and tetrahedrons completely fill space. Crystal lattices with these symmetries adhere to the crystallographic restriction theorem.

Regular pentagons and tiles of rotational symmetry greater than 6 cannot tile a plane without leaving gaps and the same is true for their 3–D counter–parts. It is difficult to envision how order is possible using more than one type of structural unit which includes a unit of forbidden symmetry. Such arrangements are discussed in Section 2.3.

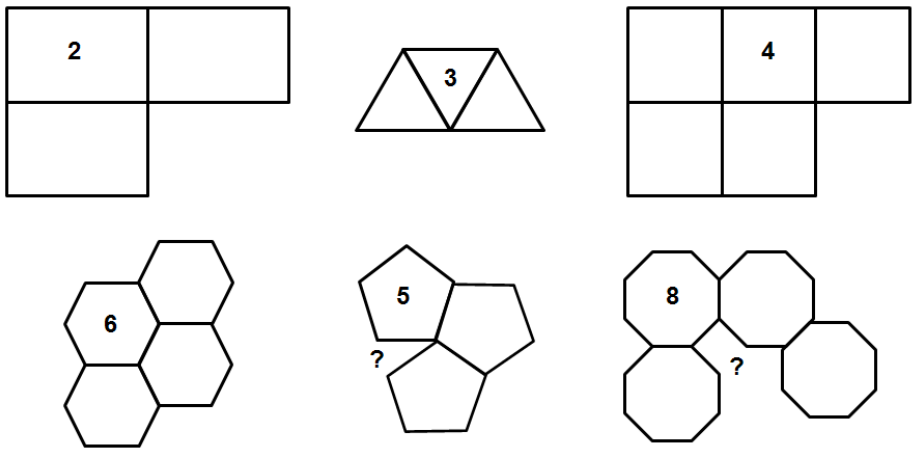

Figure 3: Demonstration that tessellation of a plane without leaving any gaps and overlaps between tiles is only possible with 2, 3, 4 and 6–fold rotational symmetry.

The crystallographic restriction theorem can be simply proved using geometric considerations. Consider a lattice point A in the Euclidean plane separated from a second lattice point B by a translation vector of the lattice $\vec{r}$. Now rotate about B by a rotation of the lattice structure $\pm\theta$ to another lattice point A$'$ and rotate around A by $\pm\theta$ to lattice point B$'$. The resulting vector between A$'$ and B$'$ (termed $\vec{r}\,'$) must also be a lattice translation vector. Since $\vec{r}\,'$ is parallel to $\vec{r}$ in a periodic

lattice its magnitude is an integer multiple of r:

$$r' = nr \tag{2}$$

The resulting trapezium (AA′B′B -see Figure 4) can be used with trigometric relationships to solve for $\vec{r}\,'$:

$$r' = 2r\sin(\theta - \frac{\pi}{2}) + r = -2r\cos\theta + r \tag{3}$$

By substituting Eqn.2 in Eqn. 3 and rearranging for $\cos\theta$ one obtains:

$$\cos\theta = \frac{1-n}{2} = \frac{N}{2} \tag{4}$$

where the integer $N = 1 - n$. Since $\cos\theta$ does not exceed 1, $|N| \leq 2$. Hence θ can only equal $\pi, 2\pi/3, \pi/2$, and $\pi/3$. The theorem can also be proved in 3 dimensions using this method and extended to higher dimensions using matrices.

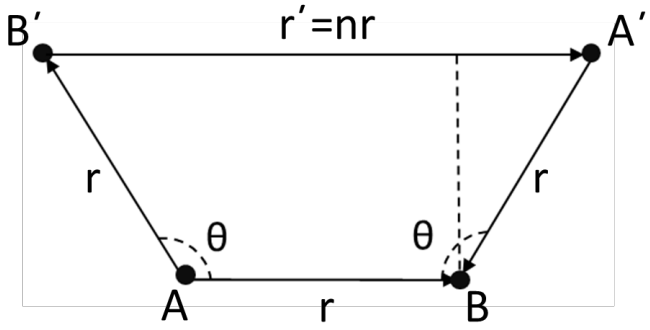

Figure 4: Representation of the generation of lattice points by rotating a lattice vector $\vec{r}$ by θ.

Parallel planes in a crystal structure with the same arrangement and density of points can be described within the unit cell using Miller indices. The Miller index of a set of planes comprises of the coordinates of a vector perpendicular to the lattice planes and are denoted in curly brackets i.e. {h, k, l}. It is the smallest integer of the same quotient. This is important notation used in structure determination using diffraction techniques and in surface studies of different exposed bulk planes. The above formulations and descriptions are for perfect crystals. Real crystals have defects such as stacking faults, vacancies and impurities due to formation in imper-

Term	1	2	3	4	5	6	7
Sequence	1	1	2	3	5	8	13
Ratio of terms		2	1.5	1.66	1.60	1.625	1.6153

Table 1: The Fibonacci sequence demonstrating that the ratio of a term to the previous term converges towards τ as the terms increase.

fect conditions. Surface reconstructions are inherent to the structure due to surface terminations of the bulk.

2.3 Aperiodic order and the golden mean

Ordered sequences can be generated that never repeat, such as the Thue–Morse sequence and the Fibonacci sequence. A term in the Fibonacci sequence is formed from the sum of the previous two terms. It is seen that the ratio of a term to the previous term in the sequence tends towards the irrational number τ, – called the golden mean,– as the number of the terms increases. Table 1 shows the first 8 terms of the sequence and the corresponding ratios and Eqn. 5 shows some expressions for τ.

$$\tau = \frac{(\sqrt{5}+1)}{2} \quad \tau = 2cos36^\circ \quad \tau = 1 + \cfrac{1}{1 + \cfrac{1}{1 + \cfrac{1}{1+...}}} \tag{5}$$

A type of aperiodic, 1–D chain of lattice points can be formed by inflation of a Fibonacci sequence of point spacing. Consider a long spacing (L) and a short spacing (S) between points, where the ratio of L to S is τ. These lengths are placed in a 1-D line such that they follow the substitution rules that S is replaced by L and L is replaced by LS, hence giving the next term in the sequence. Inflating the sequence in such a way forms a non-periodic sequence that is evidently ordered. As the sequence inflates the ratio of the amount of L spaces to S spaces tends towards τ and the total number of spacings follows the Fibonacci sequence. Placing so-called atomic surfaces at these spacings forms an ordered solid- a 1-D quasicrystal model. The golden mean is also synonymous with 5-fold rotational symmetry; Figure 5 shows that the internal lengths of a regular pentagon are related by τ.

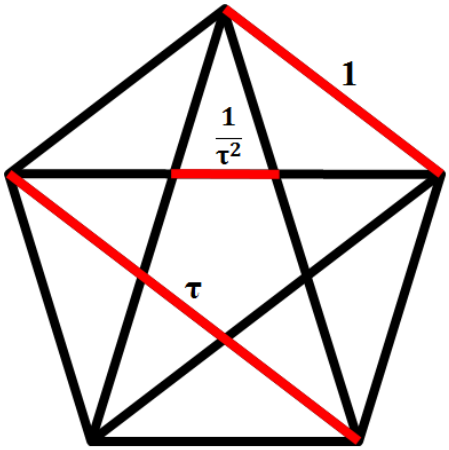

Figure 5: A regular pentagon where some distances between vertices related by τ have been marked.

2.4 Penrose tiling

The use of several proto–tiles to admit a tiling of an infinite plane that is non–periodic was explored by mathematicians in the 1960s [10]. Such tilings suggest that it may be possible to form a 2–D model of a quasicrystal that includes more than one type of structural unit or overlapping of these units.

By following matching rules for the placement of neighbouring proto–tiles, a tiling can be constructed so that it is aperiodic. Roger Penrose among others discovered examples of such tilings in the 1970s. Below in Figure 6 (right) is an example of the P1 Penrose tiling. In the left hand side of the figure the set of proto–tiles are displayed. The numbers along the edges signify the matching rules for adjacent tiles; a 1 must be placed alongside a $\bar{1}$ etc. With the appropriate dissections the Penrose P1 tiling can be inflated or deflated to the P2 and P3 tiling and vice versa. The Penrose tiling can be seen to completely cover a plane without gaps via the extension theorem, which projects the tiling so that it covers circles of increasing radii. The tiling is aperiodic infinitely as any tiling can be inflated into a unique composition of patches.

The Penrose tiling is found to have a Fourier transform (FT) with ten-fold rotational symmetry, as shown in Figure 7, like that of an icosahedral quasicrystal structure. The FT is ten-fold rather than five-fold due to the selected finite area having inversion symmetry. P1, P2 and P3 tilings have been overlaid on quasicrys-

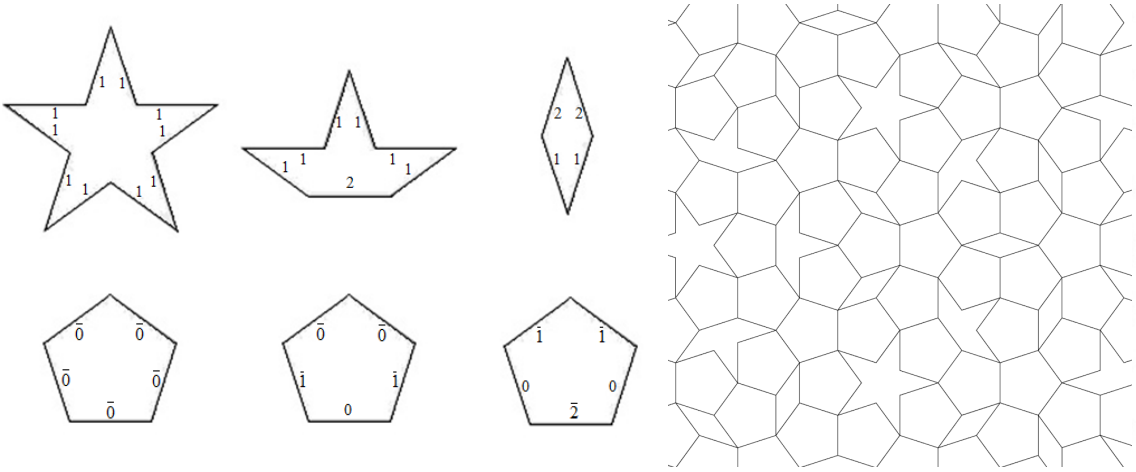

Figure 6: Left: A set of tiles used to construct the P1 aperiodic tiling. Right: A section of the Penrose P1 tiling

tal surfaces with the aim of classifying surface features and matching them with the long-range order [11, 12].

The Penrose tiling can be generalised to 3 dimensions. This consists of prolate and oblate rhombohedra where the volume of one is related to the other by a multiple of τ. This is the simplest description of a quasicrystal structure, termed the random tiling model.

2.5 Higher dimensional crystallography

Due to lack of periodicity, quasicrystal structures cannot be described by normal crystallography models. Therefore a quasicrystal cannot be described and analysed in reciprocal space using 3 Miller indices. A higher dimensional (nD) model is required to model the structure by describing the quasicrystal as a periodic N–D structure embedded in higher–dimensional (n–D) space, where N<n [13]. For polygonal quasicrystals 5 dimensions are required to describe the structure and for icosahedral quasicrystals 6 dimensions are required.

Figure 8 depicts a model for describing the generation of a 1-D aperiodic sequence from higher dimensional space using the cut and project method. The regular, 2–D square lattice has a line $E_{\|}$ placed with an irrational gradient with respect to the grid. In the example in Figure 8 the gradient is $1/\tau$. Lines are extended from the regular lattice points along the direction perpendicular to $E_{\|}$, labelled $E_{\perp}$. A real

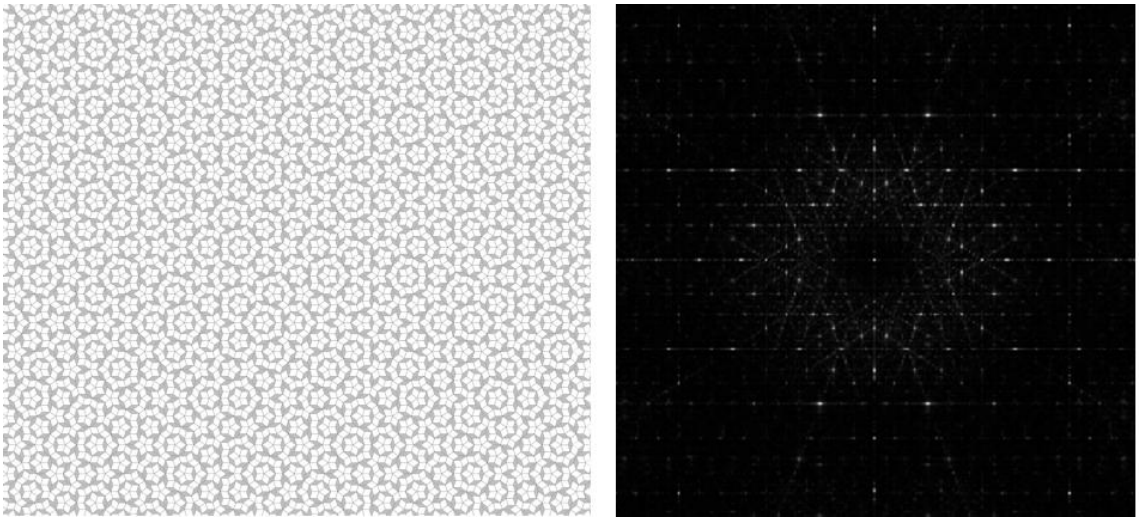

Figure 7: A section of the Penrose P3 tiling (left) and its Fourier transform (right) demonstrating the 10–fold symmetric order of the tiling

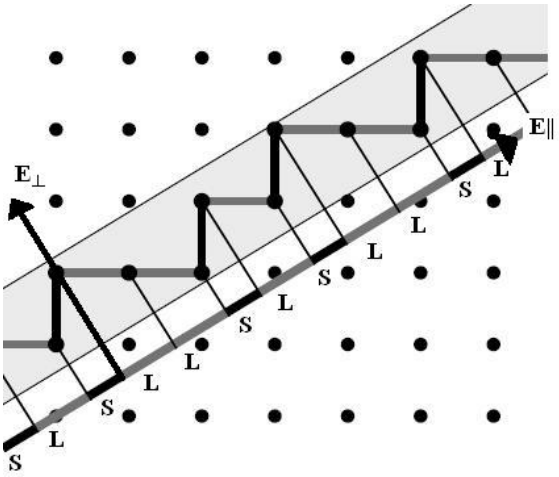

Figure 8: Diagram to demonstrate how a 2–D model can be used to generate a 1–D aperiodic chain.

space atomic surface is generated where the extensions of the lattice points intersect the $E_{\parallel}$ line. The positions of $E_{\parallel}$ crossing the projections generates a Fibonacci chain of long (L) and short (S) spacing (as described in 2.3) where the ratio of the length of L to S is τ. The lower dimensional cut of the periodic lattice still has long range order whether the cut is irrational or rational due to the higher dimensional long range order of the 2–D lattice.

For periodic structures the rank (n)(number of indices required) is equal to the number of dimensions the structure exists in. To describe a quasicrystal 5 or 6 integer reciprocal vectors are needed instead of 3 Miller indices. These are termed generalised Miller indices. The projection of the 6–D lattice into 3–D does not give the complete structure and atomic decoration of the points is required.

The higher dimensional (n–D) approach works well for perfectly ordered quasicrystals and is the only paradigm to allow application of direct analysis methods and the Patterson method to quasicrystal structures. The Fourier transform of the 5–/6–D unit cell is the structure factor of the quasicrystal, so this approach allows quantitative structure analysis. Unlike tiling models, it does not determine the arrangement of atoms and clusters for disordered spin-glass (random tiling model) quasicrystal samples [14].

2.6 Approximants

Approximants are formed by a linear phason strain applied to a quasicrystal or a complex alloy of similar composition. Intermetallic systems that form quasicrystals are also found to form binary or ternary element approximants. Approximants have similar local structure (i.e. clusters) and ordering as their respective quasicrystal counterparts but have a finite unit cell with their diffraction spots periodically arranged [15]. As a result, rational approximants can be analysed like classical crystals. The unit cell can be very large but provides a basis for modelling scattering data. Approximants are key to the analysis of quasicrystal data as the distances in the Fourier transforms of both quasicrystals and their approximants correspond to the basis vectors of the reciprocal lattice. The distances on the Fourier transform are due to the characteristic cluster distances of stable shells within the clusters.

Rotating the parallel cut ($E_{\|}$) through perpendicular space so that it lies with a rational gradient with respect to the periodic grid and performing a cut or projection, as described in Section 2.5, leads to an approximant. This concept is demonstrated in Figure 9 where the rational cut of 45° leads to a periodic lattice with lattice parameter size equal to the distance L.

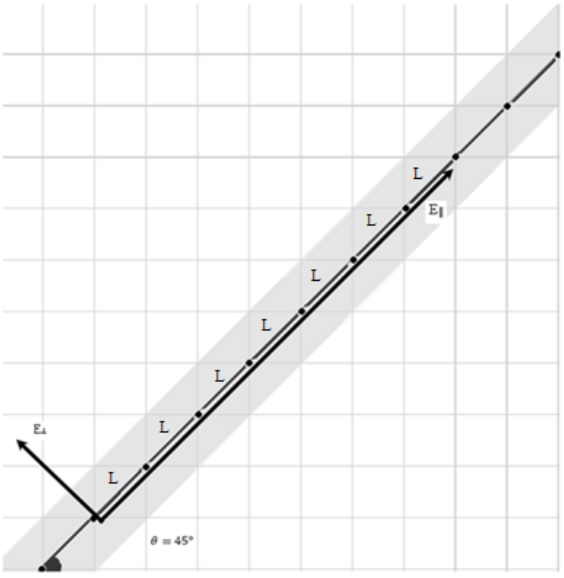

Figure 9: Model to demonstrate how an approximant can be generated from the same higher–dimensional space model as a quasicrystal.

2.7 Cluster models

Energetically stable atomic clusters are an interesting paradigm for investigating the formation of, and identifying local features in quasicrystals. A cluster in a quasicrystal is not necessarily the same as a stable, chemical entity and the concept needs careful further interpretation [16]. The customary view of a chemical cluster is an assembly of atoms more tightly bound than the surrounding atoms. Such a group should maximize packing fraction, be repeated throughout the structure and contain most of the volume (or surface area) of the material within itself. In this context the definition of clusters in quasicrystals may seem arbitrary and nothing more than a repeating structural motif but they are of increasing importance for relation to bulk physical properties of quasicrystals. Clusters are relevant as they exist in approximant phases also. For example, 87.5% of the atoms in an orthorhombic approximant to i–Al–Pd–Mn were assigned to overlapping pseudo–Mackay clusters [17]. The cleavage surface of Al-Pd-Mn was shown by STM topographic images to exhibit approximately nanometre size protrusions which may correspond to stable pseudo–Mackay clusters [18]. Clusters have also been observed in the modelling of quasicrystal formation [19, 20].

The cluster concept is that of aperiodic overlapping between the one or more

types of modified clusters combined with the contribution of some 'glue atoms' between them to form the overall structure. On the truncated surface, clusters can be viewed as polygons on the plane or –in the case of higher order structures– rings adorned with filling atoms.

The quasi–unit cell approach applies one cluster with several overlap rules to build an aperiodic structure (unlike tiling which needs at least 2 tiles). The clusters evidently must be able to share atoms without changing their atomic decoration greatly. This approach can be mapped to the 2-D Penrose tiling approach and such a relation leads to a hierarchical cluster model. In the hierarchical model an arrangement of clusters can deflate into a larger, more spherical cluster and continue to larger scales.

Al–TM (TM = transition metal) quasicrystals contain a majority of Mackay-type icosahedral clusters (see Figure 10 a)), Zn–based quasicrystals can be described with Bergman clusters (see Figure 10 b)) and many approximants involve the Tsai–type cluster [21].

2.8 Icosahedral quasicrystals

Icosahedral quasicrystals are the only structures that are quasiperiodic in all three spatial directions. Their structure consists of 6 intersecting 5–fold axes, 10 3–fold axes and 15 2–fold axes. The crystallographic description of their structure relies on projections from a periodic structure in 6–dimensional space (See Section 2.5). There are 3 types of icosahedral quasilattices that are described by P– (primitive), F– (face–centred), and I– (body-centred) hypercubic lattices in the higher dimensional space structural. Stable F– and P– type icosahedral structures have been grown experimentally. A P–type icosahedral structure can be viewed as two inter–penetrating F–type lattices where reflections of all indices can be observed in its diffraction pattern. In this thesis, two different icosahedral quasicrystals are employed for adsorption studies.

2.8.1 Icosahedral Aluminium–Palladium–Manganese (*i*–Al–Pd–Mn) quasicrystal

The aluminium–palladium–manganese quasicrystal (Al–Pd–Mn) was the first quasicrystal which was produced in large, single grain samples [22] and is the most

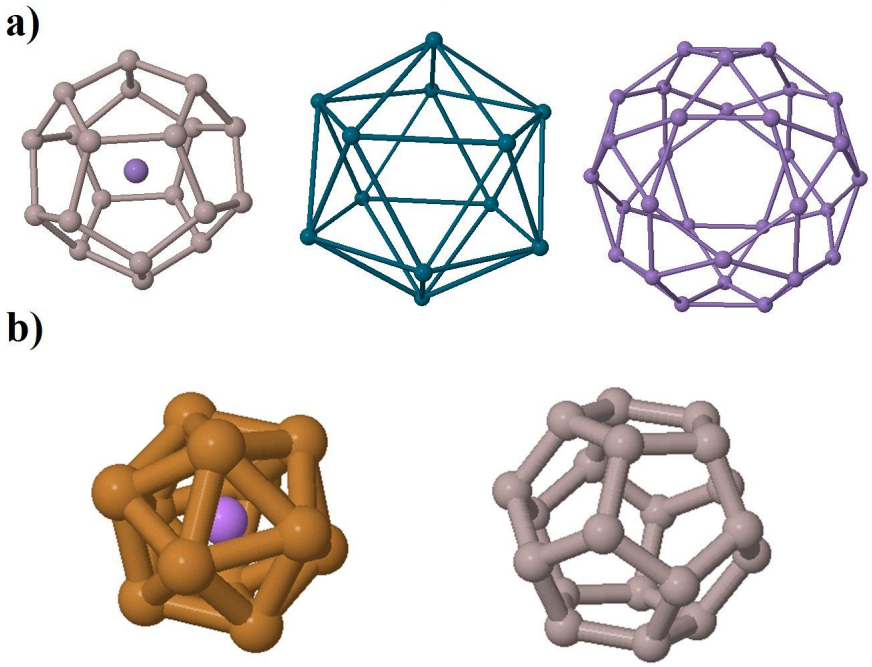

Figure 10: Model displaying the concentric shells of clusters relevant to the structure of quasicrystals. a) Mackay–type cluster in AlPdMn. Grey = Al, Green = Pd, Purple = Mn. Outer icosidodecahedron has a diameter of 1.556 nm. b) Bergman–type cluster in AlCuLi Grey = Al, Orange = Cu, Violet = Li. Outer Al dodecahedron has a diameter of 0.348 nm.

studied to date. *i*–Al–Pd–Mn has an F–type (face–centred) structure in higher–dimensional space. X-ray powder diffraction patterns of rapidly solidified samples showed that the chemical ordering has a strong dependence on composition [23]. The elongation of the icosahedral phase along the line with a constant valency ratio of e/a = 1.75 in the phase diagram (see Figure 11) suggests that electronic structure plays an important role in the stabilisation of this phase.

The real space structure of *i*–Al–Pd–Mn can be described by interpenetrating pseudo-Mackay and Bergman type clusters of atoms (see Section 2.7 for an introduction to cluster models). There is a conflict in building principles as the clusters overlap leading to reconstruction of the outer shells of the cluster. For example the number of atoms in the fourth shell of the pseudo–Mackay cluster can vary from 15 to 30.

The pseudo–Mackay cluster found in *i*–Al–Pd–Mn is composed of four concentric shells of atoms and has a radius close to 10 Å. The inner dodecahedron is composed of

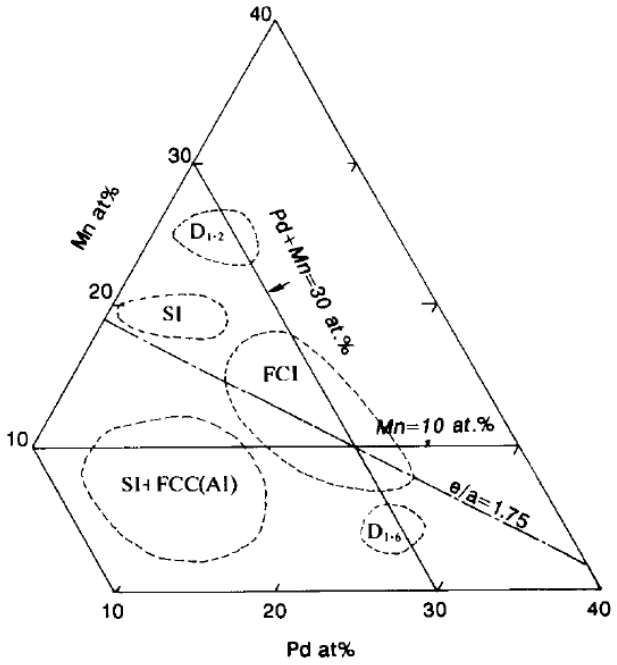

Figure 11: Part of the phase diagram for the rapidly solidified Al–Pd–Mn system. (SI, simple icosahedral; FCI, face–centred icosahedral; $D_{1.2}$ and $D_{1.6}$, decagonal phase with a periodicity of 1.2 nm and 1.6 nm, respectively). Reprinted from [23].

Al and is quite irregular, with only about 7–8 of the atoms present. This irregularity leads to the cluster being termed approximate or 'pseudo' as this core can be better represented as a base-centred cube. The intermediate icosahedron shells are made up of Mn and Al/Pd respectively. The outer icosidodecahedron shell is also an Al/Pd mixture.

The Bergman cluster contains 33 atoms in two shells with a radius of around 4 Å. The shells are centred on a Pd atom that is surrounded by an icosahedral shell of Al. This is followed by an outer layer in the shape of a dodecagon with around 12 Al atoms, 8 Pd and a proportion of Mn.

A full structural determination is difficult to obtain for Al–based quasicrystals due to the inherent chemical disorder and the lack of contrast of the different chemical constituents using x-ray diffraction (XRD). The bulk atomic structure of this phase has been examined with neutron diffraction in combination with XRD and further elucidated in a separate experiment with convergent beam electron diffraction (CBED) [24–26]. It was found that there were six different atomic hypersurfaces on the 6–D lattice. The 3–D structure is found to be composed of two chemically

different Mackay-type icosahedral shell structures. There is some disorder found in the Pd atomic hypersurfaces of the structure resulting in a fluctuation in atomic position of ∼1 Å. The CBED study refined the bulk structure and described the extended pseudo–Mackay and extended Bergman clusters located in the structure.

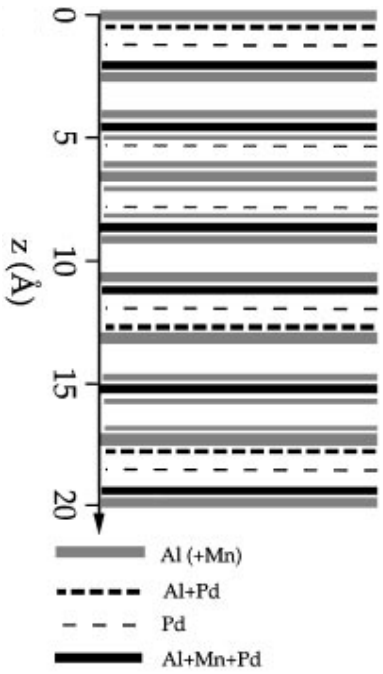

Figure 12: Layers drawn at their respective depths z, as bars with thickness proportional to the atomic density in each layer, together with their approximate composition; parentheses indicate minority species. Reprinted from [27].

The *i*-Al-Pd-Mn surface

The 2– and 3–fold surfaces of this quasicrystal are not stable as they exhibit faceting [28,29]. The substrate used in the experiments for adsorption studies is cut perpendicular to a five–fold axis. This orientation is along a natural cleavage plane. The surface structure has been determined experimentally with LEED(IV), He scattering, STM [30], medium energy ion scattering (MEIS) and photo–electron diffraction (PED) [31]. Following a preparation cycle of sputtering and prolonged annealing the surface can be considered a termination of the bulk with only slight lateral relaxation of 0.38 Å [11], MEISprep, prep. The surface therefore has the potential to act as a quasiperiodic 'template' for epitaxial growth. The surface was shown via

STM to have a step and terrace type morphology with two different step heights of 6.60 Å and 4.08 Å. The ratio of these step heights is close to the golden mean (τ) and the sequence of step heights in any direction parallel to the surface follows a Fibonacci sequence. Consequently, one can see that the quasicrystalline nature of the as–prepared surface is revealed even when no sub–terrace resolution is obtained.

Dynamical LEED showed that the bulk terminated surface planes are dense and Al rich with about 10% Mn [27]. Figure 12 indicates the relative composition and density of the experimentally determined surface layers of a *i*-Al-Pd-Mn sample used in the study. Several atomic models have been compared and show that the topmost layer contains no Pd [32]. Many Mn atoms in the topmost layer are seen to be surrounded by Al/Pd pentagons of a single orientation in the layer below. High resolution STM measurements and *ab–initio* surface models showed that the surface can be overlaid with a P1 tiling of 4.8 or 7.8 Å. The surface can be described by inter–penetrating truncated pseudo–Mackay and Bergman clusters. Pseudo–Mackay clusters are found at the centre of pentagon tiles and the smaller Bergman clusters at the vertices. Figure 13 a) shows an STM image of the clean surface with sub–cluster resolution. The two features that recur the most have been highlighted – the 'dark star' and the 'white flower'. Figure 13 b) shows the same area of the surface after FFT filtering the high symmetry features from the image to reveal a greater amount of atomic resolution. The 'white flower' corresponds to a truncated pseudo–Mackay cluster with a Mn atom in the surface layer at the centre. There is some disagreement in the literature over whether the five–fold hollows termed the 'dark star' features are part of a Mackay or Bergman polytope. Figure 13 c) shows a surface model for the 3/2 approximant of *i*–Al–Pd–Mn demonstrating how a P1 tiling can connect high symmetry, repeating features.

2.8.2 Icosahedral Silver–Indium–Ytterbium (*i*–Ag–In–Yb) Quasicrystal

The silver–indium–ytterbium (Ag–In–Yb) quasicrystal has a P–type (primitive lattice) lattice structure [34] in 6–D space. It is considered isostructural to *i*–Cd–Yb because of the similarity of the XRD spectra. *i*–$Cd_{5.7}$–Yb was the first binary quasicrystal discovered that was thermodynamically stable [35]. XRD from this intermetallic showed that there was significant scattering contrast between Cd and Yb and there was greater chemical order compared to preceding, more chemically

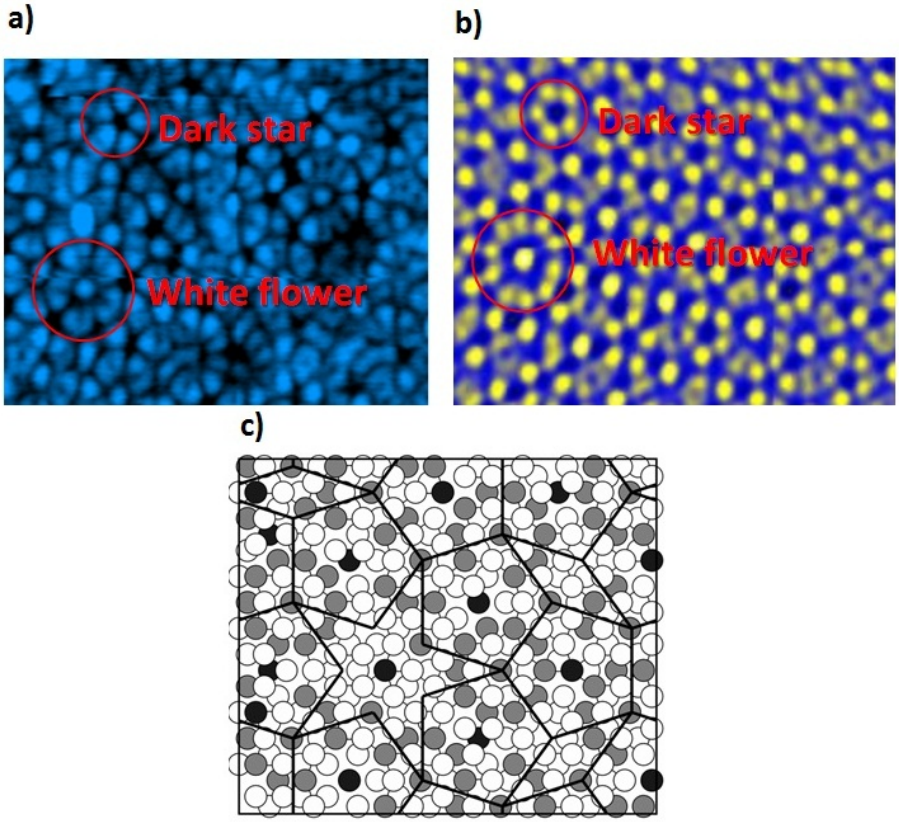

Figure 13: a) (11 nm × 9 nm) STM image of clean *i*–Al–Pd–Mn. Common, local high symmetry features are highlighted. Truncated pseudo–Mackay and Bergman clusters are imaged. b) (12 nm × 9 nm) The image in a) has been Fast Fourier Transform (FFT) filtered to enhance the atomic resolution. c) A model of the atomic structure of the fivefold surface of *i*–Al—Pd–Mn represented by the M slab cut from the 3/2 approximant. The surface is covered by a part of a P1 tiling (thick lines). The positions of atoms are displayed by circles: Al - open circles, Pd - shaded circles, and Mn - closed circles. Reprinted from [33].

complex quasicrystals. These facts led to the first full structural solution of a quasicrystal; it was found to be composed of a quasiperiodic packing of a rhombic triacontrahedral (RTH) cluster containing 66 atoms.

Cd has a high vapour pressure making it unsuitable for measurements in a vacuum. By considering Hume-Rothery rules [36] for the solubility of an element in a metal, stable icosahedral quasicrystals in the Ag–In–Ca, Ag–In–Yb, Ag–In–Ca–Mg and Ag–In–Yb–Mg systems were discovered [37]. These are considered Hume–Rothery phases that are stabilised by the elements having the same atomic size, valence electron concentration, and electronegativity (Pauling number). The qua-

sicrystal phase Ag_{42}–In_{42}–Yb_{16} was formed by replacing Cd with equal amounts of Ag and In. Averaging the valency (ratio of the number of valence electrons to the number of atoms) in Ag/In gave 2.0 therefore maintaining the same ratio as that in $Cd_{5.7}$–Yb. In addition, the atom diameter of Ag and In is close to that of Cd at 0.311 nm.

The Cd–Yb/Cd–Ca family of quasicrystals have substantially different electronic properties compared to Al–based ternary quasicrystals, for example a higher electrical conductivity and a positive temperature coefficient of resistance [38, 39].

The *i*–Ag–In-Yb surface

All three high–symmetry surfaces of *i*–Ag–In–Yb are stable with no significant faceting. Initial RHEED (reflection high-energy electron diffraction) and STM measurements of the five-fold surface found that after sputtering and extended annealing a flat surface with a step and terrace morphology was formed [41]. The surface displayed quasicrystalline order and comparisons to the bulk model showed the terminations to be Yb rich with intermediate density. The step heights, measured with STM, were τ related and followed a Fibonacci sequence along any direction further evidencing the quasicrystallinity of the surface.

High–resolution STM images of the five-fold surface structure revealed the cluster nature of the surface [40]. A change in bias of the tip–sample arrangement in constant current mode resulted in different features being imaged– see Figure 14. In Figure 14 a) and c) the sample is at negative bias relative to the tip so that it is imaging the occupied states at the surface. Here, round protrusions of 1.3 nm are imaged that tend to form a pentagonal arrangement with an edge length of 2.4 nm. Comparison to the model shows that these sites correspond to Ag/In clusters. The inability to gain sub–cluster resolution is attributed to the electronic coupling of Ag and In in the electronically stable clusters. Figure 14 e) shows the surface in a) after fast Fourier transform filtering, with part of a P1 tiling (with an edge length of 2.4 nm) overlaid to highlight pentagonal features. Sub–cluster features are only discernible after filtering of the quasicrystalline features is applied to the image. Figure 14 b) and d) shows the same surface area section at positive sample bias (i.e. imaging unoccupied electronic states). Smaller clusters are evident here which are revealed as ring–like features after FFT filtering of the high–symmetry features – see Figure 14 f). The rings are 1.8 nm in diameter and correspond to

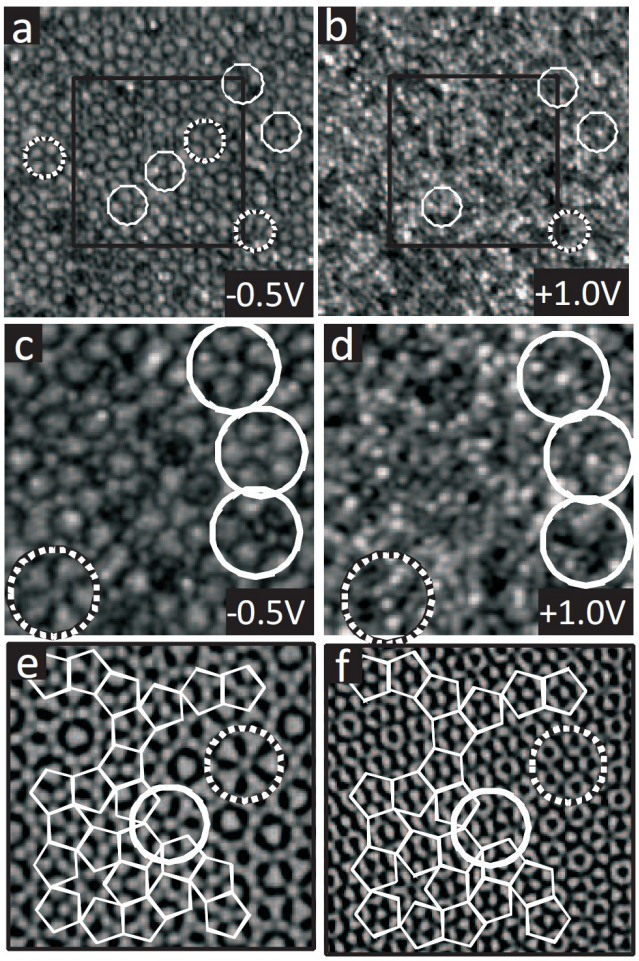

Figure 14: High resolution STM images of the fivefold i–Ag_{42}–In_{42}–Yb_{16} surface. (a, c) Images taken at negative bias. (b,d) Images taken at positive bias (a, b: 49 nm $\times$ 49 nm; c, d: 23 nm $\times$ 23 nm; I_T = 1.3 nA, tunnelling temperature: 78 K). The full and dotted circles mark pentagonal features of two different orientations. (e–f) Area marked by a frame in (a) and (b) after Fourier transform pass filtering and with a pentagonal tiling overlaid. Reprinted from [40].

rings of Yb in the surface model. This conclusion is further supported by theoretical calculations showing that the Yb–5d level dominates the occupied states near the Fermi level [42].

3 Adsorption and growth on quasicrystal surfaces

Surface science involves the study of surface properties and interface interactions, such as gas-solid interactions and epitaxial phenomena. The development of nanotechnology requires surface analysis, as the particles get smaller and therefore the proportion of atoms exposed to surface effects increases. The region of a solid near the surface either reconstructs so as to increase bonding coordination, or the surface may be considered a termination of the bulk crystal. Either scenario results in different properties to that of the bulk [43]. Surface electronic properties and many other surface phenomena require explanation at the atomic scale. The discovery of quasicrystals led to new challenges in the interpretation of results due to their complexity, especially in terms of more quantitative structural measurements.

Quasicrystal surfaces have unusual tribological properties; such as low friction and high wear resistance, but – like most intermetallics– are brittle in bulk form [44]. Therefore, they have been proposed to have potential applications in surface coatings and to aid in the reduction of friction heating effects – see Section 2.1. Such properties are thought to be due to the quasicrystalline ordering and not due to the complex composition of the material [45]. The study of quasicrystal surfaces was initiated in 1990 with a scanning tunnelling microscope (STM) investigation of the tenfold surface of *d*–Al–Co–Cu [46]. In 1997, when research commenced into quasicrystal surfaces at the University of Liverpool, there were many unanswered questions posed about the termination of the bulk quasicrystal and its relation to the surface properties [47].

3.1 Growth of thin films at surfaces

Thin films formed at surfaces are of interest due to their potential applications. For example, thin films are used to produce coatings with modified tribological properties, to improve the fabrication of microelectronic components, to modify optical properties and to enhance catalytic reactions. The surface is where crystal growth proceeds; therefore by studying surface processes new insights into crystal formation can be obtained.

Kinetic surface diffusion processes (e.g. nucleation, edge diffusion, dissociation) and the thermodynamics of crystal growth can be described with the TSK (terrace–step–kink) model. This model considers the surface in equilibrium when the po-

tential energy at the surface is minimised; i.e. when the adatoms are positioned at energetically favourable sites. The energy of an atom's position is determined by the number of formed and broken bonds to neighbouring atoms. An adatom may propagate across the surface potential via jumps and hops or by an exchange mechanism with surface atoms. Certain sites – such as defect sites, – have a lower coordination (fewer nearest–neighbour atoms than in the bulk) providing preferred growth fronts and nucleation points for adsorbing atoms.

To form epitaxial thin films the adsorbing particles need to have a certain degree of wetting ability on the underlying template. This depends on the relative surface tensions (γ) in the system. The degree of wetting is measured by contact angle measurements of a liquid droplet (L) –or nucleus of adsorbing gas, at a solid surface (S) in the surrounding adsorbing gas phase (G) using Young's law (displayed below in Eqn. 6).

$$cos\theta = \frac{\gamma_{SG} - \gamma_{SL}}{\gamma_{LG}} \tag{6}$$

Consider an ideal surface (no defects), where a liquid droplet can be roughly treated as a truncated sphere. The angle between the surface and the tangent along the droplet at the surface (θ)) can be used to predict the growth mode. If $\gamma_{SG} - \gamma_{SL} > \gamma_{LG}$, the liquid wets the solid and layer–by–layer (termed Frank–van–der–Merwe) growth will proceed. Frank-van–der–Merwe is the preferred growth mode, leading to uniform growth that is more likely to produce longer range order of epitaxial layers. Conversely, if $\gamma_{SG} - \gamma_{SL} < \gamma_{LG}$, 3–D island (Volmer–Weber) growth occurs. In reality it is difficult to determine the interface energy between the film and the substrate (γ_{SL}). A build-up of interfacial strain can accumulate in the film leading to lateral relaxation and the formation of 3–D nano-islands after one or more wetting layers. This intermediate growth mode is called Stranski–Krastanov growth or an Asaro–Tiller–Grinfeld (ATG) instability. These 3 main growth modes are illustrated in Figure 15.

Particles may be physically and/or chemically adsorbed at the surface, termed physisorption and chemisorption respectively. Certain adsorbing elements may have a chemical affinity towards a particular species in the substrate leading to a charge transfer between the adsorbate and substrate. The typical bond energy for such a reaction is around 0.4 – 2.2 eV. There may be an activation barrier for a particle to chemisorb at a surface leading to a delayed final, equilibrium state of the overlayer.

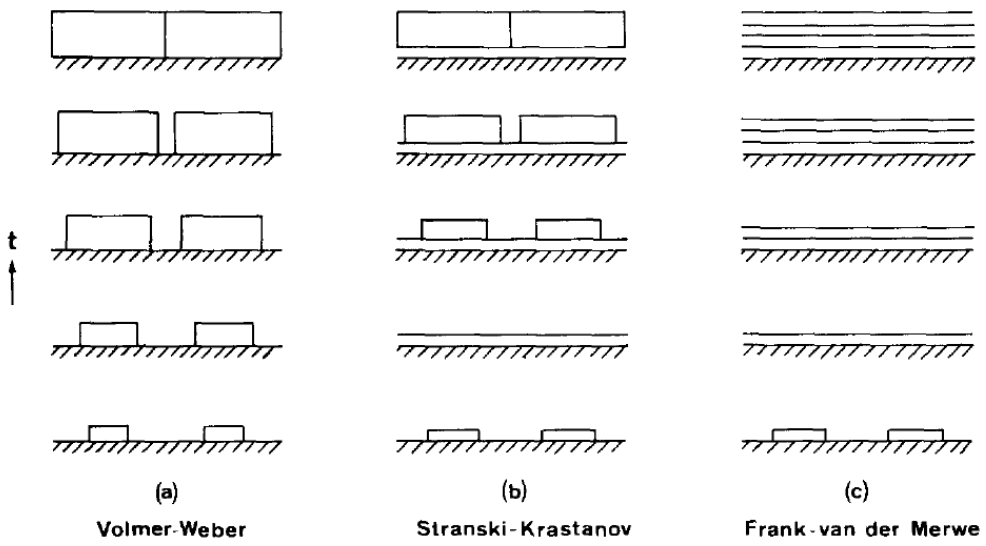

Figure 15: Three most basic modes of thin film accumulation by vapour deposition. Schematic representations of: (a) 3D crystallite growth; (b) monolayer followed by crystallites; (c) monolayer–by–monolayer growth [49]

Physisorption occurs when there are weak, van der Waals type interactions between the adsorbing particle and the substrate. The bond energy for a physical bond is $<$ 0.4 eV.

Many other factors effect the growth of thin films including substrate temperature, deposition rate, intermixing with the substrate and the density of surface defects. The effect of the deposition medium (UHV, gas or solution) will change the competition for adsorption between different incident particles and hence the growth process. A unique, preferred adsorption site for adsorbed particles and minimal lattice mismatch is required for the substrate surface order to translate to the overlying layer [48]. This can be difficult of obtain at the structurally and chemically complex surfaces of quasicrystals. Thin films will tend to be incommensurate because of competition between the periodic atomic order of the adsorbate and aperiodic atomic distances on the adsorbent. Also, there may be a range of sites with similar adsorption energies due to the complicated chemical arrangement.

As well as via epitaxial growth, a number of other methods have been used to attempt to form quasicrystalline thin films. Crystalline, epitaxially orientated islands have been found experimentally after sputtering of quasicrystal surfaces [50]. Thin layers of Al, Pd and Re deposited on a sapphire substrate followed by heating

to 680° were found to produce an icosahedral x–ray diffraction pattern [51].

3.2 Adsorption studies on quasicrystal surfaces

The experiments in this thesis involve epitaxial growth at surfaces of quasicrystals; elemental and molecular vapours are deposited upon the surface under study in an ultra–high vacuum environment (see Section 4 for details of evaporators used to achieve this). Such fundamental studies enable a unique study of adsorbate–substrate interactions due to the range of overlayer structures formed. Also, the formation of single component, artificial quasiperiodic layers will enable the experimental study of quasiperiodic order and the relating properties in solid state matter without the chemical complexity inherent to quasicrystals. For an overview of growth at quasicrystal surfaces see the reviews [52, 53].

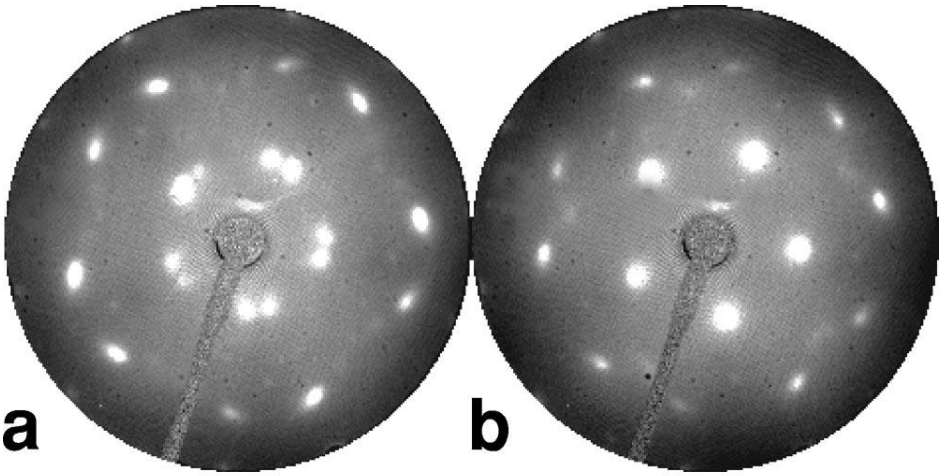

Figure 16: LEED patterns obtained from the fivefold–symmetric surface of $Al_{70}Pd_{20}Mn_{10}$ *i*-QC at primary-electron energies of a) 63 eV and b) 66 eV, after evaporating a 20 Å thick layer of Al. The fivefold symmetry of the patterns is consistent with a growth mode of Al in domains with five different orientations. Reprinted from [54]

Epitaxially orientated overlayers

Most single element overlayers yield periodic films with some orientational epitaxy with respect to the substrate. Such systems observed experimentally include

Al adsorbed on *i*–Al–Pd–Mn [54], Au/*d*–Al–Ni–Co [55], Ag/*i*–Al–Pd–Mn [56] and In surfactant mediated growth of Pt on *d*-Al-Ni-Co [57]. As an example, the low energy electron diffraction (LEED) patterns obtained from an Al multilayer deposited on *i*-Al–Pd–Mn are shown in Figure 16. Here, a 5–fold symmetry is clearly evident. The symmetric pattern around each of the 5 main spots confirms the crystalline fcc–(111) nature of the film. The large change in the position of the spots with a small beam energy change of 3 eV shows the (111) surface of the nano-crystals are at an angle relative to the surface normal.

An interesting case is that of layers of Au adsorbed on *i*–Al–Pd–Mn which usually produces a polycrystalline film. Pre–depositing a sub–monolayer coverage of In was evidenced with x–ray photo–electron diffraction (XPD) to promote the aggregation of epitaxially orientated, nanoscale twinned–crystals of $AuAl_2$ after annealing to 350 - 400 K [58]. In has a lower surface energy relative to Au and the quasicrystalline surface and therefore acts as a surface active agent (termed a surfactant) to promote epitaxial, layered growth. The investigation also looked at In mediated growth of Pt, Au and Ag on *d*–Al–Ni–Co and *i*-Al-Pd-Mn without success [59]. A medium energy ion scattering (MEIS) study concluded that the In surfactant mediated growth of Au on Al–Pd–Mn formed a disordered film contradicting these previous experiment results [60].

Similar growth modes were also observed in the deposition of magnetic elements on quasicrystal surfaces. Bulk quasicrystals display weak para-magnetic or diamagnetic properties, which can be due to the low relative amount of the magnetic element in their composition [61–63]. Quasicrystalline overlayers could be composed of a greater proportion of magnetic material. Such quasi-periodically ordered magnetic structures are predicted to have anti–ferromagnetic order [64, 65]. No pseudomorphic, magnetic overlayers have been grown experimentally so far. Systems studied by experiment include: Fe/Al–Pd–Mn [66], Fe/Al–Ni–Co [67, 68], Co/Al–Pd–Mn [69], Co/Al–Ni–Co [70], Ni/Al–Pd–Mn [71] and Mn/Al–Pd–Mn [72]. Techniques such as surface magneto–optic Kerr effect (SMOKE), Scanning Electron Microscopy with Polarisation Analysis (SEMPA) and X–ray magnetic circular dichroism (XMCD) were used in several of these studies to measure the magnetism of these epilayers.

An epitaxially orientated, multilayer of Cu formed on the *i*–Al–Pd–Mn surface was shown by STM and LEED, to exhibit an aperiodic row structure. The Cu growth proceeds with almost layer-by-layer growth on the 5–fold surface of Al–Pd–Mn; the next layer starts to form when the underlying layer is around 60% completed. The

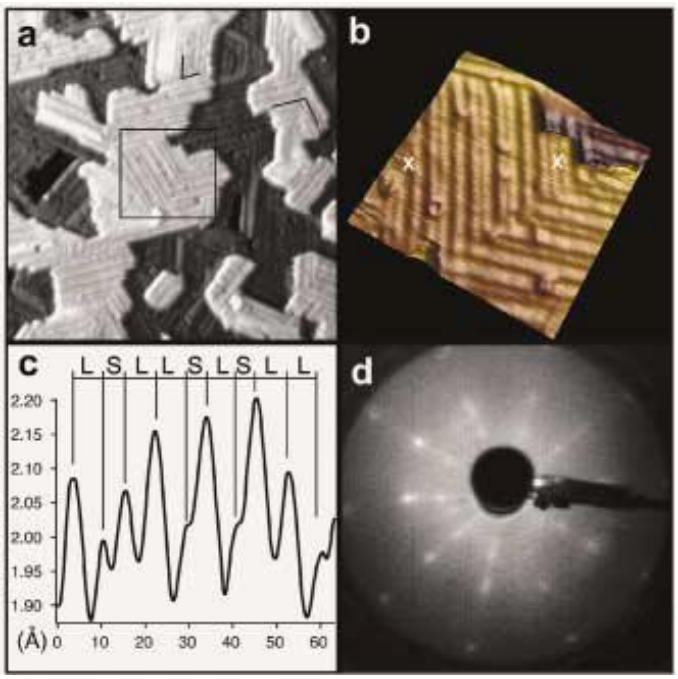

Figure 17: (a) 400 × 400 Å STM image of the fivefold surface of Al–Pd–Mn after deposition of 5.5 ML of Cu. (b) 100 × 100 Å detail from (a). (c) A profile between the points marked with a cross in (b); it demonstrates that the sequence of Cu rows is quasiperiodic with spacings given by LSLLSLSLL, where S = 4.5 ± 0.2 Å and L = 7.3 ± 0.3 Å. The ratio of these numbers equals the golden mean (τ within experimental error. (d) LEED pattern (beam energy 50 eV) corresponding to this phase. The relationships between spot positions are indicative of τ scaling.

ordered, one–dimensionally pseudomorphic Cu multilayer is formed at coverages above ∼4 ML. The aperiodic rows of Cu were first observed experimentally with scanning tunnelling microscopy (STM) and LEED [73]. An aperiodic sequence of two different sized rows was measured, termed short (S = 4.5 ± 0.2 Å) and long (L = 7.3 ± 0.3 Å) as displayed in Figure 17 a)–c). MEIS was initially used to propose several structural solutions for the overlayers [74] but failed to explain why it took several layers for the row structure to appear. A separate study finally solved the structure using dynamical LEED. The structure was found to be a vicinal surface of a body–centred tetragonal bct–(100) Cu structure [75] as shown in Figure 18.

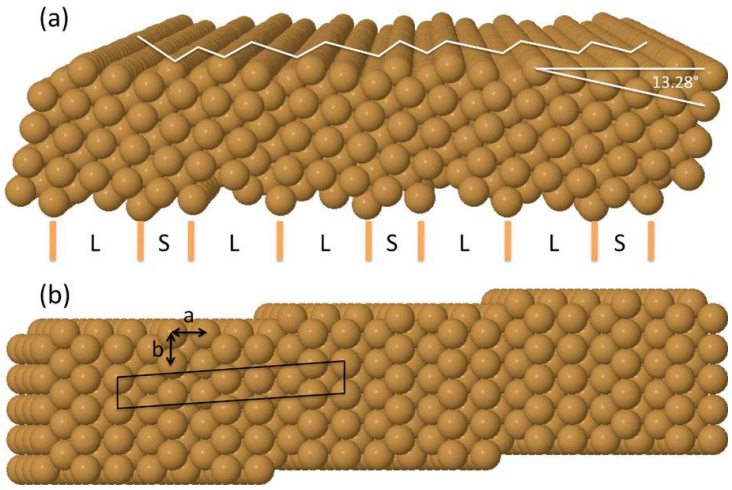

Figure 18: (a) Perspective side view of the vicinal body–centred orthorhombic LSL model, showing the L and S distances across the bottom and a schematic of the step structure at the top. (b) Top view of the stepped same model, showing the surface unit cell and the parameters a and b. Reprint from [75].

Pseudomorphic quasicrystalline systems

The first single element, quasicrystal overlayers produced were bismuth (Bi) and antimony (Sb) on the 5-fold surface of *i*–Al–Pd–Mn [76]. Many other elements have also been found to exhibit the growth of a complete 2–D pseudomorphic monolayer on a quasicrystal surface including: Pb/*i*–Al–Pd–Mn [77–79], Pb/*d*–Al–Ni–Co [80], Sn/*i*–Al–Cu–Fe [81], Alkali metals (K and Na) on *i*–Al–Pd–Mn [82], Pb and Sb on *i*–Ag–In–Yb [83] [84]. There was also limited success in the submonolayer with aperiodic ordering of atoms observed locally in the Si/*i*–Al–Pd–Mn [85] and Al/*i*–Al–Cu–Fe [86] systems. This ordering does not propagate to higher coverages.

In the case of a self-assembled monolayer of Pb on *i*–Al–Pd–Mn, the semi-metal initially forms a network of pentagonal clusters at submonolayer coverage. STM evidenced that larger Pb pentagons with an edge length of 4.2 ± 0.3 Å are formed from 5 smaller pentagons which are τ times smaller at 3.0 Å. Depositing Pb with the substrate maintained at a temperature 653 K improves the structural quality of the monolayer, as show in Figure 19. The inset 5–fold LEED pattern and overlaid P1 tiling support long-range order and the lack of defects in the layer. Density functional theory simulations were used to find initial adsorption sites of the pentagonal Pb clusters [79] and the simulated STM images were compared to experimental ones. The unique adsorption site for Pb atoms is in a surface decagon (D) tile (for a super-

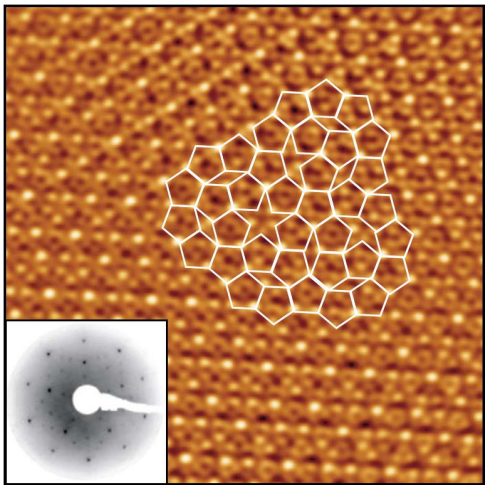

Figure 19: 250 × 250 Å STM image of 1.0 ML of Pb adsorbed on the fivefold surface of Al-Pd-Mn. Inset: LEED pattern recorded at 80 eV at the same coverage. Reprinted from [77].

imposed RHBS tiling) above a terminated pseudo-Mackay cluster. It forms a cluster of 10 Pb atoms consisting of 2 pentagons in the same orientation, as displayed in Figure 20.

Molecular adsorption at quasicrystal surfaces

Molecular adsorption at quasicrystal surfaces has been less successful than deposition with metallic and semi–metallic elements; to date no quasiperiodic molecular overlayers have been observed experimentally [87]. Computer simulations were used to model hydrocarbon adsorption on *d*–Al–Ni–Co [88]. The aim was to use the quasicrystal surface to enhance the effects of larger hydrocarbon lubricants, by finding incommensurately ordered smaller hydrocarbons. From the hydrocarbon adsorptions modelled, methane was found to form a pentagonal structure. The surface reactivity of potential candidate molecules was investigated by experiment with Fourier transform infra-red spectroscopy [87]. Carbon monoxide (CO), nitric oxide (NO), deuterated methanol (CD_4O), formic acid (HCOOH) and benzene (C_6H_6) were dosed onto the quasicrystal surfaces at various coverages. Benzene on *i*–Al–Pd–Mn and CO on *i*–Al–Ni–Co were concluded to be likely candidates.

Other experimental studies using various surface science techniques found that many molecules react aggressively with the surface and dissociate, for example,

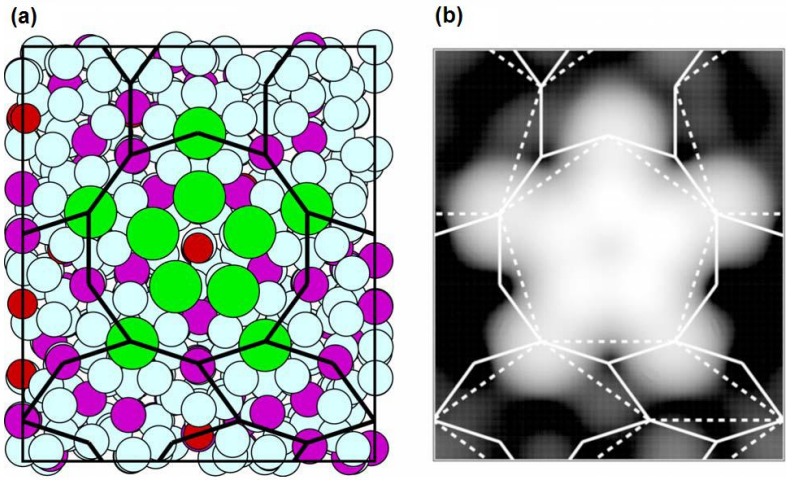

Figure 20: The large pale (green) circles show the positions of Pb adatoms in the D10T cluster in the BC sites and on top of the Al atoms surrounding the centre of the D tile. The cluster has the correct orientation, it is stable, and has the lowest energy among all tested configurations. Other circles represent atoms of the surface, cf. Fig. 4. (b) The calculated STM image of the D10T cluster has the correct size and orientation. The P1 tiling is shown by the dashed lines. Reprinted from [79].

oxygen, water and H_2S [89]. Other systems were shown to have disordered overlayers: benzene on *i*–Al–Pd–Mn [90], C_{60}/*d*–Al–Ni–Co [91], C_{60}/*i*–Ag–In–Yb [92]. Some τ-scaling of distances between adsorption sites was imaged with STM for C_{60}/*i*–Al–Pd–Mn but a disordered layer formed at higher coverage [93].

As well as using different shape and sized molecules to tune reactivity to the surface, the surface reactivity can also be modified by depositing a single element, quasi-periodic overlayer. This method achieved some success in the case of C_{60}/Pb/*d*-Al–Ni–Co [80], where hexagonal structure islands with some epitaxial orientational order grew. A disordered layer was observed for C_{60}/Cu/*i*-Al-Pd-Mn [94].

3.3 Pentacene

The pentacene molecule ($C_{22}H_{14}$) is a member of the family of organic compounds composed of linearly fused benzene rings named acenes. These aromatic hydrocarbons (or arenes) are conjugated (there are 3 or more overlapping p-orbitals in the electronic structure), have a planar arrangement of *p*–orbitals and follow Hückels rule for the lowering of energy in the rings. The delocalisation of electrons in such a structure infers increased chemical stability. A simple, atomic model for the pen-

tacene molecule with dimensions 14.21 Å × 5.04 Å is shown in Figure 21 a), where the C–C bond distance is on average 1.4 Å. For acenes there is a direct correlation between aromaticity and reactivity [95,96]. Calculations of the degree of aromaticity for each of the rings showed the central ring to be the most aromatic; NICS (nucleus–independent chemical shifts) for the 1st ring (outer rings) is -5.6 ppm, -10.8 ppm for the 2nd ring and -12.4 ppm for the centre ring.

The bulk crystalline form of pentacene is a herring–bone, triclinic structure. The unit cell of this structure is displayed in Figure 21 b) with lattice vectors a= 7.93 Å, b = 6.14 Å c = 16.03 Å, α= 101.9°, β= 112.6°, γ= 5.8°. There is also a slightly less energetically favoured thin film phase with an orthorhombic unit cell.

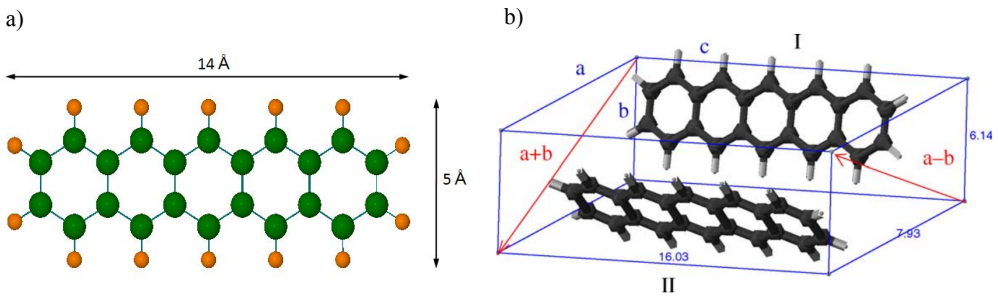

Figure 21: a) Atomic model of a pentacene molecule. Carbon: green Hydrogen: orange b) Herringbone packing of two inequivalent pentacene molecules in the triclinic unit cell of Campbell's model. The molecules are relaxed although three atoms in each molecule are kept fixed. The Bravais lattice vectors a, b, and c are assigned, as well as the vectors a + b and a - b. Reprinted from [97]

Pentacene is a p–type semiconductor with an energy gap between the highest occupied molecular orbital and the lowest unoccupied molecular orbital (HOMO-LUMO gap) of 1.1 eV. Semiconductors are the basic components of the majority of consumer electronics with an industry worth in the range of 250 billion USD. On account of its electron transport properties there has been intense research into incorporating pentacene as the active layer in organic semiconducting devices. Organic semi–conductors are of interest due to several desirable advantages they have over their inorganic counterparts. This includes low weight, mechanical flexibility [98], inexpensive materials and a much lower processing temperature for thin films. The right hand image of Figure 22 shows a flexible, polyethylene naphthalate (PEN) substrate with integrated circuits involving pentacene–based devices printed on top.

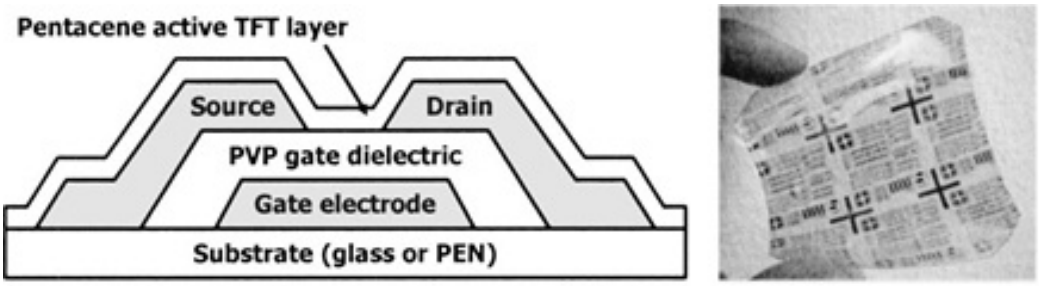

Figure 22: Schematic cross section a pentacene TFT, and photograph of a flexible polyethylene naphthalate (PEN) substrate with pentacene TFTs and integrated circuits. Reprinted from [103].

Pentacene–based electronic devices include photo–voltaic cells, light emitting diodes, thin-film transistors (TFTs). The left hand side of Figure 22 shows a cross section of a completely organic TFT with a pentacene layer and polyvinylphenol (PVP) gate dielectric. The largest field effect mobility of such devices has been reported as 1.6 cm^2/Vs which is comparable to amorphous Si devices [99]. The device parameters are poor compared to that of single crystal, inorganic devices, with high threshold voltages and low switching speed. There is a problem for such devices due to the degradation of thin films in ambient conditions and under drain–bias stress [100]. For example, pentacene easily oxidises under exposure to ultra–violet and visible light due to the generation of excitons. This problem has been addressed quite recently by encapsulation of the thin films [101].

Single crystal layers and reduced strain at interfaces in layered semiconductor devices improve charge transport. This led to research aimed at improving the long-range order and epitaxial growth of thin layers of pentacene [102].

3.3.1 Pentacene thin film studies

For this thesis project, the initial adsorption and formation of a pentacene layer was experimentally studied. The pentacene molecule has a tendency to form flat, complete layers on metallic substrates [102]. This is due to the anisotropic shape of this planar oligomer and weak, inter–molecular van der Waals interactions. There is an extensive literature of surface studies analysing the initial adsorption and structure of pentacene thin films on single crystal surfaces demonstrating that the first layer of molecules have their long molecular axis parallel to the substrate.

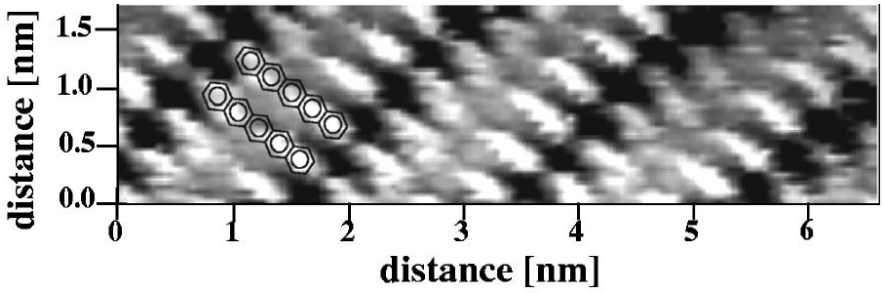

Figure 23: High resolution STM image showing rows of pentacene on the Au(111) surface corresponding to one type of unit cell found. The molecules are aligned with adjacent rows. Reprinted from [104].

Substrates on which pentacene layers have been studied –with experiment and/or theoretical calculations,– include: various Au surface orientations [104–106], Ag(111) [107], Al(100) [108], Fe(100) [109], various Cu surfaces [110,111], Si(111)–(7×7) [112] and graphite [113]. Theoretical studies found weaker physisorption at surfaces like Al(110) and Ag(111). In many cases the initial lying down orientation wetting layer is followed by 'standing–up' islands, stripes or layers. Theoretical calculations on Ag(111) showed that there is a weak binding of the first pentacene layer, with the structure aligning along the silver rows [107]. The molecule is adsorbed 'lying down' in the slightly less preferred, bulk–like thin film phase which continued to grow beyond a monolayer coverage.

For many systems the substrate induced varying degrees of epitaxial ordering in the first pentacene overlayer. For example, STM measurements evidenced the initial adsorption of pentacene along high symmetry surface directions on Cu(111) [111, 114]. On the Cu(110) surface structure the molecules adsorbed side–by–side into wires with a long range order of several hundred nanometres [110]. Similar rows of pentacene were observed on Au(111) where there were 4 different surface unit cells, all of which were commensurate with the underlying lattice [104] - see Figure 23. The ultra–violet photoelectron spectroscopy (UPS) technique showed a shift in the high binding energy edge upon adsorption of pentacene indicating a strong interaction (i.e. a chemical bond) between the molecule and surface.

On polycrystalline surfaces pentacene tends to adsorb end–on, forming upright layers, with the c–axis perpendicular to the surface e.g. SiO_2 [115].

The epitaxial growth of stable, small molecules such as acenes has not been attempted at complex surfaces such as those of quasicrystals, and as such provide

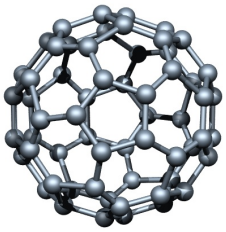

Figure 24: Representation of the atomic structure and bonding of the C_{60} molecule.

new insights on the interplay between the influence of different chemical species and the effect of structurally complex substrates on a molecular monolayer. Pentacene might be accommodated at certain adsorption sites on a quasicrystal surface as it is comparable to the size of surface cluster features.

3.4 carbon–60

Buckminsterfullerene is a fullerene molecule consisting of a closed cage-like structure of 60 C atoms, hence it is also named carbon–60 (C_{60}). The carbon atoms are bonded in a spherical, truncated icosahedron shape of regular pentagons and hexagons with each atom having 3 bonds as shown in Figure 24. C_{60} is the smallest fullerene with a van der Waals diameter of 1.01 nm. This allotrope of carbon is highly stable but it is not super–aromatic. Double bonds are not preferred between the pentagon faces for lowering energy and the molecule does not satisfy Hückels rule. Angle strain over the molecule due to bent pi–bonds can cause the molecule to chemically react. The molecules tend to pack together in an FCC structure with slight gaps between them resulting in a light material almost as soft as graphite.

C_{60} has many practical applications, such as in superconducting films and as optical limiters. It is also an n–type semiconductor, as it can readily accept up to 6 electrons [116]. Thin film transistors have been made incorporating C_{60} that have an switching ratio $> 10^8$ and a charge mobility of 0.5 cm^2/Vs [117].

3.4.1 C_{60} thin film studies

C_{60} has a large electron affinity (2.65 eV) and there is a strong inter–molecular interaction compared to other organic molecules. In most cases, C_{60} forms a covalent

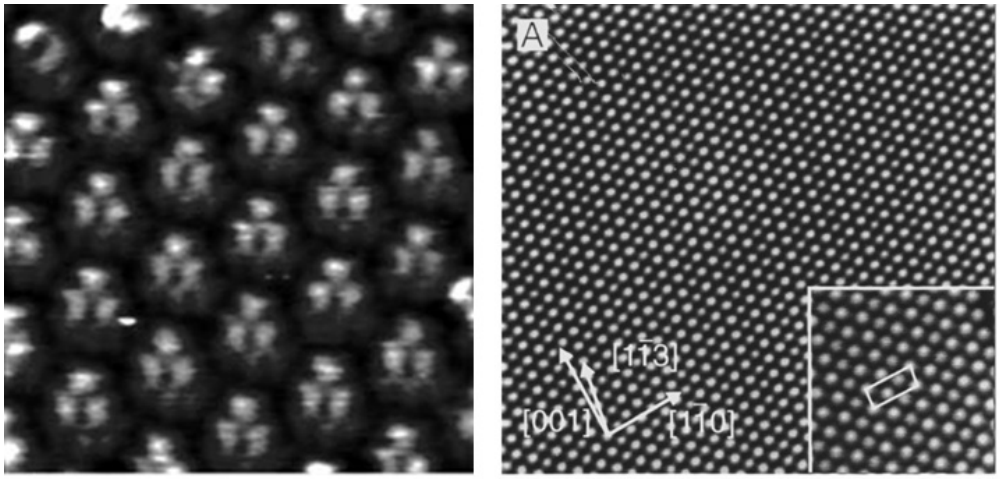

Figure 25: Left: STM image of C_{60} adsorbed on the Ge(111)–(13 × 13)R14 reconstructed surface. The sub–molecular resolution shows that all molecules are orientated the same with the same LUMO structure being imaged. Reprinted from [118]. Right: STM image 326 × 364 Å^2 of the C_{60} structure formed on Cu(110) following deposition at 470 K. The structure is a distorted hexagonal overlayer, in which every third row of C_{60} molecules is relaxed, thus forming a structure with a (10 0 1 3) periodicity. The inset shows a higher resolution image 78 × 102 Å^2) of this structure in which both the hexagonal and structure and (1 10 3 0) periodicity are indicated. Reprinted from [119].

bond with surfaces. Substrates that have been evidenced to show a large amount of charge transfer at the molecule–substrate interface when C_{60} is adsorbed include: Si(111) [120], Ag(111) [121] and Au surfaces [122]. A weaker interaction is observed for Pt [123] and Al [124].

C_{60} shows a large degree of epitaxial growth on single crystal surfaces, for example on Bi(0001) [125] and in a HCP structure on Cu(110) [119] (see Figure 25 (Right)). Using the technique of STM sub–molecular resolution is obtainable when C_{60} is chemically adsorbed i.e. not free to rotate. The orientation of this ball–shaped, symmetric molecule relative to the substrate can be determined in such cases. The left hand side of Figure 25 shows a high resolution STM image of C_{60} on Ge(111)–(13 × 13)R14. The unoccupied molecular orbitals (LUMO) are imaged as three lobes [118] indicating that the hexagonal C–rings are parallel to the surface.

C_{60} has been used to probe the reactivity of quasicrystal surfaces and the disordered monolayers formed have been attributed to a strong surface reaction [91, 92]. For C_{60}/ i–Al–Pd–Mn STM analysis showed that there are τ scaled distances be-

tween docked molecules [93]. For adsorption at the aperiodic vicinal Cu surface, the molecules aligned along the steps [94].

4 Experimental Methodology

Ultra high vacuum (UHV) is defined as pressures below $\sim 10^{-9}$ mbar (atmospheric pressure is $\sim$1000 mbar). UHV is required for surface experiments for two reasons: first, to inhibit contamination of the sample surface by gas particles for the duration of the experiment and secondly, so that the path of analysis particles (LEED, Auger electrons etc.) is not impeded by gas particles. UHV is obtained in stages using a series of vacuum pumps. These are attached to a chamber of a size within the extraction volume capacity of the pumps (see Section 4.2).

Using kinetic theory - and taking into account the relative velocity of the gas particles,- the mean free path (λ)(or average distance between particle collisions) of a gas molecule is equal to:

$$\lambda = \frac{RT}{\sqrt{2}\pi d^2 N_A P} \tag{7}$$

R is the molar constant (8.31 $m^2 kgs^{-2} K^{-1}$ mol^{-1}), T is the temperature of the system in kelvin, d is the diameter of the gas particle, P is the pressure of the gas and N_A is Avogadro's constant (6.02×10^{23} mol^{-1}). This expression assumes point–like target gas molecules. For room temperature, atmospheric pressure and using the diameter of an N_2/O_2 molecule the mean free path of such a gas molecule is 1×10^{-7}m. This value is much smaller than a sample–analyser distance in a UHV chamber and therefore particle based analysis techniques are rendered useless. For the same conditions but with a pressure in the UHV regime of 8×10^{-10} mbar the mean free path is increased to 1×10^{6} m. This value is much larger than the typical dimensions of a UHV chamber so an analysis particle has a much greater chance of reaching the analyser.

Similarly the flux of a gas particles at a centimetre square area sample surface can be calculated using the Hertz-Knudsen formula. Consider a surface with a density of around 10^{15} surface atoms per cm^2, that is highly reactive to a typical UHV contaminant like carbon monoxide (CO) so that every incident gas particle at the surface adsorbed. Assume that one CO molecule can adsorb at the surface for every surface atom. At atmospheric pressure the time taken for one complete monolayer to completely adsorb is 2.3 ns, which is too short for any type of measurement. At a low pressure of 8×10^{-10} mbar it would take 72 hours and 40 minutes for the monolayer to adsorb, which is adequate time for an experiment.

4.1 UHV chamber

To obtain an ultra–high vacuum (UHV) environment in which to perform surface experiments the sealed, containing chamber is constructed of a solid, corrosion-resistant, low out–gassing material e.g. stainless steel, mu-metal. High vapour pressure substances are not suitable as they will evaporate, increasing the ambient gas pressure inside the chamber. Gases – like water vapour and carbon monoxide, – are absorbed into the internal walls of the chamber while it is up to atmospheric pressure, hence increasing the time for out-gassing. In general chambers are constructed with a rounded or spherical shape to reduce the surface area relative to the volume of the chamber and hence the amount of gas the chamber is able to absorb when at atmosphere. Various flanges around the chamber are used to attach components and are sealed with rubber or copper gaskets. The knife edge of a steel flange opening cuts into the softer Cu gasket forming an airtight seal.

To accelerate the out-gassing and reach lower pressures in a reduced amount of time the entire chamber is heated to approximately 360 – 430 K (the maximum temperature depends on materials involved). This process is termed baking-out the chamber. After bake-out individual components may be degassed further by being heated up individually to ensure gases are desorbed from the surrounding regions. A well–degassed chamber has an ambient pressure contributed mostly by hydrogen and helium.

4.2 Vacuum pumps

4.2.1 Roughing/Backing Pumps

A roughing pump must be robust enough to pump a chamber down from atmospheric pressure to a low enough pressure for the turbomolecular/diffusion/ molecular–drag pump to start functioning. Such pumps are normally used as backing pumps at the outlet of a turbomolecular pump and therefore must be able to maintain a low enough pressure to enable the optimum pressure gradient for the turbomolecular pumps operation.

Roughing pumps are mechanical pumps, such as diaphragm or rotary pumps. Oil-sealed pumps are reliable, cheap and have a simple pressure vs. pumping rate curve when compared to dry mechanical pumps. There is a risk of hydrocarbon contamination though due to back–streaming oil.

4.2.2 Turbomolecular pump

A turbomolecular pump uses a high speed turbine to push gas molecules out of the chamber volume in successive stages of increasing pressure. The average turbomolecular pump operates in a large range of 10^{-2}–10^{-10} mbar and therefore is very advantageous in obtaining and maintaining UHV. The pump consists of an arrangement of angled rotor blades rotated by a motor at high speeds near that of a gas particle at room temperature -this equates to speeds of a maximum of 9×10^4 rpm. Such a set-up is depicted in Figure 26. As a result the rotor blades effectively deflect the incident gas particles into the pump through the holes in a fixed disk behind it with the same blades/holes called a stator. The particles encounter a series of rotor/stator pairs at increasing pressure until they are eventually expelled from the system by a mechanical pump.

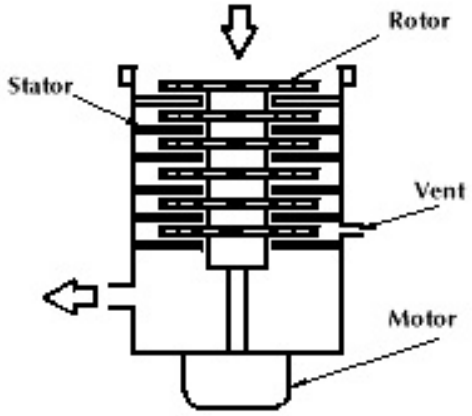

Figure 26: A simple schematic diagram of the internal structure of a turbomolecular pump [126]. The arrows show the direction of the air flow through the pump.

Turbomolecular pumps stall at higher pressures due to the low mean free path of gas particles inhibiting their deflection by the blades into the pump. Some turbomolecular pumps can be cooled slightly to increase the compression of the gas at each stage and magnetic bearings can also be used to reduce frictional heat.

4.2.3 Titanium sublimation pump (TSP)

A titanium sublimation pump (TSP) is a type of 'getter pump' which works most efficiently at lower pressures to remove reactive gases like CO and O_2. A TSP works

by passing a large current enough through a titanium filament to heat it so that the surface layers of titanium sublime and then deposit on the chamber walls. The freshly exposed titanium deposited on the chamber walls reacts with the gases in the chamber to form a stable product therefore removing them from circulating in the chamber.

The titanium is more effective if it is cooled and is mounted so it can deposit on a large area of chamber wall. One must be careful in choosing a position to mount a TSP so that the titanium does not coat and damage essential instruments. TSPs are most successful when used in conjunction with ion pumps to quickly remove residuals from any sudden degassing of the ion pump.

4.2.4 Ion pump

An ionisation (ion) pump is used at pressures lower than 10^{-8} mbar. It is effective at removing most gas particles whereas a turbomolecular pump removes mostly heavier particles leaving a majority of hydrogen and helium particles in the chamber. Figure 27 shows a simple labelled diagram of the inside of a typical ion pump. An ion pump uses an anode–cathode set–up with a few kilovolts applied across them. Electrons emitted from the cathode, are accelerated towards the tube–shaped anodes, ionising gas particles in their path leaving positive ions behind. A permanent magnet forces the electrons onto helical paths to increase the chances of collision. The positive ions are subsequently accelerated towards the titanium coated cathode surface and adsorbed. The gas ions are permanently removed from the vacuum as they either react with the titanium atoms or penetrate deeper into the cathode surface.

4.3 Pressure gauges

It is important to have a real time measurement of the pressure within a chamber so that potential disturbances to the low vacuum can be resolved deftly. There are two types of gauges normally used to monitor pressure: the Pirani gauge -which measures in the range 10-10^{-3} mbar and the ion gauge - measuring normally in the range 10^{-4} mbar-10^{-10} mbar.

A Pirani gauge acts much like a thermocouple in that the resistance measured in a wire is dependent on the temperature of the wire. The heat of a current carrying wire is transferred to gas particles incident on the exposed wire. At lower pressures

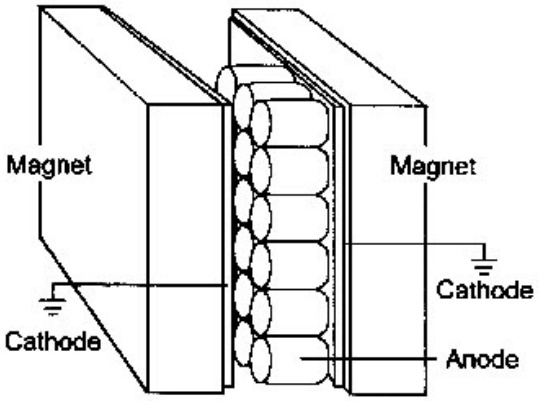

Figure 27: Simple schematic diagram of the internal arrangement of an ion pump (see text).

there are less gas particles to carry the heat away and hence the wire is at a greater temperature. The measure of resistance across the wire at constant EMF is therefore related to the pressure in the chamber.

The most common pressure gauge is an ionisation (ion) gauge which uses a triode arrangement to measure the pressure from a current of ions. The cathode is a hot filament that emits electrons which are then accelerated towards a helical grid at positive potential. The gas molecules within the region of the grid are ionized by the emitted electrons and subsequently attracted towards a cathode wire in the centre of the arrangement. The size of current detected through this cathode is proportional to the pressure in this region of the chamber. A disadvantage of this type of pressure gauge is that the reading is dependent on the type of gas molecule involved.

4.4 Mass spectrometer

A mass spectrometer is able to analyse the composition of background gases in a chamber down to around 10^{-12} mbar. Due to the hot filament used to generate electrons it typically operates at pressures below 10^{-4} mbar. It uses the principle of deflecting ions perpendicular to their trajectory path with a magnetic field. The ions have differing charge to mass ratios and hence are deflected by proportionate amounts by the magnetic component of the Lorentz force. The gas molecules in the path of electrons from the filament are ionised and then a velocity selector set-up

is used to ensure ions with the same kinetic energy enter the analyser. The ions are detected by an electron multiplier arrangement or a Faraday cup. The electrical output is usually a calibrated graphical display of intensity vs. atomic mass.

4.5 Instrumentation

4.5.1 X–ray photoelectron spectroscopy

X–ray photoelectron spectroscopy (XPS)(also known as electron spectroscopy for chemical analysis –ESCA) is a technique mainly used for the quantitative measurement of the composition and chemical state of the surface region of a sample. XPS involves directing collimated, monochromatic x–rays at a sample to excite photoelectrons, with kinetic energy E_k, from the filled core–level states of the atoms. A proportion of the subsequent photoelectrons emitted from the surface are collected by a hemispherical or cylindrical analyser.

Each element has its own electronic configuration – hence characteristic binding energies E_b of the electrons, which enables them to be identified. The number of photoelectrons detected is proportionate to the number of atoms of that species in the sample area probed, enabling calculation of the chemical composition. Following Einstein's relationship for the photo–electric effect:

$$E_b = h\nu - \phi - E_k \tag{8}$$

one can see the binding energy (E_b) of the detected photoelectron can be deduced if the work function (ϕ– the energy required for a photoelectron to escape from the Fermi level to the vacuum) and initial x–ray photon energy ($h\nu$) is known. Therefore, the photoelectron energy spectrum shows the density of occupied states shifted by $h\nu$. This equation applies to a single electron in orbit of an atomic nucleus. In reality the calculation of E_k requires the inclusion of many–body effects from the other bound electrons and conduction electrons in the solid.

The number of electrons detected – the intensity of the spectral line – can be used to calculate the chemical composition in the sample area probed. Spectral lines from Auger emission and final state effects (shake–up, shake–off peaks and plasmon losses) are also seen. Spin–orbit splitting is observed for p, d and f core levels (L–S coupling, $j = l + s$). The ratio of the electrons in each split level is almost element independent enabling easier identification of lines with the same orbital momentum

quantum number.

Bonding to surface atoms and different chemical species in the surface can be determined from the chemical shift of peaks. For example, the removal of an electron to form a bond leaves the other electrons in a more positive potential (there is less core-screening and hence more repulsion). As a result the core–binding energies increase on the order of ∼eV.

Typically, the photoelectrons detected have escaped into the vacuum from the first 10 – 20nm of the sample. The x-rays penetrate a greater depth into the sample (on the order of μms) but the resulting photoelectrons are attenuated by inelastic interactions in the material and recaptured. The surface signal to bulk signal can be improved by using grazing incidence between the surface and analyser. The detected photoelectrons at this angle will have travelled a greater lateral distance through the sample on average therefore decreasing the signal from deeper layers of the material.

Higher resolution and more bulk sensitivity can be gained by using synchrotron radiation, this technique is termed hard x–ray photoelectron spectroscopy (HAXPES). A standard laboratory x–ray source is the dual anode configuration. Electrons produced by a hot filament are attracted towards a water cooled, metallic coated target anode by a high voltage. The high energy electrons collide with anode atoms exciting core–level electrons. Subsequently electrons from less bound outer electronic levels relax to fill the empty core–level state emitting x–rays. The two most common soft x–ray source anodes are Al and Mg. Both metals have dominant K_α emission doublet line (FWHM $\sim 0.7 - 0.8$ eV) [127]. There are other less intense core emission lines on a continuous Bremstrahlung radiation background. Such an unmonochromated x–ray source leads to satellite peaks in the photoemission spectrum from a surface. These peaks may overlap with other emission peaks thus inhibiting peak identification and quantification. An Al K_α ($h\nu = 1486.6$ eV) x–ray beam can be made more monochromatic by being diffracted from the (1010) planes of a quartz crystal.

Hemispherical analysers

Figure 28 shows a basic schematic of a concentric hemispherical analyser which internally consists of two concentric stainless steel hemisphere electrodes. Electrostatic transfer lenses are placed before the analyser to reduce the angular spread of the incident electrons. The voltage of the electrostatic transfer lenses is varied

so that only electrons with a certain kinetic energy pass into the analyser. The constant potential applied between the electrodes acts on the charged particles entering the analyser through the entrance slit bending their projectile path towards the detector. The hemisphere shape of the analyser ensures the beam is focused both parallel and perpendicular to the exit slit. Jost correctors are also placed in the entrance and exit planes to reduce the field distortion there.

The absolute energy resolution ΔE is given by:

$$\Delta E \approx \frac{w^4 d V_i^2}{L^2 V_c} \tag{9}$$

where w is the exit slit width, d is the distance between the electrode plates, V_i is the potential related to the pass energy of the electrons, L is the path length of the electrons and V_c is the potential between the plates. This means that the larger the electrons' path (i.e. size of the analyser) relative to the entrance and exit slit size, the greater the resolution.

The electron detector is usually an electron channel multiplier. This increases the amount of detected electrons; initial electrons collide with the walls of the multiplier to produce cascades of secondary electrons. Hundreds of channel multipliers are placed in an array to make a channel plate, which can produce gains in the detected electron signal up to 10^4.

Photoemission peaks

The spectral lines from photoemission are broadened due to several factors which can be described by a sum of Gaussian and Lorentzian formulae (SGL). The relative resolution of the electron analyser, phonon broadening, the energy width of the initial x–ray used to excite the photoelectrons and temperature dependent effects contribute to a Gaussian peak shape. While the effects of the life–time broadening of the core–level hole state are best represented by a Lorentzian distribution. The choice of background correction algorithm used also influences the shape of the peak to be fitted. The equation fitted to peaks to quantify their area is given by:

$$SGL(x, F, E, m) = (1-m)exp(-4ln2\frac{(x-E)^2}{F^2}) + m(1+4\frac{(x-E)^2}{F^2}) \tag{10}$$

where F is the FWHM of the peak, E is the energy position of the peak and m

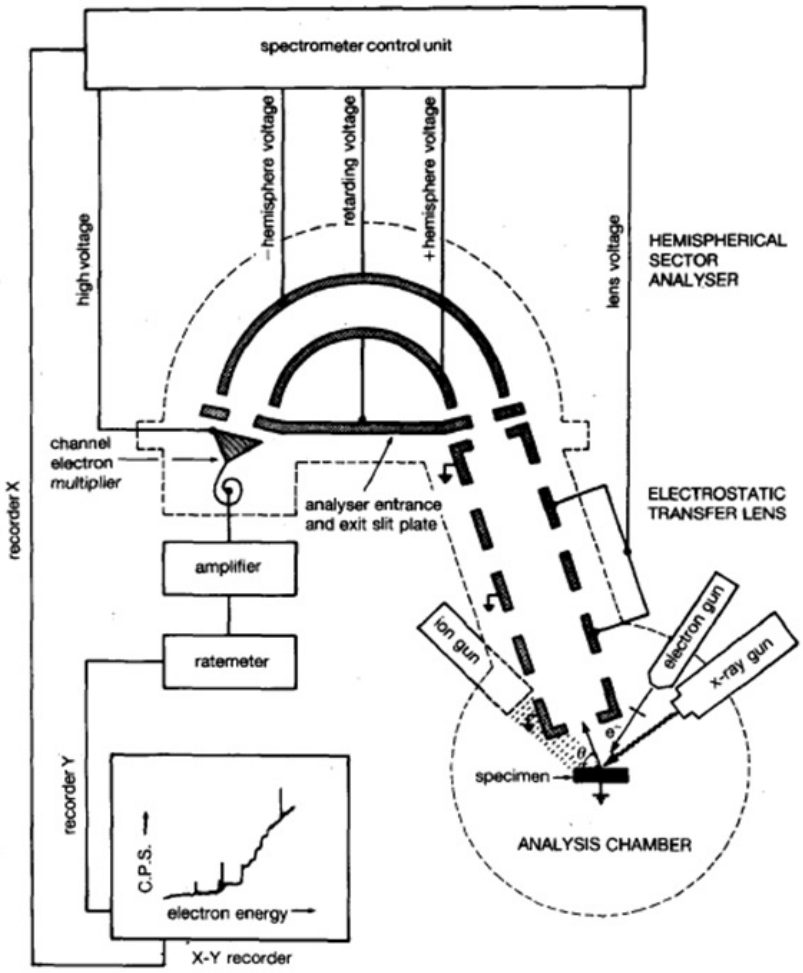

Figure 28: Schematic cross–section of a concentric hemispherical analyser for the detection of analysis electrons emitted from a sample.

determines the intermixing, so that m=1 is a pure Lorentzian and m=0 is a pure Gaussian curve.

Quantification assumes that the surface concentration of a particular atom is directly proportional to the peak intensity and that there is a homogeneous distribution of atoms in the surface. Photoemission peaks from metals have an asymmetry on the higher binding energy side that must be accounted for. This is due to final state effects where the core-hole is screened allowing small excitations above the Fermi energy in the continuum of conduction electrons. A Doniach Sunjic line shape can be fitted to account for this asymmetry. The asymmetry index in this

formula is given by:

$$\alpha = 1 - \frac{HWHM_r}{HWHM_l} \tag{11}$$

where the half at width-half maximum (HWHM) on the left (l) and right (r) are measured. The CasaXPS software is used to fit the components to quantify peaks [128].

4.5.2 Low energy electron diffraction

Low energy electron diffraction is an interference-based surface structure probe. The basic premise of LEED utilises the wave-particle duality of electrons by directing a beam of electrons with a single low energy of around 20eV–200eV at a solid surface. The wavelength (λ) of the electrons is given by the de Broglie relation: $\lambda = h/p$ where h is Planck's constant and p is the momentum of the electron. An angstrom–scale structure acts as an effective diffraction grating for electron waves. The electron clouds of the atoms at the surface deflect incoming electrons back at a fluorescent screen or detector. The redistribution of electron flux at the screen yields information on the symmetry, unit cell size and orientation of the solid surface under investigation. LEED can be useful to qualitatively check order at a surface or quantitatively to determine the structural contents of the unit cell (LEED(IV)). Exposing the surface to the bombarding electrons can be destructive to atomic order and can increase the roughness of the surface, particularly for oxide materials.

LEED is the most widely used surface structure determination technique due to its relatively low expense and ideal wavelength, as well as being surface sensitive at the same low energy. The surface sensitivity is due to inelastic interactions; as the electron beam is strongly attenuated in the first few atomic layers of the surface. The low energy of the electrons ensures the depth of penetration into the surface is only around 0.5 – 1.0 nm, and hence there is no background signal from the bulk structure to be subtracted. The low energy is also required to give a larger scattering cross section for the electrons.

Figure 29 shows a diagram of a typical reverse–view LEED apparatus to be attached to a UHV chamber. In the path of the diffracted electrons there are four grids that ensure an even distribution of elastically scattered electrons reaches the fluorescent screen employed to display the diffraction. The first grid (Grid 1) is

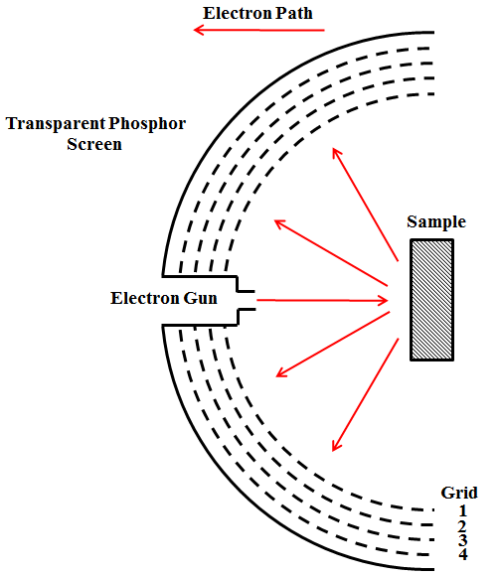

Figure 29: Simple schematic of a rear–view LEED optic. For explanation see the text.

grounded to produce an electric field free region around the sample. Two retarding grids (Grid 2 and 3) are placed at a negative voltage; these grids suppress the lower energy, inelastically scattered electrons which would contribute to the background noise of the pattern on the screen. Grid 4 is grounded to provide a region where the electrons that pass Grid 3 are accelerated towards the positively biased screen. Cooling the sample can reduce thermal vibrations of the atoms in the sample that contribute to the background intensity. The attenuation of the intensity due to thermal motion can be described using the Debye–Waller factor (DWF), given by the time averaged relationship:

$$DWF = \left\langle e^{i\Delta K \cdot u} \right\rangle^2$$

where u is the position of the scattering centre (i.e. atom).

Reciprocal space and diffraction

Periodic functions – like those that represent the translational invariance of a crystal lattice (see Section 2.2),– can be represented as a Fourier series. The Fourier

representation of a function with translational invariance in one-dimension, $f(x + a) = f(x)$, is:

$$f(x) = \sum_n a_n e^{2\pi nx/a} \tag{12}$$

The Fourier coefficients can be labelled by $g = 2\pi n/a$, g is called a reciprocal lattice vector. For the three–dimensional case, $f(r + R) = f(r)$, the representation is:

$$f(n) = \sum_G A_G e^{i\vec{G}\vec{r}} \tag{13}$$

where $e^{i\vec{G}.\vec{R}}$=1 for all $\vec{R}$, $\vec{G}$.

As in Eqn. 1 for the base vectors of a direct lattice ($\vec{R}$), the reciprocal lattice vectors are defined as:

$$\vec{G} = l_1\vec{b_1} + l_2\vec{b_2} + l_3\vec{b_3} \tag{14}$$

where l_1, l_2, l_3 are integers. Each reciprocal lattice vector is perpendicular to a set of lattice planes denoted by the Miller indices [h, k, l]. The reciprocal lattice vectors - $\vec{b_1}$, $\vec{b_2}$, $\vec{b_3}$, must satisfy:

$$\vec{a_j}.\vec{b_j} = 2\pi\delta_{i,j} \tag{15}$$

Using this condition Eqn. 14 can be solved to give relationships between the reciprocal space and real space vectors:

$$\vec{b_1} = 2\pi\frac{\vec{a_2} \times \vec{a_3}}{\vec{a_1} \cdot \vec{a_2} \times \vec{a_3}} \quad \vec{b_2} = 2\pi\frac{\vec{a_3} \times \vec{a_1}}{\vec{a_1} \cdot \vec{a_2} \times \vec{a_3}} \quad \vec{b_3} = 2\pi\frac{\vec{a_1} \times \vec{a_2}}{\vec{a_1} \cdot \vec{a_2} \times \vec{a_3}} \tag{16}$$

The simple Ewald Sphere construction depicted in Figure 30 a), b) can be used to help envisage where diffraction peaks occur. Using the case of a 2–D, simple cubic lattice for the geometric representation of a crystal structure the corresponding reciprocal lattice is pictured. An exact truncation of the bulk leads to crystal truncation rods (CTRs) of intensity perpendicular to the surface. A lattice point (0,0)

is taken as the lattice origin. By considering incident radiation of initial wavevector $\left|\vec{K_i}\right| = |2\pi/\lambda|$ perpendicular to the surface normal an Ewald circle of radius $\left|\vec{K_i}\right|$ is drawn about the origin. The outgoing final wavevector, $\left|\vec{K_f}\right|$ is orientated so that it ends in the centre of the sphere. As a result the beginning of the outgoing wavevector lies on the Ewald circle. The resulting scattering vector $\Delta\vec{K}$ joins the beginning of the outgoing wavevector and the origin. For constructive interference to occur the scattering vector must start and end on a reciprocal lattice point. Using the Laue conditions for diffraction one can see that $\Delta\vec{K}$ is a vector of the reciprocal lattice. Therefore, diffraction peaks are defined by the reciprocal lattice, occurring at:

$$\Delta\vec{K} = \vec{G_{hkl}} = h\vec{b_1} + k\vec{b_2} + l\vec{b_3} \tag{17}$$

For surface rods there are many more coincidences possible for $\Delta\vec{K}$ and hence more scattering vectors. This holds true as long as the wavelength of the incoming radiation is less than the smallest real space, lattice distance. As the initial wave vector is increased the radius of the Ewald sphere increases also, and hence the intensity of the diffraction peaks varies as the sphere moves across the k-space rods. This means that the lower the electron beam energy the longer the range of order being observed at the surface. Not all of these peaks are seen in the diffraction pattern, as only the scattering vectors towards the surface represent the electrons in the observation region of the LEED apparatus. Using this pictorial representation one is able to find all scattering vectors $\Delta\vec{K}$. The surface termination leading to the presence of CTRs means that the intensity of a reciprocal lattice spot never goes to zero as the electron beam energy is varied.

LEED from quasicrystal surfaces

Diffraction is the main technique for the analysis of ordered surface structures and the discovery of quasicrystals led to new challenges in the interpretation and modelling of diffraction patterns. The Fourier transform of a Fibonacci array (see Section 2.3 for an introduction to the Fibonacci Sequence) leads to an infinite number of peaks but only a few of appreciable intensity. LEED patterns from quasicrystals show inflational symmetry; the discrete peaks are arranged aperiodically but symmetrically about the origin [129]. This is similar to that observed in diffraction

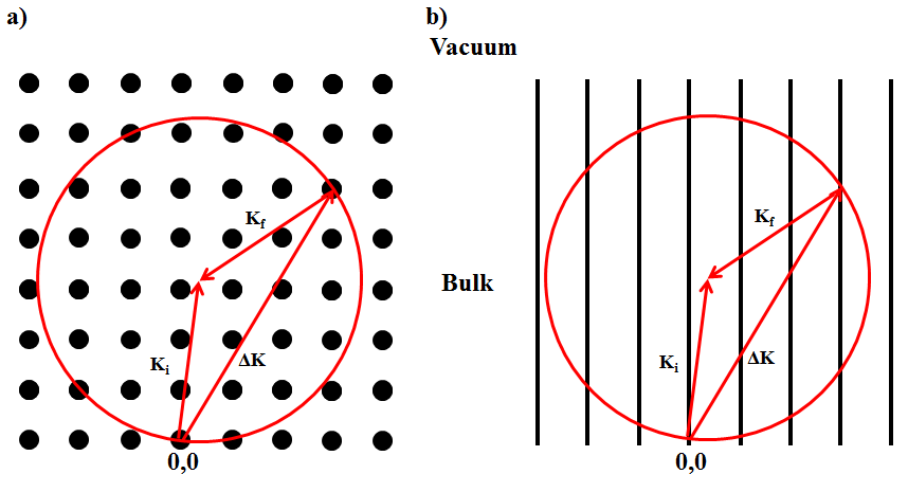

Figure 30: A 2-D simple cubic, reciprocal lattice, truncated at the surface is shown. The Ewald sphere of incident wave vector $\vec{K}_i$ is used to derive all possible scattering wave vectors $\Delta\vec{K}$. a)Top view b)Side view of 2–D Ewald construction.

from quasiperiodic arrays.

The intense diffraction spots from quasicrystal samples are described by Generalised Miller Indices as there is no discrete unit cell. For example: an icosahedral quasicrystal structure can be described by 6 indices:

$$G = h_1\vec{a}_1 + h_2\vec{a}_2 + h_3\vec{a}_3 + h_4\vec{a}_4 + h_5\vec{a}_5 + h_6\vec{a}_6 \tag{18}$$

h_i are integers and $\vec{a}_i$ are the reciprocal basis vectors. The reciprocal basis vectors take the form of vectors pointing from the centre to the vertices of an icosahedron - as shown in Figure 31 a). The equivalent Cartesian components of the vectors are:

$$\vec{a}_1(1,\tau,0)\ \vec{a}_2(\tau,0,1)\ \vec{a}_3(\tau,1,0)\ \vec{a}_4(0,1,-\tau)\ \vec{a}_5(-1,\tau,0)\ \vec{a}_6(0,1,\tau) \tag{19}$$

The indexing of Cartesian components up to a certain length scale are 1 and τ.

An example of a LEED pattern obtained from an i-AlPdMn surface along the 000001 fivefold direction is shown in Figure 31 b). A schematic of the pattern is overlaid for clarity. The indices of the other five directions of the diffraction spots of the two-dimensional surface reciprocal lattice relative to the normal surface direction are labeled.

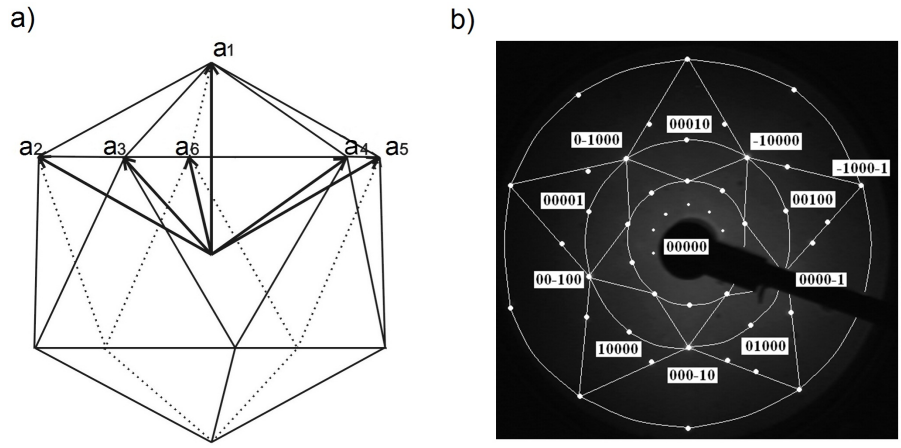

Figure 31: a) An icosahedron with the directions of the 6 basis vectors used for indexing the diffraction pattern marked. b)LEED pattern obtained from the clean fivefold surface of i-AlPdMn.(Beam energy 100 eV). Indices of the major spots are labeled.

4.5.3 Scanning tunnelling microscopy

Scanning tunnelling microscopy (STM) scans the charge density of the top–most layers of a surface under study, which often corresponds to the topographical surface structure. This technique was the first to enable imaging of an individual atom's charge density and observe surface structure in real–space. It utilises the quantum mechanical tunnelling of electrons between a conducting/semi–conducting sample and a very fine tip to give precise control over the variation in height (z) or the change in current detected (I). An x–y raster scanner enables complete topographical scans of a region of the surface. By moving a conducting tip – biased with regard to the sample,– to within a few nanometres of the surface to be scanned, a classically forbidden tunnelling current occurs across the gap (of the order of around 1 nA). The tunnelling current (I) between the tip and sample has an strong dependence on the tip–sample distance (d) due to the exponential decay of the electron wavefunction into this classically forbidden vacuum region. This is expressed by the equation:

$$I(d) \propto e^{-Kd} \tag{20}$$

where $K = \sqrt{2m\phi}/\hbar$ is the decay constant of the wavefunction at the Fermi level. ϕ is the potential of the tunnelling barrier or average work function of the tip and sample. As a result the variation in current (constant height mode) or height

(constant current mode) maps the charge density of the surface atoms; specifically the local density of states near the Fermi level is detected.

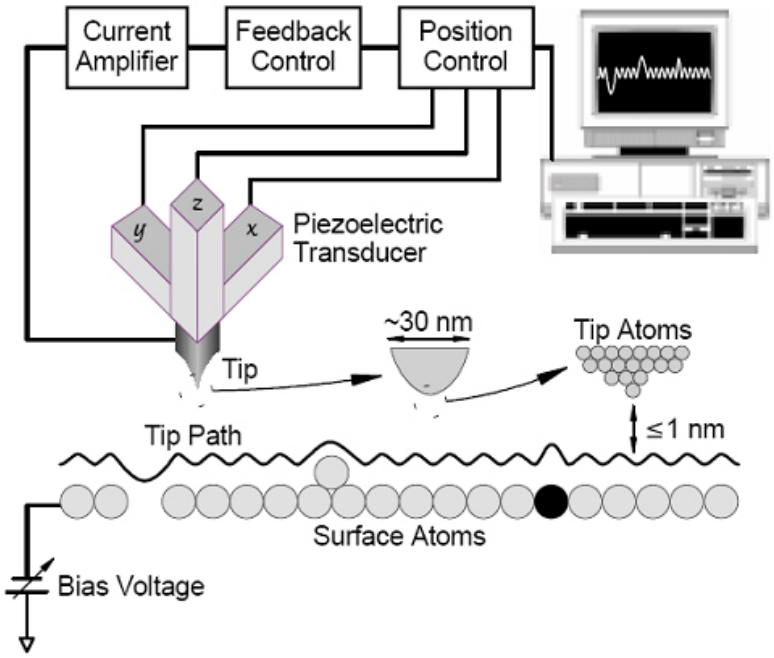

Figure 32: Basic elements of scanning tunnelling microscope [130].

Figure 32 shows a simple diagram of a typical STM set–up. Modern STMs use an inertial slider for coarse movement of the tip and sample surface to be scanned. Sensitivity of tip position in the x, y and z axes to changes in current is given by an electrical feedback circuit and a scan head with arms made of a piezoelectric material (e.g. quartz). Such a material possesses the property that its macroscopic dimensions change when a voltage is applied across the material. Typically ceramic piezo–electric materials are used which are polarised by being cooled in an electric field. One of the most common piezo–electric geometries is the tube scanner that is bent to track in the surface plane [131]. The current amplifier converts the small tunnelling current to a measurable voltage and therefore a logarithmic amplifier (op–amp with a diode) is required. Specialist SPM software installed on a connected computer controls the inputs of the scanning circuit and displays the scan results.

For a given tip there will always be a single atom closer to the surface than the others, since the tip–sample separation has an exponential influence on tunnelling current atomic resolution is possible with any tip. At a single position and instant

the wavefunctions of a single sample and an individual tip atom overlap and the detected current is a convolution of these electronic states. A sharp tip reduces the chances of artifacts in the topograph such as multiple tips etc. The material used for conducting tips is unreactive and/or of high strength. Materials used as scanning tips include Au, Ag, W, Ni, Pt and PtIr. For the experiments in this project high purity W tips were used. The tips were made by electrochemically etching a length of W wire suspended in a meniscus of KOH solution. The condition of the tips were checked with an optical microscope before being mounted and inserted into the STM instrument.

The different materials used for the STM components must have similar thermal expansion coefficients to ensure that the instrument remains structurally robust during heating and cooling e.g. bake–out. The material of the components must also have a high resonant frequency (> 1 kHz) so parts of the system do not oscillate during measurement hence inhibiting imaging and increasing the probability of the tip and sample touching. STM instruments are always isolated from external mechanical vibrations by suspending the instrument stage on springs combined with eddy–current dampening or air–pneumatic table legs.

In some systems the sample can be cooled (e.g. with LN_2) to limit surface diffusion processes and atomic thermal vibrations in the surface. STM systems have been modified to suit purposes other than topographical imaging. For example spin–polarised STM is used to image the local magnetic structure and low temperature atomic manipulation of individual atoms at the surface has been demonstrated.

STM from quasicrystal surfaces

Due to the complex structure of quasicrystals STM is useful to probe the wide–range of local structural features on a quasicrystal surface that is bulk terminated. The unusual low electronic conductivity of quasicrystals for a mixture of its metallic constituents, due to the localization of electrons, enables clearer imaging of the surface. STM was first applied to the study of quasicrystal surface structure of d–Al–Co–Cu [132] and has been successfully utilised to observe the self–assembly of adsorbed atoms at quasiperiodic surfaces – see Section 3.2 for examples.

4.6 Sample preparation

Single–grain quasicrystal ingots can be synthesised using normal crystal growth techniques e.g. Bridgman, flux-growth. The most common technique used to grow quasicrystal samples is the Czochralski technique. The set–up for this technique is shown in Figure 33, where a seed crystal is pulled at a very slow rate from a melt of the sample composition. The even shape of the ingot is increased by rotating the pulling rod. The temperature of the furnace at the growth front is set so that a meniscus forms at the solid–liquid interface. A sample with a certain crystallographic orientation can be grown using a seed crystal of the same phase and orientation, this is termed homogeneous growth. Quasicrystal samples are cut along the required crystallographic direction from the ingot grown. The quality of the sample structure is then determined using x–ray or electron diffraction.

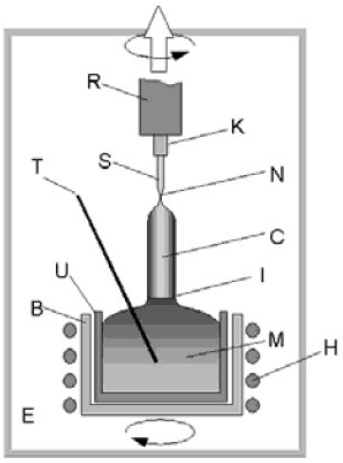

Figure 33: Set–up used in the Czochralski crystal growth technique. C: crystal grown M: melt U: protecting envelope E: heater, R: pulling rod, N: thin neck, S: seed crystal, K: seed carrier, T: thermocouple, B: susceptor. Reprinted from [133].

The quasicrystal samples are carefully polished to significantly reduce the surface roughness on the macro–scale. The surface is polished with different grade diamond paste (0.25 - 6 μm) and rinsed with methanol between stages. The sample is then cleaned of contaminants using an ultra–sonic bath of methanol. The resulting surface is sufficiently flat for many surface science techniques.

The dried sample is subsequently mounted on a plate designed for transfer and treatment in the vacuum system. The plate is normally made of Mo, Ta or Cu and

the sample is spot welded to the plate with Ta wires or strips.

Quasicrystal samples are treated in–situ to produce a bulk–truncated surface by cycles of sputtering and high–temperature annealing. Contaminants are cleaned from the surface by ion bombardment (generally referred to as sputtering) with noble gas ions (e.g. Ar, Ne). The sputter ion gun is operated at grazing incidence relative to the sample so as to increase the surface flatness and to avoid embedding of sputter gas atoms in the surface layers. The lines containing the noble gas are over–pressured (above atmosphere) to stop diffusion of atmospheric gas into the line. The noble gas pressure is flowed at a high enough pressure to produce an emission current in the order of 10^{-3}A. The ion density and mean free path are optimised to maximise the ion current detected at the sample. Sputtering removes the surface layers to produce a off–stoichiometry, disordered surface. In the case of quasicrystals sputtering has been shown to produce nano–crystallites at the surface [50].

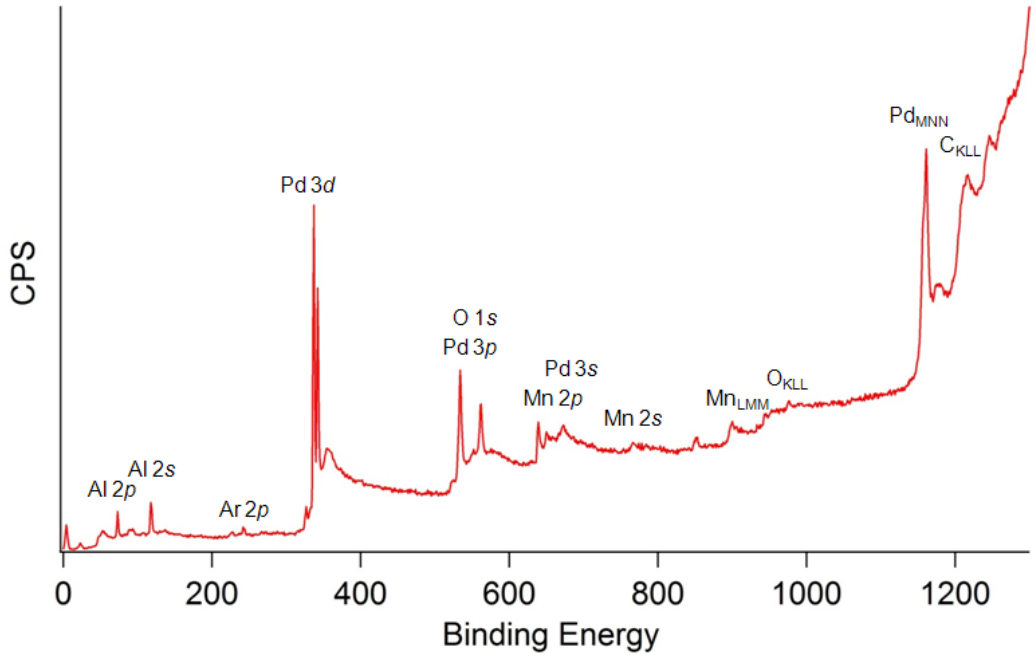

Figure 34: A survey XPS spectrum obtained from the surface of i–Al–Pd–Mn after a sputter cycle of 75 minutes length.

As an example of the effects of UHV preparation on a chemically complex surface, Figure 34 shows an XPS survey scan from the i–Al–Pd–Mn five–fold surface. After being introduced to the UHV environment the surface has been sputtered for 75 minutes with Ar+ at 2.5 keV. The XPS spectra are used to calculate the atomic fraction

of elements in the sample region scanned by fitting the area of each bulk peak and taking the element sensitivity factors into account assuming an even distribution of elements in this region. The XPS spectrum shows that the chemical composition of the surface has changed from the bulk composition of $Al_{70.5}Pd_{19.5}Mn_{8.5}$ to $Al_{60.4}Pd_{28.7}Mn_{11.0}$. The depletion of Al in the surface layers demonstrates that the Ar ions preferentially removes the element with the least mass from the surface. It is also notable that there is only a very small oxygen O_{KLL} signal present. Further sputtering cycles were applied to the sample for a period of half an hour with a lower ion kinetic energy.

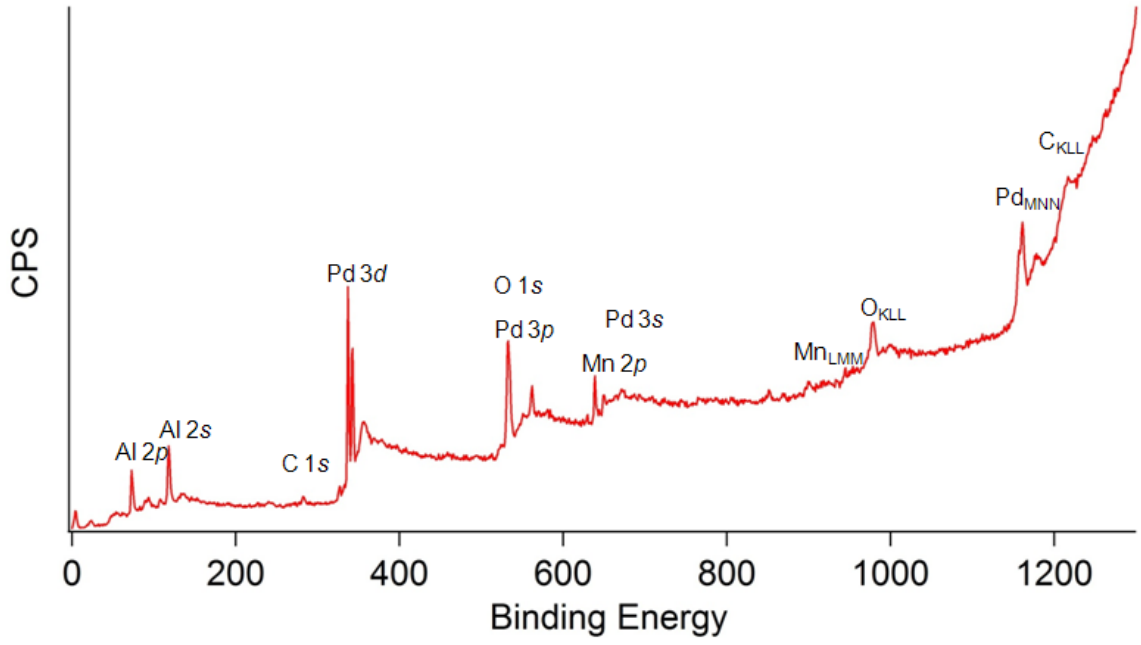

Figure 35: A survey XPS spectrum obtained from the surface of *i*–Al–Pd–Mn after an anneal of 3 hours.

Following sputtering, the sample was then heated in UHV to near melting temperature to use the thermal energy to restore bulk composition at the surface. This process is termed annealing the sample. It is carried-out using *e*–beam or thermionic heating applied behind the sample plate on the manipulator arm. The initial annealing conditions used were 3 hours at a temperature of 920 K. The time for subsequent anneals was 2 hours. Prolonged annealing enables the formation of larger flat terraces which are sufficient to produce clear LEED patterns and improve STM scans.

Longer anneals at higher temperatures may yield pits and voids in the terraces. Figure 35 shows a survey spectrum from the surface following the first anneal of 3 hours. There is an increase of the O $1s$ and O_{KLL} signals and also a small C signal. These contaminants are due to diffusion from the bulk of the sample and from degassing of the surrounding area e.g. the sample plate. The surface is now Al rich with a calculated composition of $Al_{82.2}Pd_{11.5}Mn_{6.3}$.

4.7 In-situ evaporation

Physical vapour deposition is used to form epitaxial thin films in UHV. This technique involves the sublimation of a high-purity evaporant source towards the sample surface. The two types of evaporators used to accomplish this are the Knudsen cell and electron beam evaporators (e–beam).

Knudsen cell evaporators use conductive and radiative heating provided by a filament (usually W) to evaporate the material from a rod or container. This type of evaporator is used for materials with low melting points e.g. noble metals.

Electron–beam evaporators use electron bombardment to locally heat a rod or crucible containing evaporant. Thermally emitted electrons from a filament are attracted towards a positivity biased rod or crucible. Crucibles are normally constructed from alumina, molybdenum or stainless–steel. The evaporant can reach higher temperatures than in the Knudsen cell evaporator and since the electron beam is directed at the evaporant the out-gassing of the surrounding surfaces is reduced during operation.

5 Growth of Bi on the fivefold surface of *i*–Al–Pd–Mn

5.1 Introduction

One of the first, successful, single element quasicrystal overlayers produced was Bi on the *i*–Al–Pd–Mn quasicrystal [76]. The substrate structure has been previously described in Section 2.8.1. Bulk Bi is a semi–metallic element with an arsenic type atomic structure. This structure has a body–centred cubic (bcc) lattice structure that can be considered as a slightly distorted simple cubic structure.

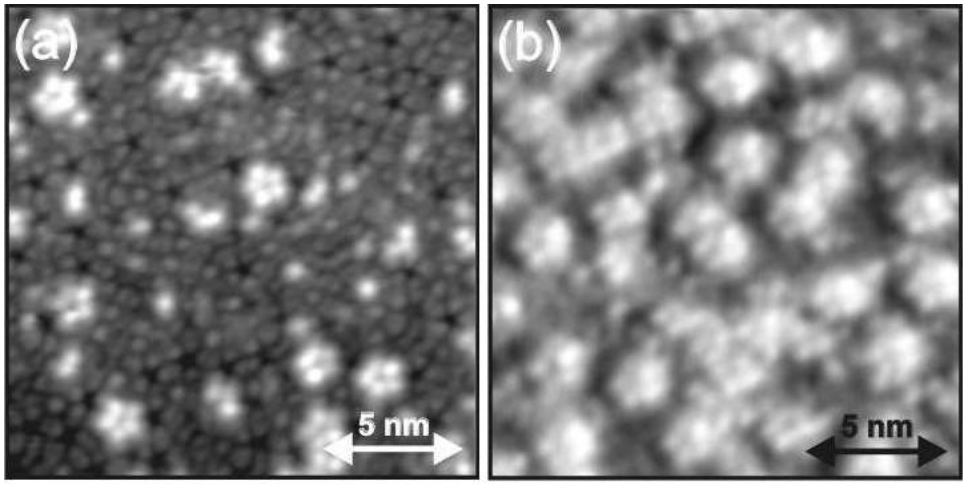

Figure 36: Overview of the nucleation and growth of the Bi monolayer by room temperature deposition on *i*–Al–Pd–Mn. (a); 0.54 ML Bi; (b); 0.9 ML Bi. Reprinted from [134].

The Bi / *i*–Al–Pd–Mn system exhibits a Stranski-Krastanov type growth mode of Bi on the surface. The Bi forms a complete quasiperiodic overlayer evidenced by the observation of a fivefold LEED pattern similar to that from the clean surface. Bi then forms rectangular, multilayered islands of mostly 4 ML and 8 ML which at higher deposition eventually coalesce [135]. The rectangular, nano–crystallites grow with the (100)–pseudocubic ({012}–rhombohedral) directions parallel to the surface normal.

Previous sub–monolayer coverage STM studies show that Bi initially adsorbs in pentagonal clusters with an edge length of 4.9 Å, as shown in Figure 36. From a

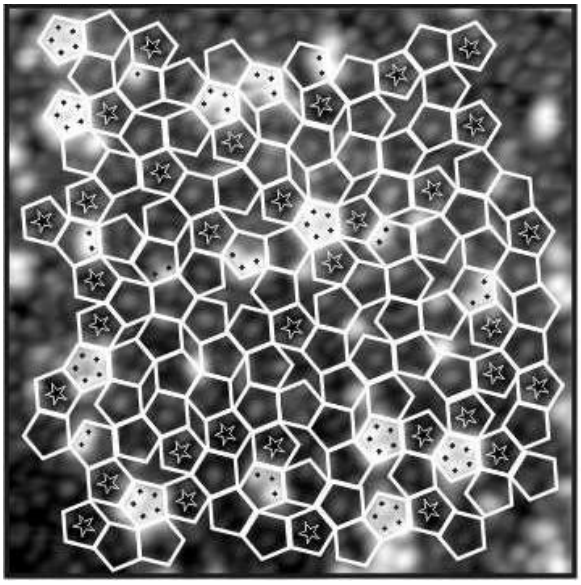

Figure 37: The five–fold surface of i–Al–Pd–Mn with a Bi coverage of 0.13 ML. A Penrose P1 tiling edge length 7.8 Å has been superimposed. Bismuth atoms only decorate top pentagonal tiles and many of the bottom pentagonal tiles enclose a five–fold depression (dark star). These are indicated with a star motif. Reprinted from [134]

tiling analysis it was determined these Bi clusters form inside 'top' pentagon tiles that contain an equatorial truncation of the pseudo–Mackay clusters with a Mn atom in the top plain [134] (see Figure 37). The nucleation sites that enable the formation of these nano–clusters are dense enough so that the fivefold order translates to the atoms that adsorb between them. The result is an aperiodic network of Bi atoms with fivefold rotational symmetry.

Figure 38 demonstrates the similarity of the LEED patterns recorded for the clean surface and after the deposition of a monolayer of Bi. The pattern appears 10–fold but as the beam energy is varied alternate spots in a decagonal ring have differing intensity. The spots are at the same positions for both the clean surface and Bi monolayer (principal spots are in a 1×1 pattern) and the behaviour of the intensity as the beam energy is varied are observed to be the same. Such a result indicates pseudomorphic growth of the monolayer. The presence of more spots in the pattern from the Bi monolayer is due to the larger electron scattering cross section for Bi atoms compared to the clean surface atoms and not as a result of surface reconstruction or instrument parameters [136].

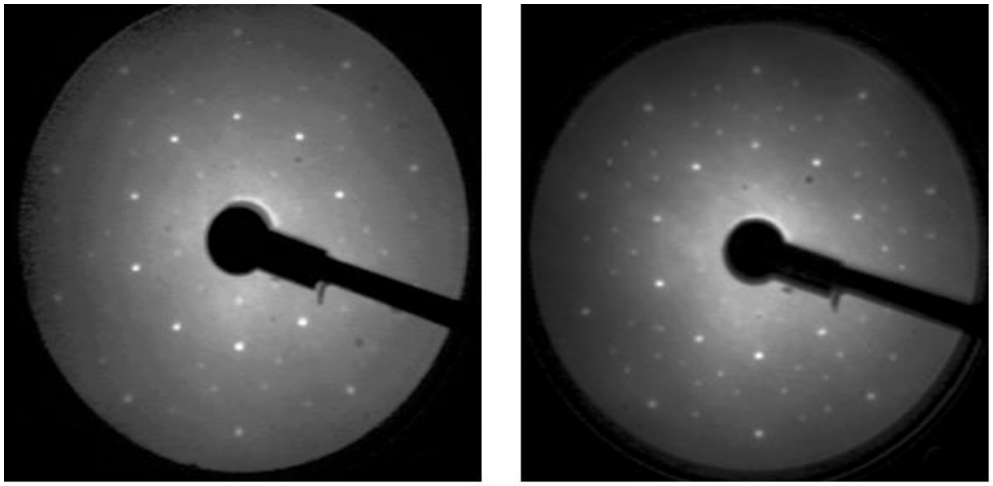

Figure 38: LEED pattern recorded at 117eV. Left: Clean surface of i–Al–Pd–Mn. Right: 1ML of Bi deposited.

In the current experiment XPS, LEED and STM were employed to characterise the evolution and thermal stability of the Bi thin film. The morphology of the nano-crystalline islands is monitored as a function of evaporant flux, coverage and time.

5.2 Experimental details

The fivefold surface of a single grain i–Al–Pd–Mn sample with a nominal composition of $Al_{70.5}$–$Pd_{19.5}$–$Mn_{8.5}$, was prepared using the method described in Section 4.6. The sample temperature during anneal was measured using a previously calibrated optical pyrometer. The long range surface order of the material structure was confirmed after a preparation cycle by the observation of a fivefold LEED pattern (see Figure 38). Therefore, the surface is deemed to have large terraces of the icosahedral quasicrystalline structure over a length scale larger than the coherence length of the electron beam.

The x–ray source employed used an Al anode target (principal x–ray energy line Al Kα =1486eV) with approximately 64 mA emission current incident on the anode. The photoelectrons were collected and analysed using a PSP Vacuum Technology hemispherical electron-energy analyser. The scans were taken in constant analysis energy mode; for example: a concentric pass energy of 50 eV was used for survey scans. Normal incidence to the analyser was taken as 15° (position of 161° azimuth

Spectroscopic line observed	Sensitivity factor (S)
Al2p	0.160
Al2s	0.193
Pd3d	4.642
Mn2p	2.420
Bi4f	7.632
O1s	0.711

Table 2: Sensitivity factors for core levels and AlKα x–rays.

on the manipulator) to avoid the majority of x–rays being directed at side of sample plate. Grazing angle was taken at 60° (at 75° to analyser normal) to this arrangement (position of 101° on the manipulator). The angular acceptance of the analyser is 8°.

The amount of Bi deposited on the surface was calibrated using XPS intensity measurements of the Mn 2p, Pd 3d, Al 2s, Al 2p and Bi 4f core–level photoemission peaks as the dose was increased. The estimated coverage was therefore a dose equivalent to the monolayer, quoted as monolayer equivalent (MLE). The elements in the sample may be less sensitive (possess a smaller cross–section) to the absorption of a particular x–ray wavelength used to probe the sample. Table 2 lists the sensitivity factors used for the main spectroscopic peaks measured. These are empirically derived Scofield sensitivity factors modified to account for the electron lens transmission and an angle of 90° between the x-ray source and the analyser entrance slit [137]. Aluminium has the lowest sensitivity factor for the components in the system so there are quite low statistics on Al core–level peaks even though the majority of the sample is composed of Al.

To fit the peaks in the region scans a Shirley type background is applied to the data in the region of a peak. A Gaussian–Lorentzian shape is fitted to the peaks to calculate the relative contributions from different elements present (see Section 4.5.1). The peaks from metals are asymmetric, and hence a Gaussian–Lorentzian may not accurately fit the peaks. A hybrid Doniach Sunjic/Gaussian–Lorentzian (sum) line–shape with a small asymmetry parameter is fitted where a Gaussian–Lorentz combination is not satisfactory [138].

Preliminary work to calibrate the temperature of the sample adopted the same experimental conditions as the desorption experiment. This included heating the sample for a total of 10 minutes at the same power and leaving the for sample to cool

for 5 minutes (to below the lower temperature limit of the pyrometer) in between heating intervals.

Bi atoms were deposited on the sample surface using an Omicron EFM–3 electron beam evaporator. LEED patterns are recorded with an OCI low current MCP LEED apparatus. The STM data is taken using a Omicron RT–STM and an Omicron VT–STM (with the sample kept at room temperature) with a chemically etched W tip. The data is processed and analysed using the software Gwyddion [139]. The base pressure in the chamber was 5×10^{-10} mbar.

5.3 Results

XPS results

The graph of Figure 39 shows the Al (substrate) and Bi peaks intensities as a function of increasing deposition time. Similar curves were calculated for the Pd $3d$ and Mn $2p$ core–level peak intensities. Each plot has an inflexion point between the same two depositions within experimental error. The substrate peak intensity change between depositions at greater coverages decreases after this inflexion point. Straight line fits to the points in each apparent region are extrapolated to highlight the point at which the change in gradient occurs. From the two lines fitted to the curve it can be deduced that a monolayer occurred at a deposition of 11 minutes at 400 nA flux. This deposition parameter was used to calibrate dosage deposition for different coverages. The errors for the peak ratios on the deposition diagram (Figure 39) were calculated from the average fluctuations in the background counts. The linear variation of the curve and lack of further breaks at greater coverage supports a Stranski–Krastanov type growth mode (initial layer plus island formation). This growth mode is consistent with previous STM and LEED results from this study.

The growth morphology was also investigated by desorption of the multilayer and monolayer. The stability or strength of bonding of the Bi multilayer and the Bi monolayer to the quasicrystal substrate can be roughly inferred by the desorption. The sample with a total of 56 MLE of Bi deposited was heated to the given temperature for a duration of 10 mins and allowed to cool for 5 minutes before taking relevant XPS scans.

If there was a significant desorption of Bi at a given temperature the heating was repeated at that temperature until all the Bi able to desorb at that temperature is

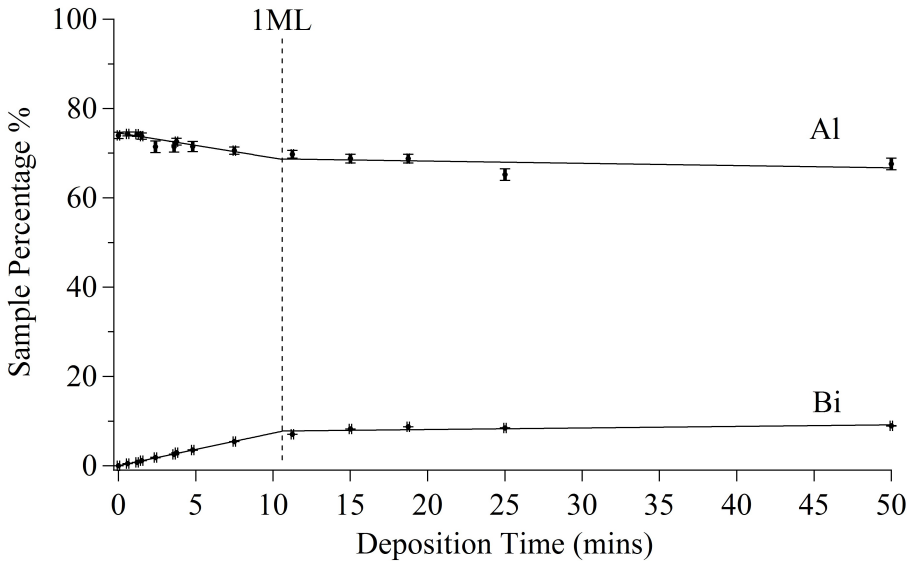

Figure 39: Deposition curve showing the variation in Al 2p and Bi 4f intensity as a function of deposition time. Fitted line segments of different gradients are shown. The Al 2p intensity is normalised with respect to the clean surface and Bi 4f intensity is normalised to the peak intensity and after 50 mins Bi deposition.

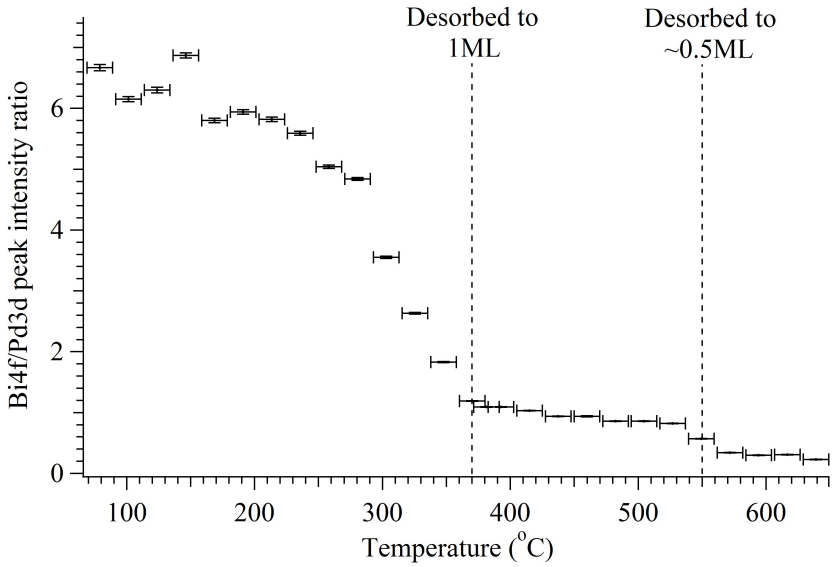

Figure 40: Desorption of Bi from the substrate starting from a total coverage of around 56 MLE. The plot shows the ratio of the Bi 4f to Pd 3d photoemission peak intensities as a function of increasing sample temperature.

removed. By this method the temperatures at which the multilayer and monolayer desorb was obtained. Typically, adsorbate–adsorbate bonding strength is less than that of adsorbate–substrate bonding; the monolayer desorbs at a temperature above that of the less bound multilayer. In this way the substrate to adsorbate intensity ratio for the monolayer can be accurately determined and compared to the ratio found during the deposition experiments.

The plot in Figure 40 shows that the multilayer desorbs between 520 and 620K. This temperature agrees with previous studies which found the multilayer completely desorbed at 620K leaving a monolayer [135]. The monolayer coverage corresponds to the region where the spectra peak intensities recorded were constant for a large temperature range of 620 – 800 K. The ratio of peak intensities of Pd $3d$ to the Bi $4f$ matches well with that of the monolayer transition in the deposition curves.

The monolayer desorbed abruptly at 820K leaving around ∼0.5 of a monolayer. The signal from this coverage remained even at 910K. This stable sub–monolayer coverage may be the point at which saturation of the island nucleation sites occurs and the pure growth regime begins leading to the completion of the monolayer [140]. This temperature is significantly higher than that reported in a previous study where the monolayer was estimated to desorb between 670K and 870K [76]. However this estimate was inferred from an observed structural change without any direct chemical information.

Throughout the experiment the Bi overlayer passivated the surface from contamination under UHV for extended periods of time. There is no O_{KLL} peak present in scans of greater than a monolayer coverage after a period of 3 days. The Bi $5d$ peak coincides with the O $2s$ peak and the Pd $3d_{3/2}$ peak coincides with the O $1s$ peak. Even so the ratio of Pd $3d_{3/2}$ to Pd $3d_{1/2}$ is maintained after this period and there would be larger peaks for this high coverage at around 24 eV and 536 eV if oxygen was present on the surface.

STM and LEED results

Prior to STM measurements around 4.1 MLE of Bi was deposited on the sample. The coverage was checked with an XPS survey scan. It was observed that it takes several hours for Ostwald ripening of the islands to occur, which equates to the time required for Bi to diffuse over the surface to form larger, more stable islands.

Initially irregular-shaped islands with a height of 2 ML were observed (consistent with observations in previous studies [135]). These islands are seen transforming into to regular (100)–pseudocubic ({012}–rhombohedral) islands with time. Figure 41 a) shows an STM image of an irregular, 2 ML high island next to a stepped, rectangular, {012}–rhombohedral island where the lowest layer is 4 ML.

After several hours, stable rectangular islands were observed on the substrate. A large scale image of many rectangular islands is shown in Figure 41 b). The multi-layer islands themselves have a step–like structure which reflects the appearance of the macroscopic, hoppered, bulk Bi crystals. Large scans of regions with numerous islands were recorded to enable a statistical analysis of the type of island present. Around 92% of the islands measured are rectangular. 12% of the rectangular islands have joined onto others as they have grown and formed 'L'–shapes. Islands with as many as 24 layers were measured. There was no orientational alignment measured between islands.

The LEED pattern obtained from the same Bi coverage as in Figure 41 b) is displayed in Figure 41 c). There is a large diffuse ring feature, which indicates a lack of orientational alignment of this pseudocubic phase with the substrate. Upon inspection, the ring is measured as coincident with the (22001) ring of the clean, quasicrystal surface [141]. This ring has a wavevector radius of k = 1.94 $Å^{-1}$ corresponding to a real-space distance of 3.24 Å. From the width of the diffuse ring (< 0.05 Å), the error on this distance is estimated to be around <0.1 Å, making the observation consistent with the Bi {012} inter-planar spacing of 3.28 Å [142].

As the size of the pseudocubic islands increases there is a morphological transition to larger, triangular islands. Several of these islands are shown in the STM image of Figure 42 a). These islands are oriented with the {111}–rhombohedral ((0001)–hexagonal) plane parallel to the surface. This is the preferred epitaxial allotrope of Bi and the natural cleavage plane [143]. The resultant film is much flatter than the pseudocubic islands; with a coverage of 4.1 MLE, the maximum number of layers in an hexagonally ordered triangular island is 6. These single–domain triangular Bi islands grow to a large lateral size, with the largest surface area observed being in excess of 0.25 μm^2. Figure 42 shows an atomic resolution image of the hexagonal surface arrangement.

A clear LEED pattern from the triangular islands was observed after deposition of 6 ML, displayed in Figure 42 c). The pattern shows a ring of 30 spots regularly

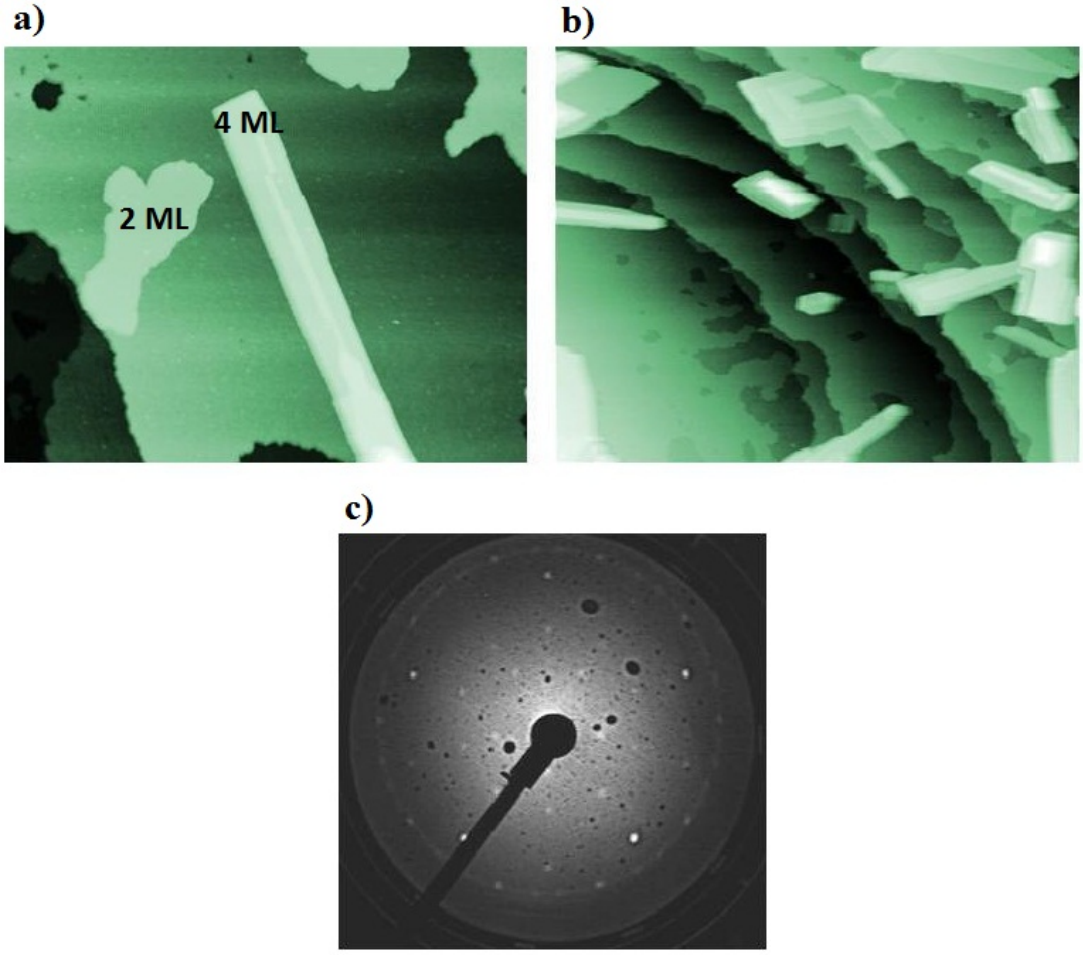

Figure 41: a) 506 nm × 394 nm image of 1.8 ML deposition of Bi, flux 0.07 $MLmin^{-1}$. b) 395 nm × 500 nm Coverage of 4.1 MLE of Bi, flux of 0.16 $MLEmin^{-1}$. The image displays the stepped, rectangular (100)-pseudocubic orientated Bi islands. The islands are composed of four, eight, or a larger number of multilayers. c) LEED pattern from the pseudomorphic monolayer with pseudocubic islands. Coverage 4.1 ML, flux 0.32 $MLmin^{-1}$.

spaced. The ring represents 5 different orientations of the 3–fold islands, similar to the Ag/*i*–Al-Pd-Mn [144] and Xe/*d*–Al-Ni-Co [145] systems. Each island orientation is rotated 72° to the next alignment. This result evidences the influence of the fivefold substrate at this higher coverage.

The momentum transfer of this 30-spot ring is 1.646 ± 0.02 $Å^{-1}$, which is equal to a row separation in the Bi(111) structure of 3.82 ± 0.05 Å and therefore a lattice constant of 4.41 Å, a contraction of approximately 3 % from the bulk value of 4.54 Å [143] .

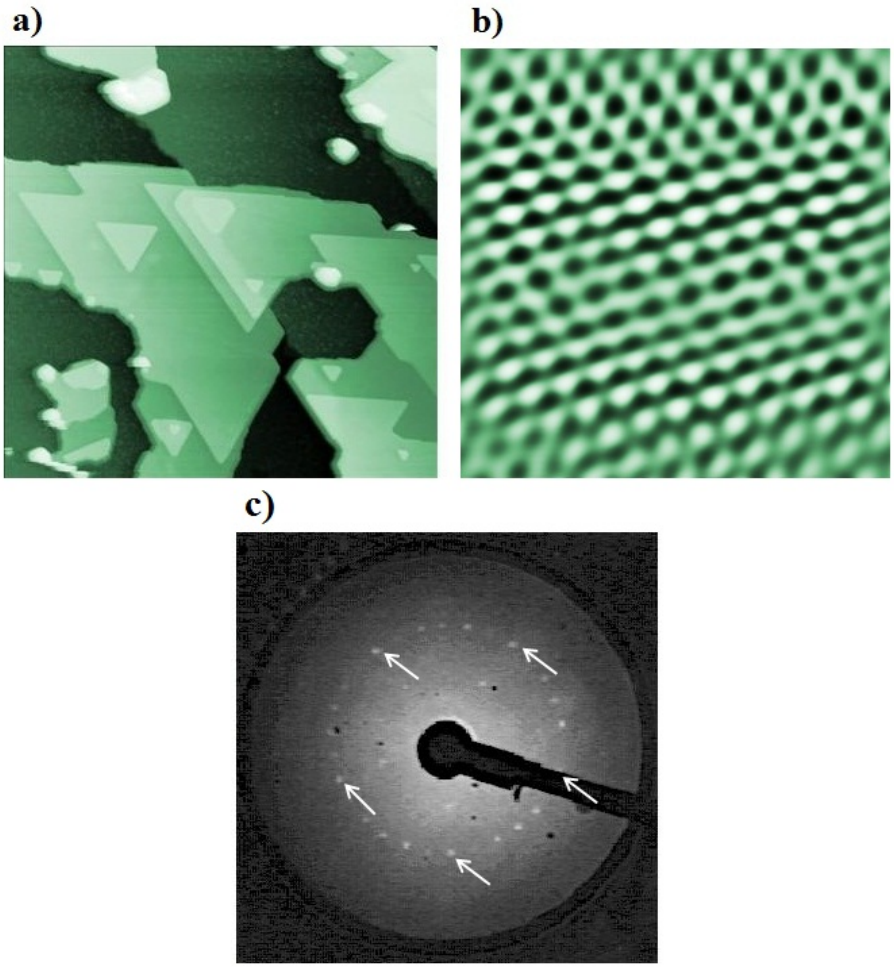

Figure 42: a) A 300 nm × 300 nm image showing hexagonal domain islands (V = 1 V, I = 0.2 nA). The image has a shadow filter applied for clarity. b) 5 nm × 5 nm dimension Fourier filtered image showing atomic resolution of an hexagonal island. c) LEED pattern from the monolayer with hexagonally oriented Bi islands; arrows indicate the substrate (21001) ring. The pattern was recorded at a beam energy of 76 eV. The flux of Bi atoms during deposition was 0.16 ML min^{-1} and the coverage is 4.1 ± 0.1 MLE.

The formation of the hexagonal phase is found to be flux dependent. For an equivalent coverage of 4.1 ± 0.1 MLE, the film (at equilibrium) deposited at a rate of 0.16 ML min^{-1} exhibits approximately 30 hexagonal domains per μm^2. A film of the same coverage deposited at 0.32 ML min^{-1} exhibits 930 ± 90 domains (prior to equilibrium) μm^2 distributed across 600 ± 30 islands. Some of these coalesce; after waiting for the system to reach equilibrium (14 h), a density of 700 ± 70 domains distributed across 320 ± 16 islands μm^2 was observed, corresponding to 2.2 domains

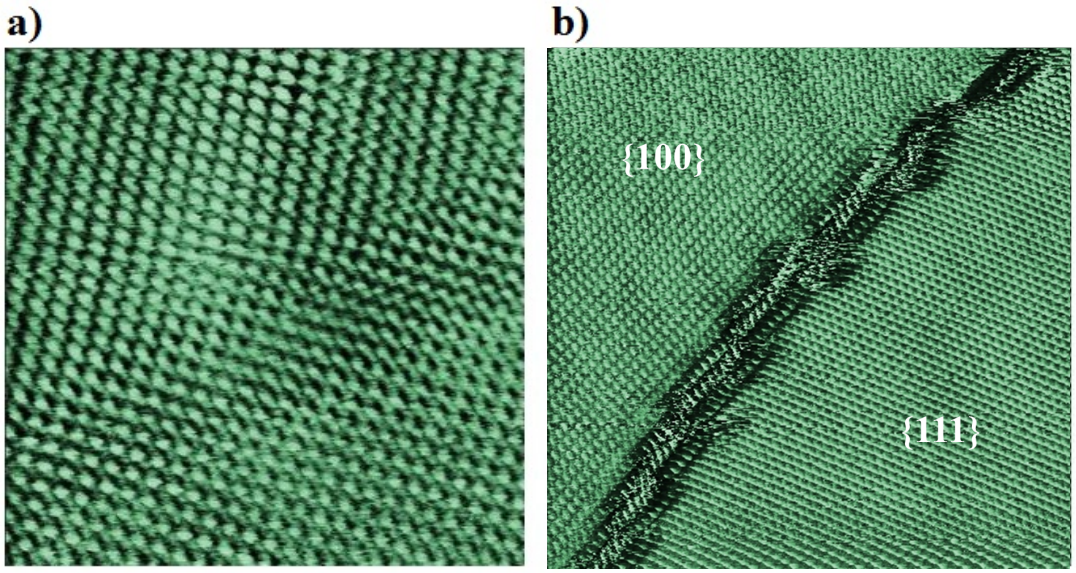

Figure 43: a) 15 nm × 15 nm images of a twinned pseudocubic island (Bi coverage of 4.1 ± 0.1 MLE, flux during deposition is 0.16 ML min^{-1}; (b) 20 nm × 20 nm STM image of a boundary between pseudocubic and hexagonal structures.

per island on average. Only two hexagonally ordered islands were observed in total across data spanning 4 μm^2 for the higher flux; the rest were pseudocubic.

The STM image shown in Figure 43 a) shows atomic resolution of the surface of one of these islands. It shows that there is a pseudo–square surface mesh, which leads us to confirm the earlier conclusion that Bi is oriented with a pseudocubic (100) (rhombohedral {012}) face parallel to the substrate surface.

There is a domain boundary on the twinned pseudocubic island in Figure 43 a). The boundary between the two domains is smooth and without defects. The angle between the domains is 100°, which indicates that at least one domain cannot be aligned with the substrate. Figure 43 b) shows a domain boundary between hexagonal and pseudocubic structures at this surface. In contrast to the domain boundary shown in Figure 43 a), this domain boundary shows many crystal defects. This coincidence of structures without subsequent transformation of the pseudocubic domain supports the idea that some pseudocubic islands are stable against transformation.

Scans of the Bi monolayer revealed a surface covered in round clusters of approximately the same size as in previous sub-monolayer studies [134]. Such a scan is displayed in Figure 44 a). The RMS (root mean squared) roughness of the monolayer was ∼0.3 Å, which is rougher than the flat clean surface, which has a roughness

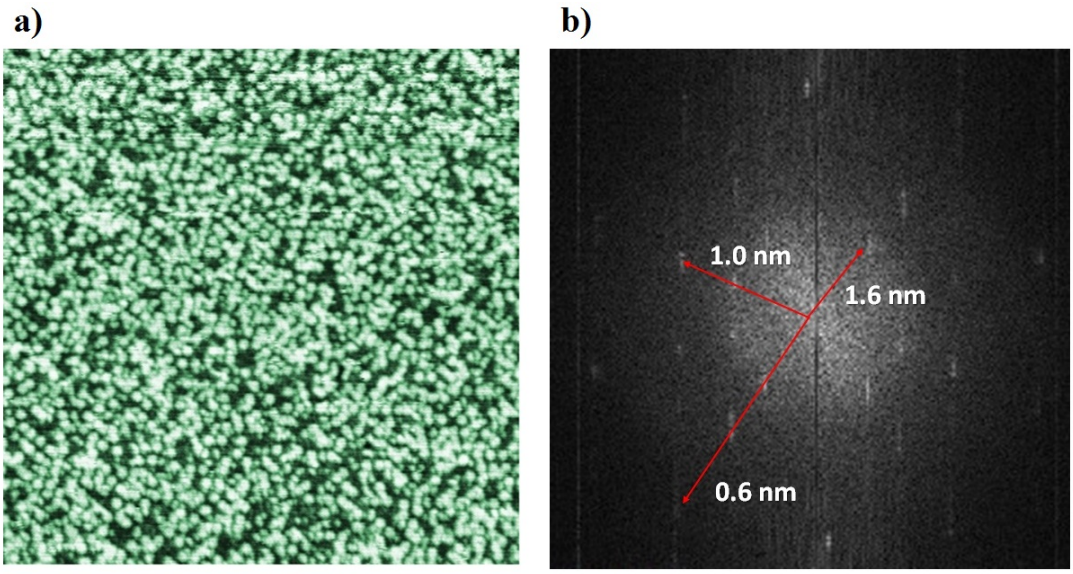

Figure 44: a) 80 nm × 80 nm V_{bias}= 1.2 V Resolution of pseudomorphic monolayer of Bi. Network of round clusters imaged. b) Square–root FFT of a). The real space distances of the 10–fold rings are marked in nm.

equal to 0.1 Å. The resolved images of the monolayer have clear, 10-fold FFTs - as displayed in Figure 44 b). The distances on the surface that these rings correspond to are the same as in images of the clean surface. This is further evidence for pseudomorphic growth of the first Bi layer. Subsequent rings moving radially out from the centre of the FT are related by a ratio of τ indicating positional ordering of the features in the STM image.

5.4 Discussion

The data has demonstrated that XPS can be used to determine the growth mode of an adsorbate on a complex intermetallic. The desorption curve, showing that ∼0.5 ML of Bi is more bound to the surface than the whole monolayer supports the initial nucleation regime [140]. It suggests that the Bi preferentially occupies all the sites where the pentagonal clusters form at the surface before forming the complete layer. For a deposition of 56 MLE the Bi overlayers would be oriented with the (0001)–hexagonal plane parallel to the surface. The clear plateaus in the desorption curve data suggests that the quasicrystalline monolayer is intact under these bulk-like Bi layers.

In a study of Bi growth on Si{111}–7 × 7 below a critical thickness of 6 ML, the Bi film has a pseudocubic (100)) surface, with pseudocubic surface unit cell lattice parameters of 4.75 and 4.54 Å and with step heights as observed by scanning tunnelling microscopy (STM) consistent with an even number of layers [142]. Above the experimentally determined critical thickness of 6ML, the entire film was found to undergo a transformation to a bulk–like structure, with an hexagonal {0001} plane parallel to the substrate surface. The *ab–initio* calculations performed by Nagao et al. led them to conclude that the film adopts a unique allotropic layer-paired structure similar to the 'black phosphorus puckered-layer phase, which reduces the number of dangling bonds at the surface. Cohesive energy calculations indicated that at thicknesses greater than 4 ML (for an infinite film), a bulk–like structure would become preferred over the [142] thin–film layer–paired structure.

It is notable that a transition from the {012}–rhombohedral oriented Bi to the (0001)–hexagonal oriented structure initially occurred at roughly the same deposition of 4 – 6 ML. As previously stated the current system exhibited many layered rhombohedral islands (up to 24 ML), whereas in contrast, the Bi islands of the same structure on Si{111}–7 × 7 strictly adhere to 2 and 4 layer pairing island growth. Perhaps a greater flux was used in the present experiment, which would promote 3–D growth, resulting in smaller islands with a larger number of layers.

Thin films of Bi grown on HOPG have been evidenced to grow in the {012}–rhombohedral structure up to a deposition of at least 5 ML via electron back scatter diffaction (EBSD) [146]. There was no complete wetting layer formed and instead growth proceeded by the formation of six–fold rotationally symmetric, star–shaped islands on top of which rectangular islands grew. The two island morphologies had strong orientational alignment with the substrate unlike in the present experiment. At 5 ML the film was found to be pseudocubic and at 12 ML it appeared that bulk–like hexagonally oriented Bi and pseudocubic Bi coexisted, with only bulk–like Bi islands persisting into the 100 ML regime. The Bi flux for those experiments was 0.53 ML min^{-1}.

A transition from pseudocubic to hexagonal islands was also observed as a function of coverage for Bi deposition above a monolayer on *d*–Al-Ni-Co with STM and LEED [135].

As island growth is observed for this system, it is clear that impinging Bi atoms have a degree of mobility on the quasicrystalline Bi wetting layer. Increasing the

flux decreases the mean free path of a Bi adatom and hence increases the frequency of cluster formation. Therefore increasing the flux promotes island nucleation rather than the growth of existing islands. As the islands in the pseudocubic phase are not aligned with the substrate, this increases the likelihood that islands which nucleate separately will subsequently coalesce with at least one domain boundary.

Once a critical single–domain lateral size or single–domain thickness (6 L) is reached, Bi islands transform from a pseudocubic layer–paired allotrope to the {111} orientation of the rhombohedral phase without layer–pairing generally referred to as hexagonal (0001). Islands that coalesce during the growth of the pseudocubic phase, or twinned islands, having one or more shared domain boundaries, stabilise these structures against subsequent transformation to the hexagonal orientation.

The overall coverage of Bi seems to be the main factor in the transformation for other systems [142, 146]. However, as the dependence on flux during deposition has not been investigated for the other systems, and in the system under discussion both hexagonal islands at low coverage (1.8 MLE) and pseudocubic islands at high coverage (4.1 MLE) are observed, the overall coverage can be discounted as the main governing factor for the transformation in the coverage regime of 1-5 MLE.

5.5 Summary

The results presented here elaborated on the atomic structure and gave a qualitative analysis of the stability of the overlayers. Atomically resolved STM shows {012}–rhombohedral oriented Bi islands for a lower coverage of 4.1 monolayers. These islands proceed to transform to (0001)–hexagonal islands with further deposition. It is demonstrated that at a higher flux the density of rhombohedral islands increases and the transformation to a hexagonal orientation is inhibited. LEED acquired from the hexagonal structure islands evidences their rotational alignment along high symmetry directions of the substrate.

6 Pentacene adsorption on the fivefold surface of *i*–Al–Pd–Mn

6.1 Introduction

The interaction of weakly interacting, linear molecules, such as pentacene, with quasicrystal surfaces has not been previously studied. For an introduction to pentacene and previous pentacene thin film growth studies the reader is referred to Chapter 3.3. In this chapter STM is used to study the interaction and growth of pentacene on the high–symmetry surface of *i*–Al–Pd–Mn and on layers of Bi grown at this surface.

The epitaxial multilayer of Bi formed on *i*–Al–Pd–Mn was described in Section 5. This study aims to compare the reactivity of the molecule on the clean, chemically complex quasicrystal and on the pseudomorphic Bi monolayer. If the larger Bi atoms can reduce the chemical reactivity of the surface they may be able to promote a greater degree of epitaxial growth, although, the Bi monolayer is more rough compared to the clean surface which may inhibit diffusion of the molecules. The crystalline Bi nano–scale islands formed on the monolayer offer an opportunity to simultaneously observe the growth on quasicrystalline and crystalline surfaces under identical experiment conditions.

6.2 Experimental details

The UHV chamber used was equipped with an Omicron VT–STM and an Omicron LEED instrument. The base pressure during scanning was below 1.0×10^{-10} mbar. The surface of the sample was prepared as previously described in Section 4.6 and was kept at room temperature throughout the experiment.

The pentacene was evaporated from a pyrex glass tube with a filament coil wrapped around it. The evaporator was repeatedly degassed to the operating temperature of 393 ± 2 K, as measured by a K–type thermocouple attached next to the pyrex tube. A 10 second dose at 393 K gave a coverage of 0.17 ± 0.04 ML on the clean surface of Al–Pd–Mn. The coverage was determined by measuring the area of surface covered, using STM images in the sub-monolayer regime.

Bi was dosed in the STM chamber itself from a water–cooled, Omicron EFM-3 *e*-beam evaporator. The Bi was deposited at fluxes of either 0.07, 0.08 or 0.17 ML

min^{-1}. This low deposition rate was chosen to reduce the nucleation density of nano–crystalline islands and hence promote the growth of larger islands without domain boundaries. Larger islands with greater space in between are easier to scan, and lower the risk of losing tip stability. Once the Bi was deposited, the surface was left for several hours before pentacene was deposited so that stable {012}–rhombohedral islands were allowed to form.

6.3 Results

6.3.1 Pentacene growth on *i*–Al–Pd–Mn

Figure 45 a) shows a typical scan following the initial deposition of 0.17 ± 0.04 ML of pentacene. At this coverage the pentacene molecules appear as an oblong shape and the substrate features are imaged simultaneously. The size of the dark holes from the substrate corresponds to the 'dark star' features. The positions of the molecules are evenly distributed across the surface and no local clustering is observed. Edges of the molecules are blurred outwards, which is most likely due to a molecular electronic cloud imaging effect, rather than due to movement of the molecules, as it is present after allowing the molecules time to diffuse and also at higher coverages. In addition, the majority of the molecules showed no movement between scans of the surface over a time scale of ∼30 minutes in one area.

The adsorbed molecules exhibit increased tunnelling current at either end (for the range of bias voltages resolution was maintained at $\pm 1.8V$). This charge-density distribution has been observed in other studies [111]. A line profile parallel to the long axis of the molecule is displayed in Figure 45 b). The distance of 9 Å measured between the maxima in tip height is approximately equal to the spacing of the outer carbon rings in an isolated pentacene molecule. The average difference between the height of the outer and centre carbon rings measured at the surface was 0.3 Å. The enhanced tunnelling and dimensions lead us to conclude that the features are single molecules adsorbed intact with their long molecular axis parallel to the surface. For the range of tunnelling conditions used the heights of molecules above the substrate was in the range 0.8 – 2.0 Å supporting a flat adsorption geometry. Figure 45 c) displays a higher resolution image with the majority of individual pentacene molecules highlighted by orange rectangles. More details of distinct substrate features are resolved: 'dark stars' are highlighted with a yellow pentagon and 'white flowers' with red rings.

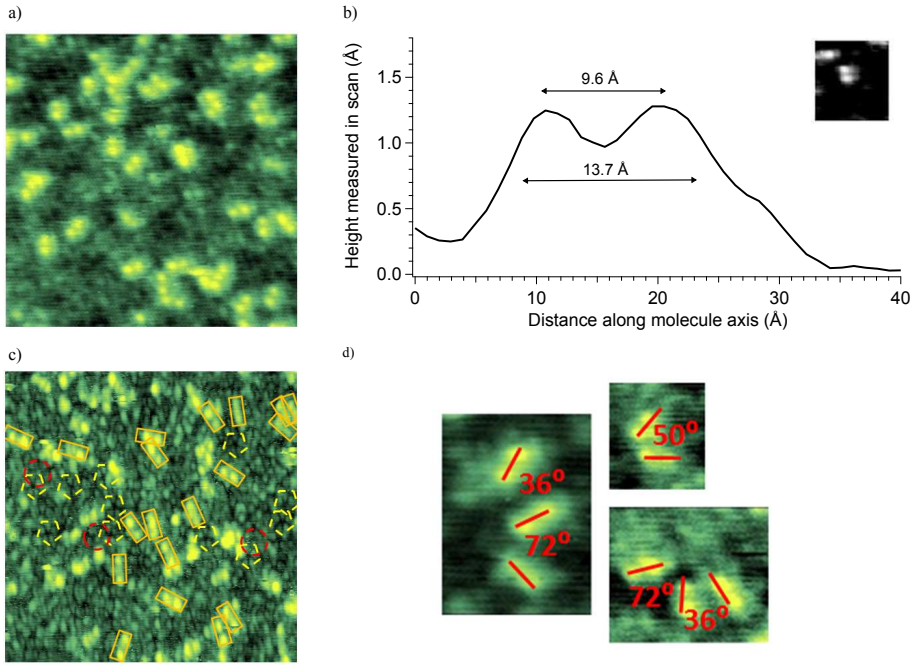

Figure 45: a) 23 nm × 23 nm STM image of 0.17 ± 0.04 ML of pentacene deposited on clean *i*–Al–Pd–Mn (V_{bias} 1.0 V I_T 0.083 nA) b) Profile along the molecular axis of an adsorbed pentacene molecule. The peak–to–peak and FWHM distances are marked. Inset: individual molecule that the profile was measured from. c) 25 nm × 25 nm 0.22 ML V_{bias} +1.4 V showing detailed substrate features. Individual molecules are highlighted with orange rectangles, 'dark star' features are marked with yellow pentagons and 'white flower' are marked with red rings. d) Sections of the surface – with the same coverage as in a),– showing the orientation of the adsorbed molecules with 5–fold symmetric angles relative to one another and demonstrating the presence of non–pentagonal angles. The error in the angle measurement is ±3°.

From analysis of the orientations of the long molecular axis for individual molecules there are several preferred orientations for the molecules at low coverage. Figure 45 d) shows distinct cases of several closely adsorbed molecules being orientated relative to one another with angles related to 5–fold symmetry. There are also some cases of non-pentagonal angles (one such case is shown).

The 10–fold rotational symmetry present in the fast Fourier transform (FFT) from the substrate disappears almost completely after an adsorbed coverage of 0.48 ± 0.08 ML dose of pentacene (see Figure 46 b)). This indicates that as more pentacene is deposited the molecules in the layer are randomly orientated and that there is no overall positional ordering of the molecules.

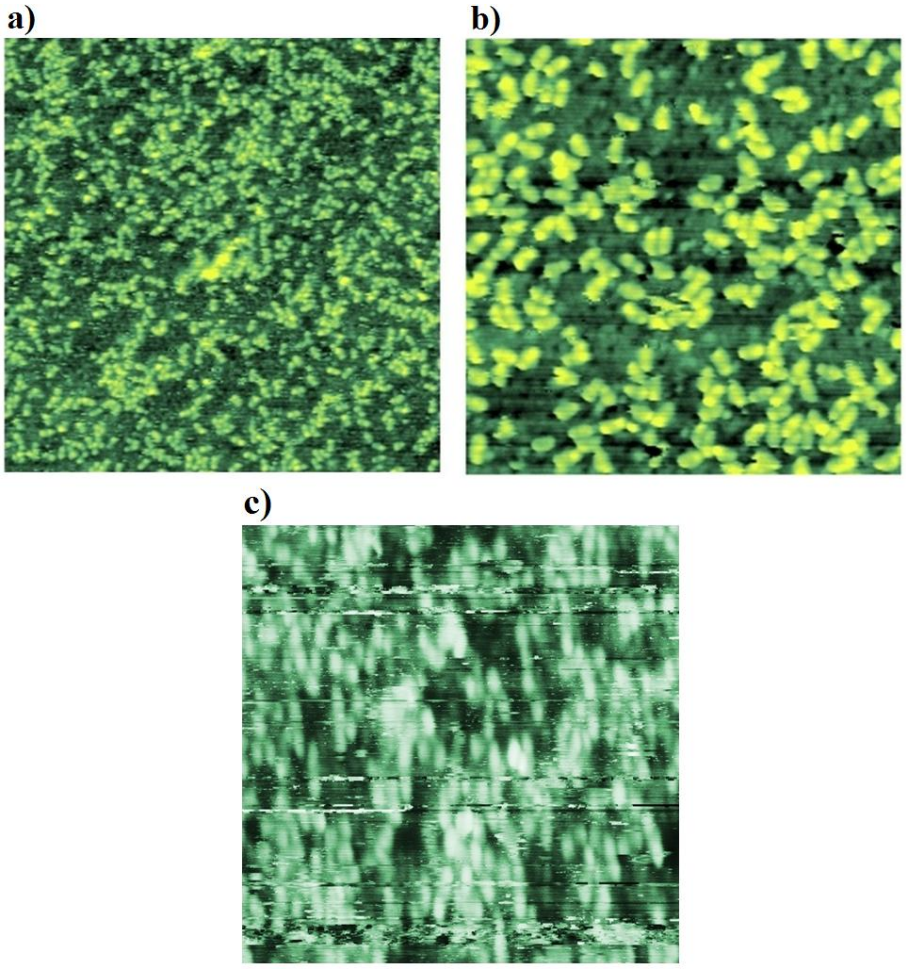

Figure 46: a) 55 nm × 55 nm STM image 0.42 ± 0.06 ML of pentacene b) 25 nm × 25 nm image of pentacene adsorbed on 5–fold Al–Pd–Mn at a coverage of 0.48 ± 0.08 ML c) 25 nm × 25 nm image of ∼1 ML of pentacene.

As the coverage nears a monolayer there is considerable streaking along the scan direction while imaging (see Figure 46c)). This effect is attributed to the tip picking up and moving loosely bound molecules across the surface. No LEED pattern is obtained from the 1 ML coverage. The sample with a flat monolayer of pentacene present was heated several times to 393K and 413K briefly and also for a duration of 10 minutes. The surface was checked with STM between each treatment and the annealing appeared to have no effect on the surface layer.

6.3.2 Pentacene growth on the quasicrystalline monolayer and nano-scale crystalline islands of Bi on *i*–Al–Pd–Mn

Pentacene on the quasicrystalline Bi monolayer

Figure 47 a) shows a typical image of 0.22 ML of pentacene adsorbed on the Bi monolayer. Individual molecules are resolved as a dumbbell shape similar to that found when the molecule is adsorbed on the clean surface. This shape appears more prominent compared to the clean surface; each end of the molecule appears larger in size compared to the central part of the molecule connecting them. Resolution of the Bi monolayer was achieved which yielded highly ordered FFTs although we were unable to discern individual Bi clusters once the pentacene was deposited.

The average peak–to–peak distance between the higher charge density ends of the molecule in the line profile of Figure 47 b) is slightly less than the spacing of the outer carbon rings in an isolated pentacene molecule. From the height of 1.8 Å for a single molecule we can conclude that the molecule cannot be adsorbed edge on to the surface and has its carbon rings positioned parallel to the surface. The average difference in height measured between the outer ring and centre carbon ring is 0.5 Å. This value is larger than that measured from molecules on the clean quasicrystal surface where the average was 0.3 Å.

A statistical analysis of the relative orientations of the long molecular axis on individual terraces showed that there are no preferred directions at this coverage. The resolution of the molecules and Bi layer quickly degraded at higher coverage.

Pentacene on nano-scale crystalline Bi islands

No evidence for pentacene adsorption on the rhombohedral–{012} islands was found until quite a high dose of pentacene. Figure 48 a) shows atomic resolution of such a Bi island after pentacene was dosed for 10 seconds. Atomic resolution of the (100)–pseudocubic Bi structure is clear and no evidence for adsorbed pentacene was found. Around 0.14 ML of pentacene was found adsorbed on the monolayer at this dose.

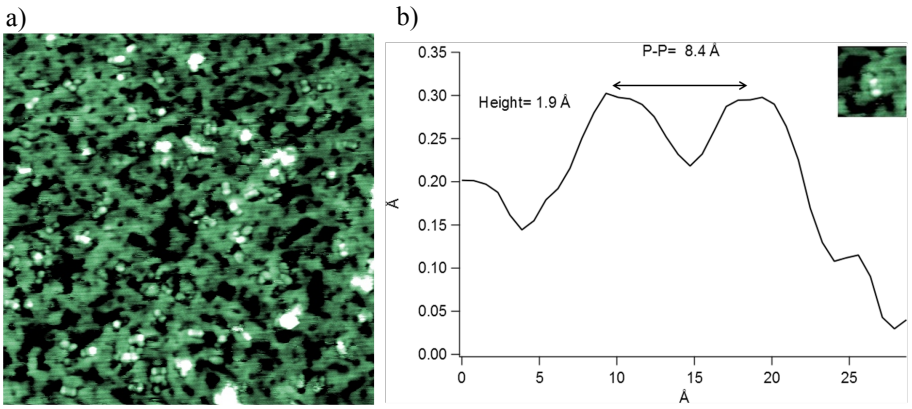

Figure 47: a) 40 nm × 40 nm STM image of 0.22 ML of pentacene adsorbed on a quasicrystalline Bi monolayer (shaded to enhance the molecules over the Bi layer) (V_{bias} -2.3 V I_T 0.108 nA). b) Line profile along an individual molecule the height and peak–to–peak (P–P) distances are marked.

Figure 48 b) c) show a square Bi island after dosing with pentacene for 100 seconds of pentacene deposited (0.83 ± 0.2 ML of pentacene on monolayer). Unresolved, close packed rows are imaged with a lateral peak-to-peak spacing of 16 Å. This is slightly larger than the length of an adsorbed pentacene molecule leading to the conclusion that these rows are composed of pentacene molecules with the molecules' long molecular axes aligned side-by-side. From the height of rows of ∼ 1 Å it can be deduced that pentacene lies in a flat geometry on Bi.

Two orientations of the rows are measured at an angle of 90° to one another. This angle is consistent with the rows being aligned along the Bi rows of the rhombohedral–{012} structure of the islands. The direction of the pentacene rows is distorted for some of the shorter rows around the central square step on the island in Figure 48 b). The direction of the rows is gradually changed by 20°, around the apex of this step, so that it does not have a cubic angle relative to the other rows observed. The rows around the central step are shown in Figure 48 d). This distortion suggests the underlying Bi rows also change direction here.

6.4 Discussion

Due to the large size of the molecules relative to the substrate features and the size of the surrounding electron cloud we are unable to determine the adsorption sites on the clean quasicrystal surface directly from STM. The complex surfaces of

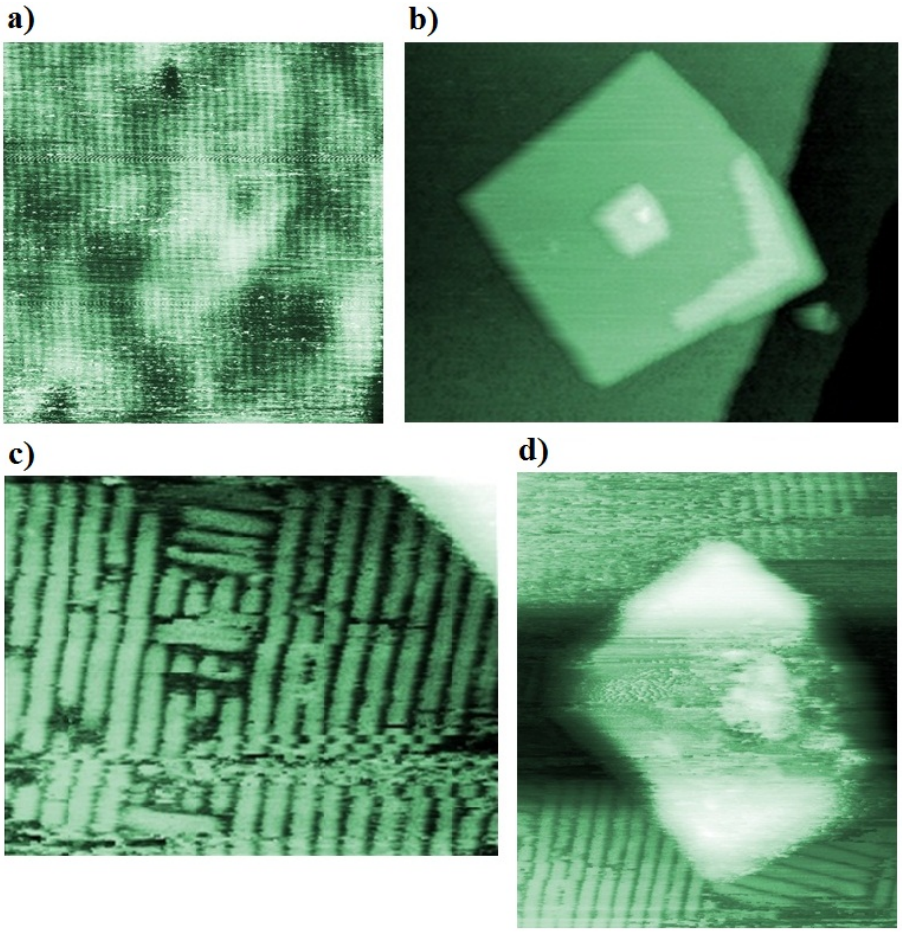

Figure 48: a) 20 nm × 20 nm Atomic resolution of a rhombohedral-{012} Bi island after 5.6 ML. A 20 second dose of pentacene was deposited (V_{bias}= 1.4 V I_T= 0.105 nA). b) Stepped, square rhombohedral-{012} Bi island after 6.3 ML of Bi is deposited. c) Unresolved periodic rows of pentacene adsorbed on the square Bi island of figure b)(V_{bias}= 2.8 V I_T 0.091 nA). Same Bi and pentacene coverage as in b). d) 35 × 42 nm Bi island in figure b) showing the rows around the top of the central step island.

quasicrystals have many different potential adsorption sites with varying interaction energies so one would not expect the influence of the substrate to propagate to higher coverages of pentacene. The lack of order of the molecules at coverages above around 0.2 ML suggests that there is no single preferred adsorption site and that the molecule adsorbs where it lands.

The increased charge density at the outer benzene rings highlighted in Figure 45 suggests that the highly aromatic central benzene ring is chemisorbed at the

surface. Experimental and theoretical studies of pentacene on Si(001)–2 × 1 have found a similar charge density distribution [147]. This is in contrast to an *ab–initio* study of pentacene on Al(100) [108] where there was a very small molecule–substrate interaction. The smaller peak–to–peak distance between the ends of the molecule than for an isolated molecule suggest some bending of the molecule. This would occur if the central ring was chemisorbed to the substrate atoms and hence closer to the surface.

A similar scenario occurred when pentacene was deposited on the quasicrystalline Bi monolayer. The adsorption geometry of the molecule relative to the substrate was the same, although the difference in height between the central and outer carbon rings was greater than on the clean surface by 0.2 Å. The greater variation in charge density across the molecule suggests that more charge has transferred to the Bi monolayer from the central benzene ring than in the clean surface case.

Unlike on the clean surface at low coverage, no preferred orientations at low coverage were measured for the molecules on the Bi layer. This may be due to the rougher Bi surface reducing the diffusion length of the molecules at the surface at room temperature.

On high quality Bi– rhombohedral–{111} ((0001)–hexagonal) films pentacene has been observed by STM to adsorb 'standing-up' in its bulk herring bone structure [148]. This corresponds to the ab-plane of the bulk pentacene crystal structure, which is the lowest energy crystal face. The inert, close-packed Bi–{111} surface is also the lowest energy plane (lower energy than (100)-Bi). The lack of interaction between the adsorbing molecules and the substrate encouraged bulk-like growth for the first layer. One would expect a similar growth mode on the triangular {111}–rhombohedral islands at the quasicrystal surface.

In the current study, the {012}–rhombohedral islands induce epitaxial growth of the molecules. The 'lying down' rows of pentacene that appear on the {012}–rhombohedral islands are suggested to form along the underlying Bi rows. Similar side-by-side rows have been observed with STM for the second layer of pentacene adsorbed on Au(111) [149]. The delay in forming these rows when a high coverage of molecules is present on the quasicrystalline Bi suggests a lower sticking coefficient for the flatter islands compared to the rougher Bi monolayer.

C_{60} molecules have shown bulk–like growth when physically deposited on some quasicrystalline surfaces. STM images of C_{60} adsorbed on a quascrystalline overlayer

of Pb on *d*–Al–Ni–Co have an hexagonal close packed (hcp) order [80]. Similar hcp islands of C_{60} were observed on all three allotropes of Bi present on *i*–Al–Pd–Mn [150]. The smaller intermolecular interaction between pentacene molecules compared to C_{60} may account for the disordered nature of the pentacene layers where no islands were seen to aggregate.

The domains of C_{60} on *i*–Al–Pd–Mn were not aligned along any high-symmetry direction on the quasicrystalline Bi [150] and are smaller than those observed in the Pb/*d*–Al–Ni–Co system [80]. The domains were larger on the crystalline Bi islands and aligned along high-symmetry directions of the rectangular and triangular islands. The molecules prefer to position along the edges of the islands - where there is increased coordination at the step, than on the top of the islands. The difference in growth modes for the crystalline and quasicrystalline surfaces was attributed to different diffusion lengths of the molecule on the rough layer compared to the less modulated islands.

6.5 Summary

STM has shown that the initial pentacene layer grows in a disordered fashion on *i*–Al–Pd–Mn and the quasicrystalline adlayer of Bi formed on this surface. The results suggest that pentacene is chemisorbed through its central benzene rings. The strong reaction of the molecule with the substrate leads to a disordered film. On the clean surface, a proportion of the anisotropic molecules adopt some pentagonal directions from the substrate. Similar behaviour was observed for pentacene adsorption on the pseudomorphic Bi layer. For pentacene adsorption on the rhombohedral Bi islands at high coverage, periodic rows are formed. Similar to previous cases for C_{60} adsorption on these features, the difference in growth between pentacene on the quasicrystalline Bi layer and on the Bi islands is attributed to the molecules having a smaller diffusion length on the quasicrystalline Bi layer compared to the islands.

7 Pentacene adsorption on the uniaxially aperiodic Cu multilayer formed on *i*–Al–Pd–Mn

7.1 Introduction

As previously described in Section 3.2, an aperiodic, surface row structure of crystalline Cu domains forms on *i*–Al–Pd–Mn. This structure was solved by LEED (IV), it was found to be a vicinal surface of a body-centred tetragonal structure [75]. Research into systems involving thin films of Cu are of importance to the semiconductor industry as Cu is currently used as the interlayer conductor in most devices.

In this chapter the results of the experimental investigation with scanning tunnelling microscopy (STM) and low-energy electron diffraction (LEED) of the growth of pentacene on the one-dimensionally aperiodic Cu multilayer pre-deposited on the *i*–Al–Pd–Mn substrate are presented. The experimental results for individual adsorption sites and molecular orientations are further elucidated by comparison to DFT calculations of the adsorption of a single acene at the surface.

7.2 Experimental details

The sample was prepared after insertion into UHV using the procedure described in Section 4.6. The Cu evaporator consisted of a W filament with a formed Cu wire on it. The formation of the required Cu multilayer structure was monitored with STM. Vapour deposition of the pentacene and Cu was performed in an interconnected UHV chamber which could be sealed off from the experimental measurement chamber by a manual valve.

A variable temperature Omicron VT–STM equipped with a chemically etched tungsten tip was used to scan the surface in constant current mode. Base pressure during scanning was 1.2×10^{-10} mbar. The sample was maintained at room temperature throughout the experiment.

7.3 DFT calculation details

Density functional theory (DFT) calculations of acene adsorption on the aperiodic, vicinal Cu surface were carried out by a collaborator: M. Lahti from the Lapeenranta University of Technology, Finland. Recounting examples of the electronic interaction

between a polycyclic molecule and a smooth surface, it has been found that the interaction is similar to that of several benzene molecules with the surface [151,152]. Therefore it is possible to find the trends in pentacene adsorption by studying the adsorption of smaller acenes. Naphtalene and anthracene - the acenes with 2 and 3 aromatic C rings - were used in the present calculations. For the current vicinal surface under study there are many more possible adsorption sites compared to a flat (111) surface and a large distortion of the surface is possible due to the presence of steps.

The Vienna ab-initio simulation package (VASP) [153,154] including the projector augmented wave (PAW) [155] potentials was implemented for calculations. The surface slab was modelled with 5 layers of Cu atoms. The total amount of Cu atoms in the supercell was in the case of naphtalene 115, and in the case of anthracene it was 138. A region of approximately 22 Å of vacuum was inserted in the z-direction to prevent interactions occurring between mirror images. The bottommost layer of the surface slab was fixed during the geometric relaxation.

The adsorption energy (Ads. energ.) of a molecule at a certain surface position is defined as the difference between the energy of the relaxed system and the original starting energy of the isolated surface and molecule. The quoted binding energies are calculated as the adsorption energy minus the surface and molecule distortion energy (termed Sur. Dist. Energ. and Mol Dist. Energ. respectively in the results tables).

7.4 Results

7.4.1 Experiment results

Figure 49 a) shows the sub–monolayer coverage after a 10 second deposit of pentacene on 4.40 ± 0.12 ML coverage of Cu. There are 5 equivalent orientations of the Cu domains confirmed by the FFT of images showing many domains. The Cu domains have an average length of 92 Å with a spread of one standard deviation equal to σ= 32 Å. Linear strain defects in the film are present along some domains [156]. These features are measured to have a height of 1.2 Å above the film.

Pentacene is imaged as an oblong shape of height 1.0 ± 0.1 Å. This height supports an adsorption model with the plane of the molecule flat on the surface,

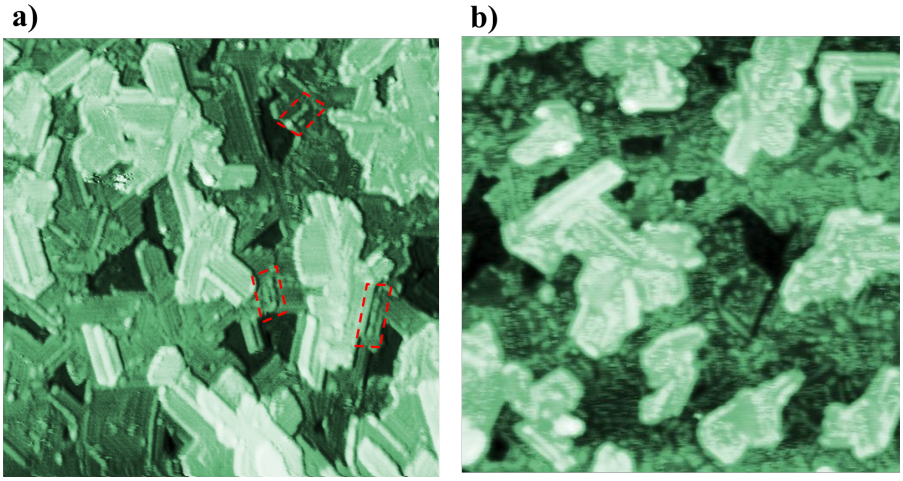

Figure 49: a) 1100 Å × 1100 Å 0.05 ± 0.02 ML of pentacene on 4.40 ± 0.12 ML of Cu on *i*–Al-Pd-Mn (V_{bias} 1.0 V I_T 0.105 nA) b) 1000 × 1000 Å 0.25 ML of pentacene. V_{bias}= 1.2 V Disordered, non-equilibrium structure of pentacene.

positioned with the long molecular axis parallel to the substrate. Several areas have been outlined in red in Figure 49 a) where the 2 or 3 molecules have aligned parallel, end–to–end and in one case also side–by–side. For subsequent depositions pentacene appears randomly distributed with a large amount of streaking on individual domains, as shown in Figure 49 b). The small streaks imaged suggest that the pentacene molecules are quite mobile and loosely bound on the domains.

After the system was left for several hours with a total deposit of ∼0.48 ML (60 second dose at 393 K), individual molecules were resolved again and the order of the film was found to have increased, see Figure 50 a). It can be concluded from the images that the pentacene molecules diffuse for several hours over the surface to form an ordered film. The molecules image more uniformly across the surface and a high majority are ordered parallel to the rows on each domain. The molecules generally adsorb end-to-end along the Cu rows rather than side–by–side across. Many of the longer rows of molecules form around the linear strain defects in the Cu film mentioned previously. As slightly more pentacene is deposited a closer packing of the molecules and longer end–to–end rows are clearly evident. The ends of each row line up with the domain edge and hence the molecules are not necessarily seen to align side–by–side across the rows. The longest rows are still observed next to the high, linear strain defects that protrude from the domains. The average distance between the rows is 12.8 Å but with a variation of σ= 3.9 Å. No periodic or aperiodic

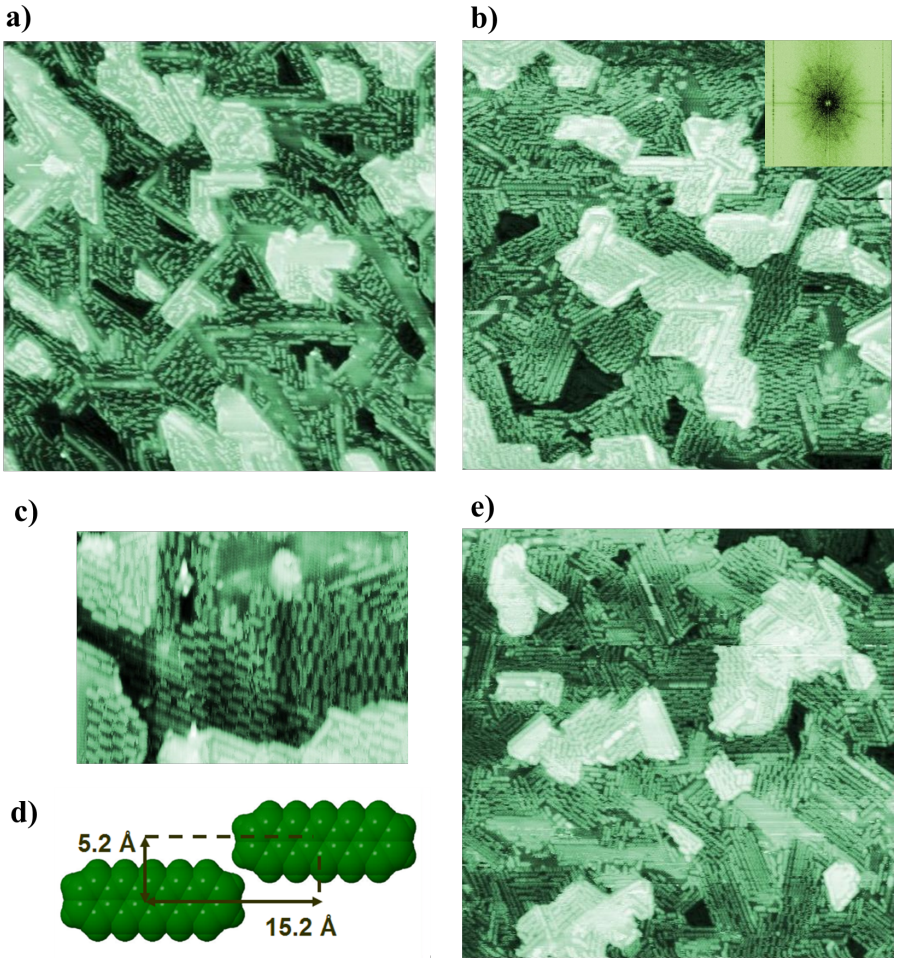

Figure 50: a) 1000 Å × 1000 Å 0.48 ML of pentacene after being left for several hours to diffuse (V_{bias} -1.0 V I_T 0.112 nA) b) 800 Å × 800 Å 0.59 ML of pentacene. The periodic superstructure of pentacene is evident (V_{bias} -1.2 V I_T 0.108 nA) Inset: FFT of image displaying 10–fold rotational symmetry of equally spaced streaks. This indicates that the pentacene is aligned along the 5 directions of the underlying domains. c) 310 Å × 210 Å close up image of several domains of the periodic structure. d) Model of the surface unit cell for the periodic structure. The dimensions are extracted from the measurements of the surface structure and the FFT of the domains. e) 800 Å × 800 Å V_{bias}= -1 V 0.7 ML of pentacene. Large scale image showing the periodic structure starting to fill in at a higher coverage.)

sequence of these spacings was extracted.

With a greater surface density of molecules (0.58 ML), a more ordered, periodically spaced structure evolves (see Figure 50 b)). Here a constant sized gap has formed after each molecule along the rows and the position of the gap alternates

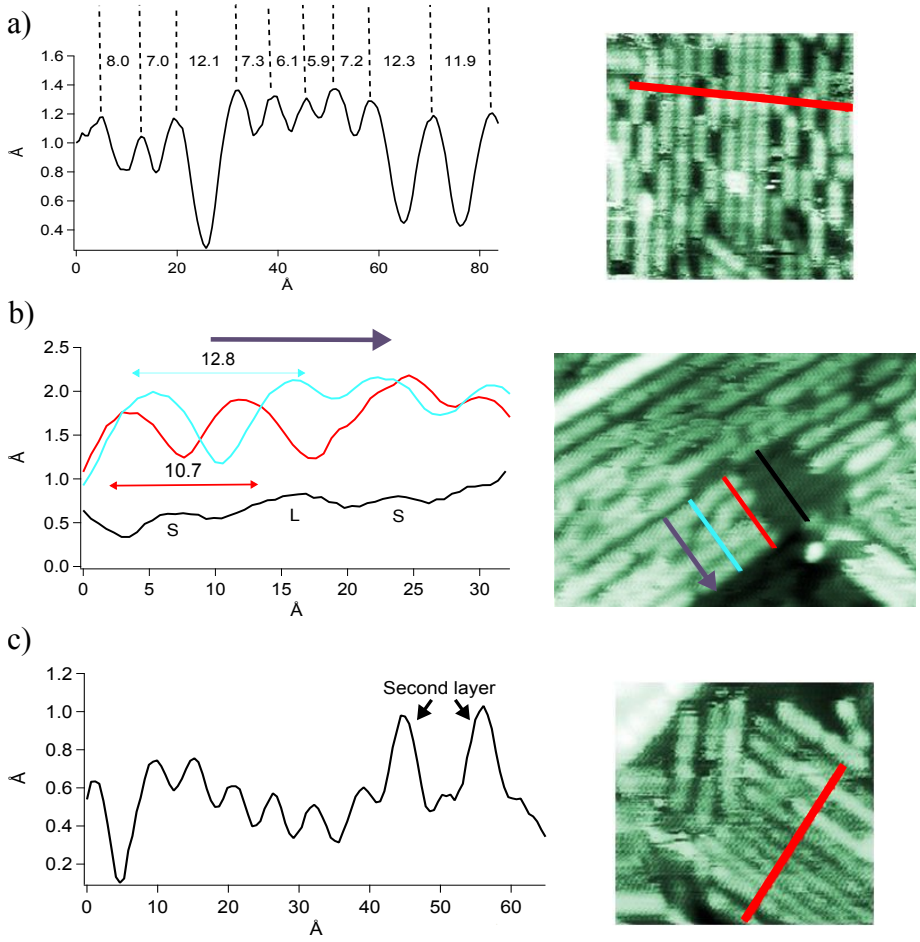

Figure 51: a) 100 Å × 100 Å 0.7 ML of pentacene showing the spacing of the rows as the periodic surface structure starts to fill in. b) 150 Å × 100 Å 0.7 ML of pentacene. The relative positions of the molecules to the adjacent exposed Cu rows are compared. c) 60 Å × 70 Å ∼1.0 ML Row detail showing partial second layer rows.

across the rows. At a higher pentacene coverage again the alternate site structure dominates the layer structure, although the end–to–end chains of molecules persist around strain defects. The FFT of the image is shown as an inset of Figure 50 b), with the streaks displaying 10–fold rotational symmetry is evidence that the molecules are still aligned along the 5 directions of the underlying domains. Figure 50 c) shows a close up of several domains of this structure. The surface unit cell measured from the FFT of a single domain gives dimensions of 15.2 Å × 5.2 Å. A model of the superstructure unit cell is shown Figure 50 d).

With further deposition the alternate site structure starts to fill in and the spac-

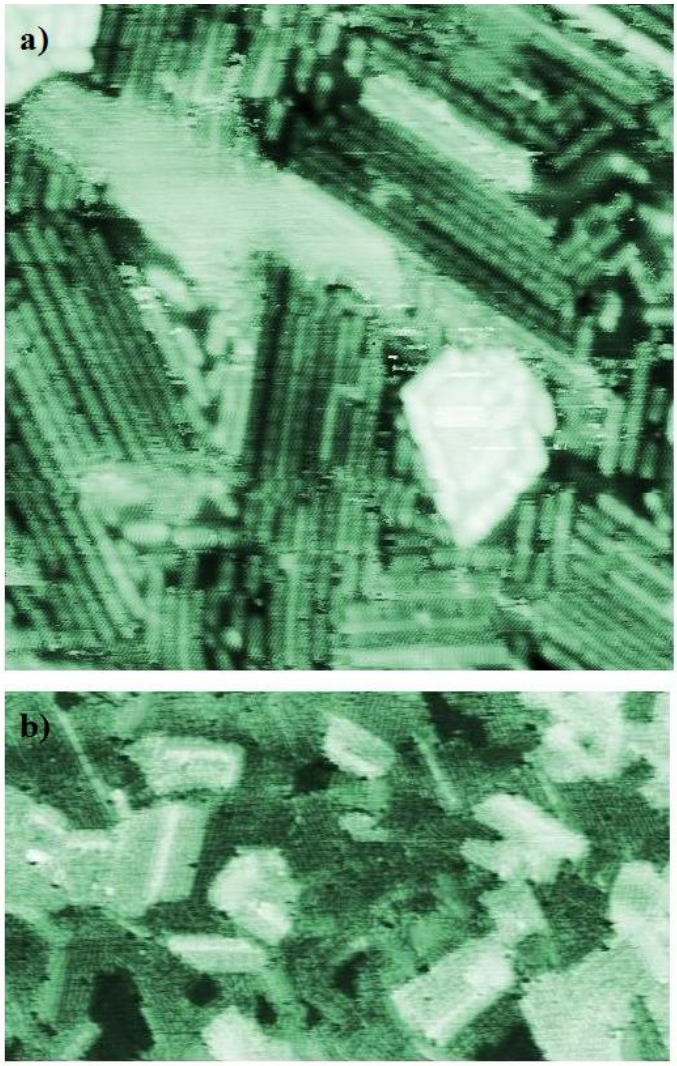

Figure 52: a) 300 Å × 300 Å (V_{bias} 1.1 V I_T 0.108 nA) ∼1.0 ML showing the densely packed pentacene rows on the Cu b) 1000 Å × 560 Å (V_{bias} -1.5 V I_T 0.084 nA) ∼1.3 ML showing a multilayer of pentacene. The densely packed rows that form along the Cu rows continue beyond the first layer.

ing across these denser rows becomes more irregular again (see Figure 50 e)). Figure 51 a) shows a line profile across a domain where both spacings are present demonstrating the variation in spacing of the filled in structure. The denser rows are nearly twice as closely packed with an average row spacing measured as 6.7 ± 1.2 Å.

A section of a domain where the pentacene has only partially adsorbed along the rows leaving some of the Cu rows bare is shown in Figure 51 b). The sequence of Cu rows is taken from a line profile perpendicular to the row direction and is identified

as SLS. From the green and red line profiles across the dense pentacene rows it is evident that that the molecules have adsorbed on both L and S rows. Comparing the green and red profiles across the molecule rows evidences different adsorption sites on the L rows. The spacing between the peaks of the molecules in two adjacent rows is marked. The difference of 2.1 Å in the row–to–row spacing indicates different possible adsorption sites laterally on the rows.

The spacing in the profile across the dense rows in Figure 51 c) shows that two molecules have been deposited directly on top of the first layer rows. Figure 52 a) shows a complete monolayer of pentacene formed with dense, long, end–to–end rows of molecules. There is a variation in the spacing across the rows and in the relative height of the rows. There is no distinct pattern of periodic or aperiodic spacing of the rows. This row structure persists for succeeding layers (see Figure 52 b)). No LEED pattern was recorded from the same multilayer coverage shown in Figure 52 b).

7.4.2 Theoretical results

Density functional theory (DFT) calculations carried out by collaborators in the Lapeenranta University of Technology were used to aid in understanding of the interaction of pentacene with the vicinal Cu surface and to determine the molecular adsorption site. To reduce calculation times, a naphthalene molecule (the acene with two benzene rings) was used. The molecule was placed at different potential adsorption sites along the rows, to match the experimentally observed pentacene behaviour. Table 3 shows the adsorption energies, binding energies and the minimum, maximum and average Cu–C distance corresponding to each adsorption site of naphthalene in Figure 53. The error on the calculated energies is ±0.2 eV. Taking this error into account one can see that there is not a large variation in the adsorption energies.

Sites 1 and 7 are calculated to be the preferred adsorption sites in terms of adsorption energy. Both sites have similar bonding and only differ in that site 1 is on an L step and site 7 is on an S step. In both sites the molecule leans against the 'upper step edge' and the carbon rings are centred almost above the hollow sites on the (100)–bct rows. The least preferred adsorption sites for naphthalene are 8 and 3. Site 8 has C atoms situated above the Cu atoms in the upper S step while the molecule at site 3 is on the outer edge of an L step. By comparing the green and

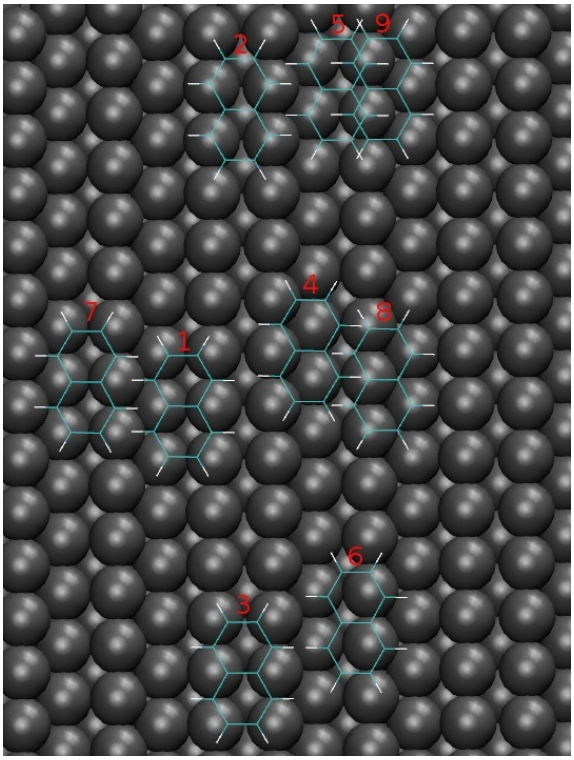

Figure 53: Model of the starting positions of relaxation of naphthalene molecules along the vicinal Cu rows. The adsorption energies and bond lengths for the different sites labelled are shown in Table 3

black profiles in Figure 51 b) it appears that a molecule is adsorbed at a position across the rows similar to site 3.

At the best adsorption sites there is heavy distortion of the surface. However, as we can see in Table 3, in most cases the distortion energy is negative meaning that the structural change of the surface makes it energetically more favorable. Overall there was more distortion when the molecule adsorbed nearer to the step. In all distortion cases the ledge row of the longer terrace moved to the new position and caused modification to the whole surface. Figure 54 a) and b) highlight where the surface distortion occurs for site 1 in Figure 53. Here the naphthalene molecule pulls up the Cu atoms row closest to it.

Excluding the distortion energy to determine the binding energy of the adsorbed molecules shows that site 3 is now the most preferred site. Comparing the adsorption sites 1 and 7 to adsorption site 3, it is apparent that they are very similar. Although site 1 is on the longer step terrace, site 7 is on the shorter step terrace, while

Place	Ads. Energ.	Surf. Dist. Energ.	Surface	Mol. Dist. Energ.	Binding Energy	Cu–C distance			C–C Distance	
						Shortest	Longest	On average	Shortest	Longest
1	-1.1	-0.51	Dist.	0.09	-0.68	2.25	3.69	2.82	1.38	1.44
2	-0.98	-0.48	Dist.	0.20	-0.7	2.24	3.04	2.61	1.40	1.44
3	-0.59	0.16	Slight Dist.	0.40	-1.15	2.22	2.44	2.34	1.41	1.45
4	-0.89	-0.43	Dist.	0.08	-0.54	2.35	3.21	2.79	1.38	1.44
5	-1.02	-0.54	Dist.	0.03	-0.51	2.25	3.54	2.98	1.38	1.44
6	-0.98	-0.53	Dist.	0.02	-0.42	-0.42	3.66	2.95	1.38	1.44
7	-1.09	-0.54	Dist.	0.12	-0.67	2.25	3.07	2.69	1.38	1.44
8	-0.22	0.16	Unchanged	0.02	-0.38	2.36	3.23	2.79	1.38	1.44
9	-1.01	-0.55	Dist.	0.02	-0.48	2.25	3.71	3.08	1.38	1.44

Table 3: Table of calculated adsorption energies and bond lengths for naphthalene adsorption on vicinal aperiodic Cu surface. The numbered places correspond to those labelled in Figure 53. Calculated energies are in in eV (error= $\pm$0.2 eV). Bond lengths are in Angstroms (Å). Dist. = Surface Distortion

adsorption site 3 is on the ledge of step. For site 3 the molecule binds to the row of surface atoms (see Figure 55 a)) which in the distorted case was moved. Also, in case 3 the molecule had enough space to keep the same horizontal angle as the terrace so the bonding of all C atoms of the molecule can be almost optimised(see Figure 55 b)). The binding energy per C atom is low for all sites, with a value of -0.12 eV for site 3.

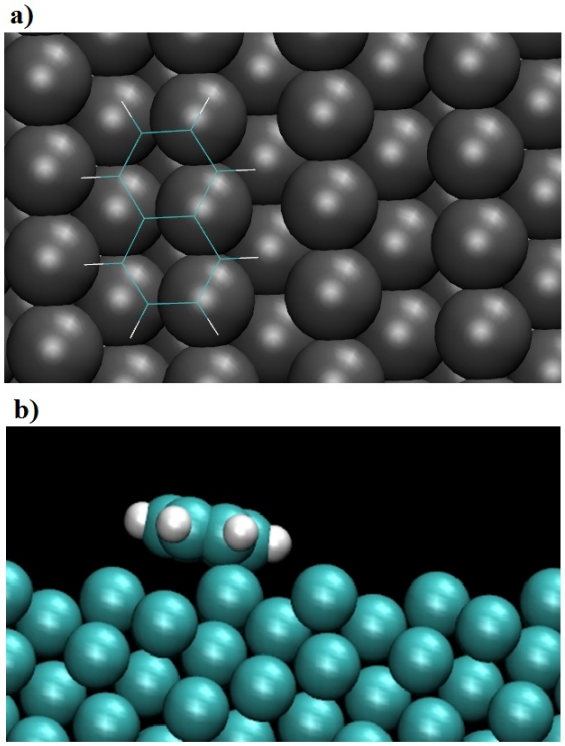

Figure 54: Model of an atom adsorbed at site 1 showing the distortion of the Cu row below the molecule a)Top view b) Side view.

Figure 56 shows the unrelaxed surface with the sites of the tested perpendicular adsorption sites. Overall most of the adsorption energies were much lower than in the cases of parallel adsorption sites -see Table 4. Adsorption sites 1, 2, 4 cause only light distortion to the surface. Only the adsorption site 3 was near the best cases of adsorption sites of the parallel molecule. However, the binding energies are weaker than in the case of parallel adsorption sites.

Next, the adsorption of anthracene on adsorption sites parallel to step edge near a corresponding favourable site for naphthalene were calculated. The adsorption site

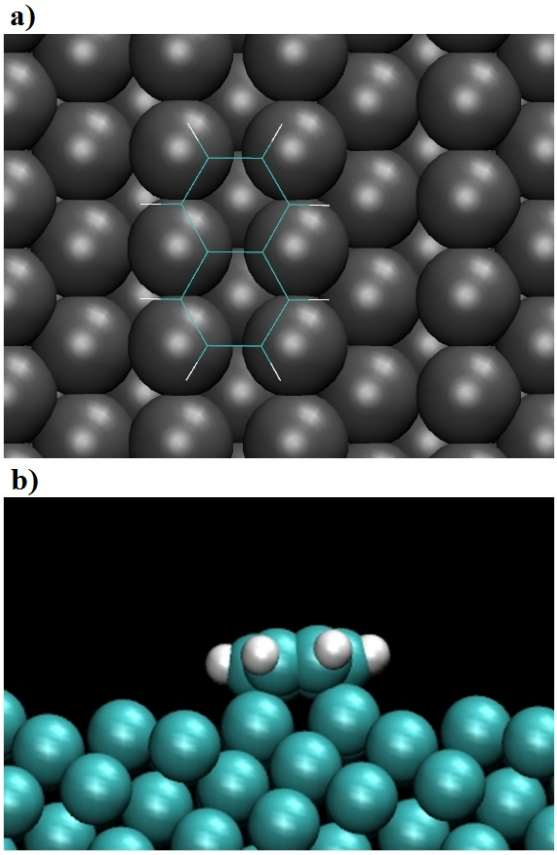

Figure 55: Model of an atom adsorbed at site 3 showing the distortion of the Cu row below the molecule a)Top view b) Side view.

Place	Ads. Energ.	Surf. Dist. Energ.	Surface	Mol. Dist. Energ.	Binding energy
1	-0.62	-0.04	Slight Dist.	0.16	-0.74
2	-0.18	0.02	Slight Dist.	0.01	-0.21
3	-1.00	-0.47	Dist.	0.08	-0.61
4	-0.43	0.11	Slight Dist.	0.08	-0.4

Table 4: Corresponding adsorption and binding energies for the final positions of naphthalene adsorbed perpendicular to the Cu rows in Figure 56.

3 from the naphthalene adsorption was chosen. The starting points of relaxation are displayed in Figure 57 and the adsorption energies are shown in Table 5. The slight differences in the starting point of adsorption made huge differences to the adsorption energy. For site 1 the distortion did not occur leading to an effect on adsorption energy. The overall binding energy per C atom are very similar for the

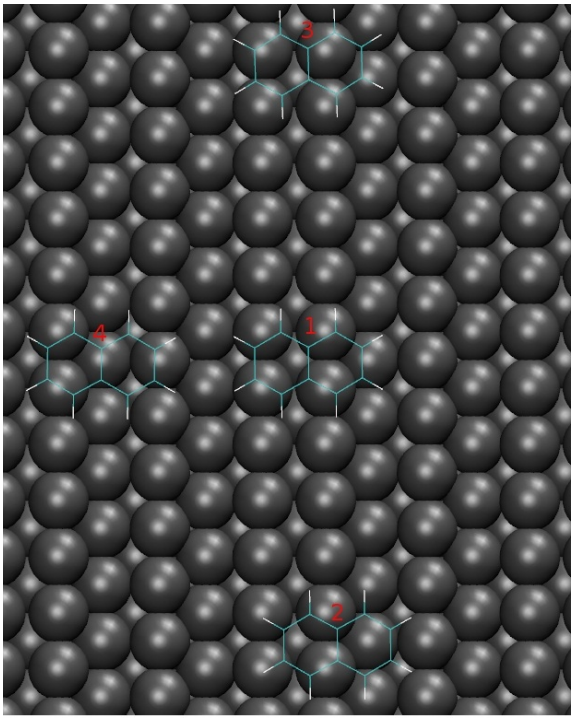

Figure 56: Model of the starting positions of relaxation of naphthalene molecules perpendicular to the vicinal Cu rows. The adsorption energies and binding energies for the different sites labelled are shown in Table 4

different molecules; calculated as -0.12 eV/atom in the case of anthracene and -0.11 eV/atom in the case of naphthalene.

Place	Adsorption energy	Surface
1	-0.16634	Slight Dist.
2	-1.3422	Dist.
3	-1.7035	Dist.

Table 5: Corresponding adsorption and binding energies for the final positions of anthracene parallel to the Cu rows in Figure 57.

7.5 Discussion

The current study was more successful in producing an ordered layer on the Cu surface which is aperiodic in 1–dimension, than on the clean surface which is aperiodic

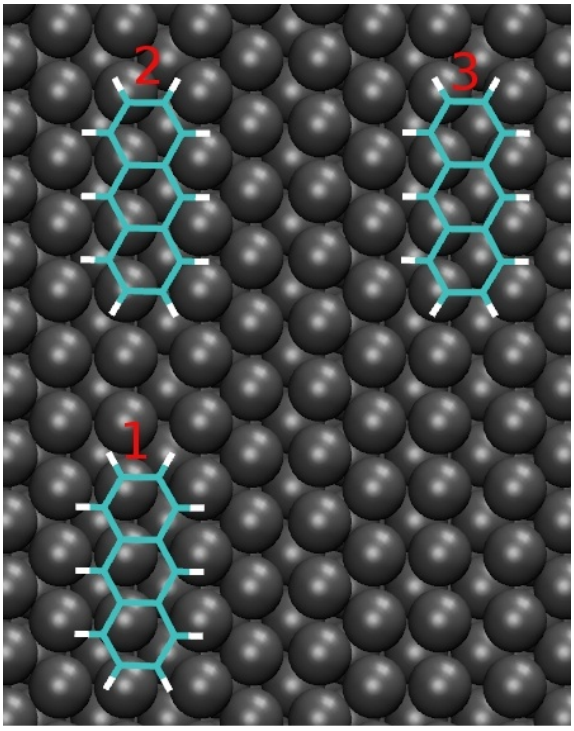

Figure 57: Model of the starting positions of relaxation of anthracene molecules parallel to the vicinal Cu rows. The adsorption energies for the different sites labelled are shown in Table 5.

in 2–dimensions. The aperiodic rows of Cu present a significant barrier to rotation of the molecules and reduce the number of different adsorption sites. This is supported by low coverage STM images of individual pentacene molecules aligning along the rows and further demonstrated by theoretical calculations of naphthalene adsorption energies parallel and perpendicular to the rows. The formation of a periodic structure instead of an aperiodic one (as in Figure 50 c)) at higher coverage implies that inter–molecular repulsion dominates as the overlayer becomes dense enough so that the molecules cannot avoid interaction with one another. This is supported by the DFT calculations which show low binding energies for the molecule at the surface and demonstrate that there is no significant preference for one site over another.

The DFT calculations demonstrated that there is a marked distortion of the rows for acene adsorption, especially in sites near the step edges. The initial results for anthracene adsorption were similar to that for naphthalene adsorption showing that the calculations can be scaled to larger acenes.

The current case is similar to pentacene layer growth on other vicinal Cu sur-

faces [157, 158] where the pentacene molecules were aligned end–to–end with their long molecular axis along the rows. For the (119) vicinal surface the molecules were adsorbed against the step edge. Previously an STM investigation of C_{60} molecules deposited on this vicinal Cu multilayer determined that they formed an incommensurate hexagonal structure at 0.5 – 0.8 ML [94].

The periodic, alternate site structure and the streaking imaged at lower coverage suggest a degree of molecular repulsion. The homogeneous character of the theoretical calculations for the adsorption of an individual acene along the vicinal Cu steps reinforces the conjecture that the molecule–molecule interaction is the larger interaction. For example, the evidence for adsorption of pentacene at different sites across the rows in Figure 51 b) suggests no overall preferred adsorption site while there is a high amount of neighbouring molecules adsorbed. Figure 52 a) showing the variation in the lateral periodicity of the filled in, dense row structure, may be explained by the influence of the edges of the domains and linear strain defects as site with greater surface free energy. The DFT calculations also showed a very weak binding for individual C atoms in the molecule at the surface.

7.6 Conclusions

It was observed that an incommensurate layer of pentacene grows when deposited on the aperiodic Cu rows formed on *i*–Al–Pd–Mn. The dense rows of pentacene form in the same direction as the vicinal Cu rows and adsorb on both L and S rows. DFT calculations show that the similar acene naphthalene prefers to adsorb along the rows with no significant preference for L or S rows. The formation of a periodic structure on an aperiodic substrate has been attributed to a larger molecule-molecule interaction relative to the molecule-substrate interaction at coverages of $\sim$0.5 ML or more.

8 Metal adsorption on the fivefold surface of *i*–Ag–In–Yb

8.1 Introduction

In this chapter two experiments involving metal growth on *i*–Ag–In–Yb are presented. First, the formation of a single, complete monolayer of the semi–metal Bi deposited on *i*–Ag–In–Yb is described. This complete layer is analysed as a prerequisite to using it as an interfacial layer for deposition of Cu and C_{60} in later experiments. The second experiment is an investigation of Cu growth at this surface and on an interfacial Bi monolayer.

For an introduction to the *i*–Ag–In–Yb quasicrystal surface the reader is referred to Section 2.8.2. Ag–In–Yb is a P–type icosahedral quasicrystal. It provides a high-symmetry surface composed of different elements and different structural components compared to *i*–Al–Pd–Mn.

8.2 Experimental details

The quasicrystal sample had a nominal composition of $Ag_{42}In_{42}Yb_{16}$. The five-fold surface was polished with different grades of diamond paste down to 1/4 μm. It was prepared in UHV by cycles of sputtering (2 keV Ar^+ ions for 30 minutes) and pro-longed annealing (2 hours at 690K) to produce a step and terrace morphology at the surface. Figure 58 d) displays a LEED pattern acquired from the clean surface. A clear 5–fold pattern confirms that long range quasicrystalline order is present. STM scans show that a large proportion of terraces exceed 0.1 μm in width.

The quasicrystalline order is also evident through the observation of a distinct 10–fold FFT from STM images of a resolved, flat terrace, as shown in Figure 58 c). Consistent with previous STM studies, different surface structural features at the surface are imaged depending on the whether positive or negative bias is applied between the tip and the sample [40]. With a sample bias (V_{bias}) < 0 V (electrons tunnelling from the sample to the tip) Ag/In protrusions with a size of 1.30 ($\pm$ 0.04) nm are imaged. The protrusions form pentagons of edge length 2.40 ($\pm$ 0.15) nm. At $V_{bias} > 0$ V (electrons tunnelling from the tip to the sample) Yb rings are imaged with a diameter of 1.8 ($\pm$ 0.05) nm.

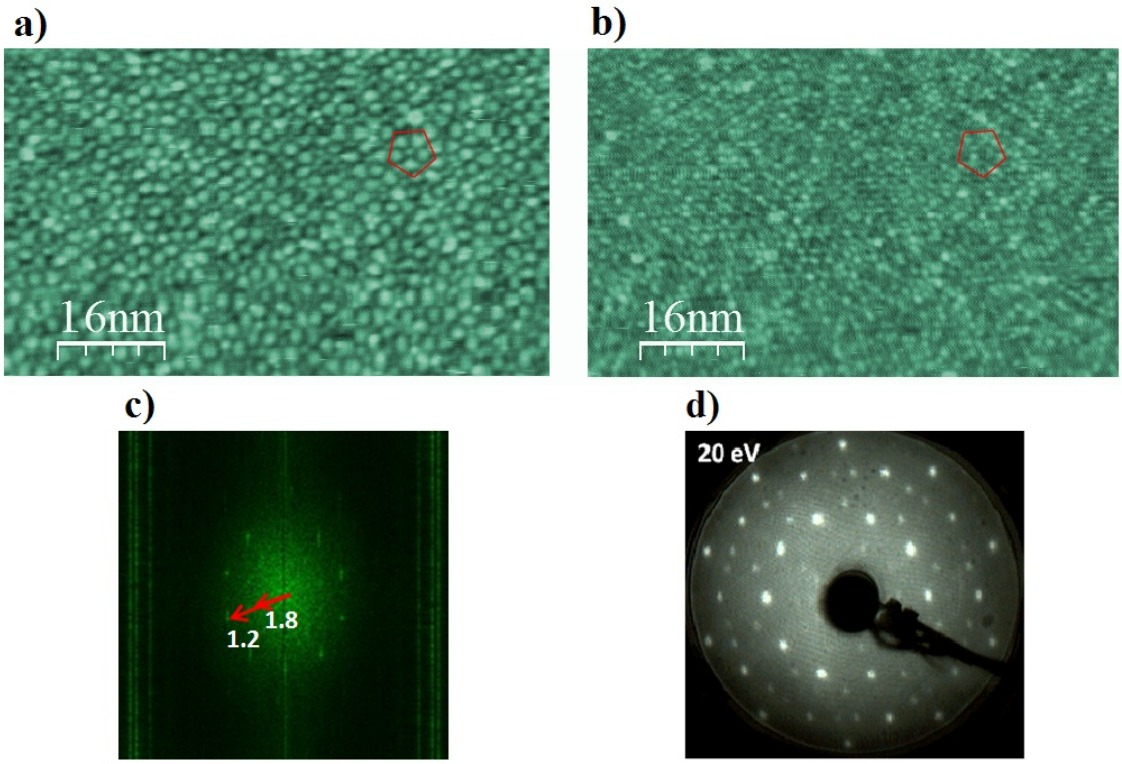

Figure 58: FFT filtered and merged STM scans of the clean five–fold surface of *i*–Ag–In–Yb a) 80 nm × 57 nm, -1.4 V b) Same position as in a). 80 nm × 57 nm, +1.4 V c) FFT from the an STM image of the clean surface at positive bias with the ring diameters converted to real distances. d) LEED pattern acquired from the clean surface of Ag–In–Yb at a beam energy of 20 eV.

Figure 58 a) and b) shows images where the high symmetry features have been filtered in the FFT and then merged with the original image to highlight the repeating structural features. The images are of the same area of the surface at different bias. The measured cluster–cluster distance at negative bias was slightly larger than previously published measurements at 2.7 ± 0.4 nm, although this value is still consistent within the calculated error. The FFT from a negative bias clean surface scan shows common high symmetry feature distances (distance of inner and outer rings from origin) of 2.0 nm and 1.2 nm. The FFT from the positive bias clean surface image shows common high symmetry features corresponding to distances (distance of inner and outer rings from origin) of 1.8 nm and 1.2 nm (see Figure 58 c)) which are close to the average high–symmetry rings/cluster sizes measured directly.

The Bi is evaporated from a Mo crucible mounted in a water-cooled, EFM-3 *e*–beam evaporator. The deposition rate was ∼0.09 MLmin^{-1}.

Cu was evaporated in–situ from a simple evaporator consisting of a Ta filament with a formed Cu wire wrapped around it. The deposition flux was calculated to be 0.004 ML/s on the clean quasicrystal surface. An Omicron VT–STM was used to acquire images of the surface while the sample was maintained at room-temperature. The base pressure during scanning was 1.4×10^{-10} mbar.

8.3 Bi growth on *i*–Ag–In–Yb

8.3.1 Results

The first layer of Bi deposited on the 5–fold surface of Ag–In–Yb in UHV conditions grows in a pseudomorphic fashion [159]. Once the layer is complete the sticking coefficient of Bi is greatly reduced for further layers from the incident vapour. STM images of the resulting monolayer contain a high density of repeating features with 5–fold and 10–fold symmetry. The most common feature at lower resolution of the layer are complete or almost completed rings of 10 atoms as shown in Figure 59 a). The FFT of large scale images of the monolayer have 10–fold symmetry similar to the clean substrate, as shown in Figure 59 b). The surface density of atoms found by applying a grain threshold to atomic resolution images was 1.5×10^{14}atoms cm^{-2}.

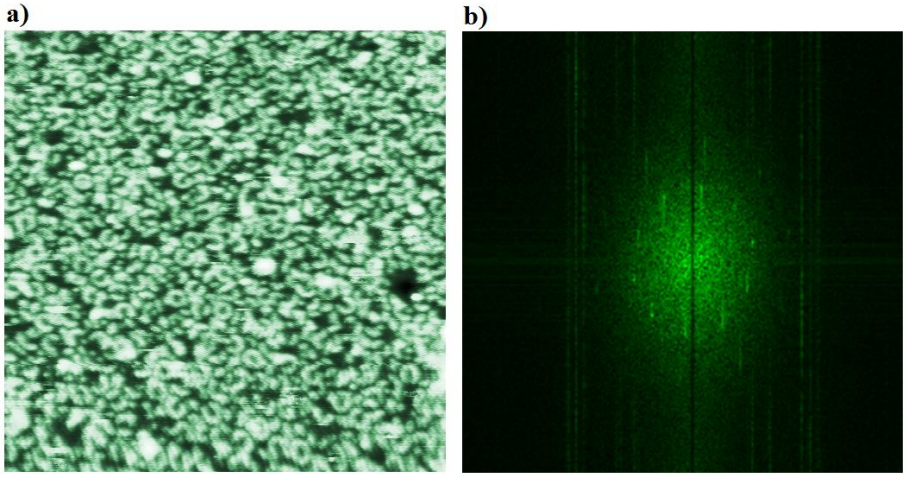

Figure 59: a) 50 nm × 50 nm STM image of 1 ML of Bi on the surface of *i*–Ag–In–Yb b) FFT of a) displaying distinct spots of forbidden 10–fold symmetry. This is indicative of a quasicrystalline monolayer.

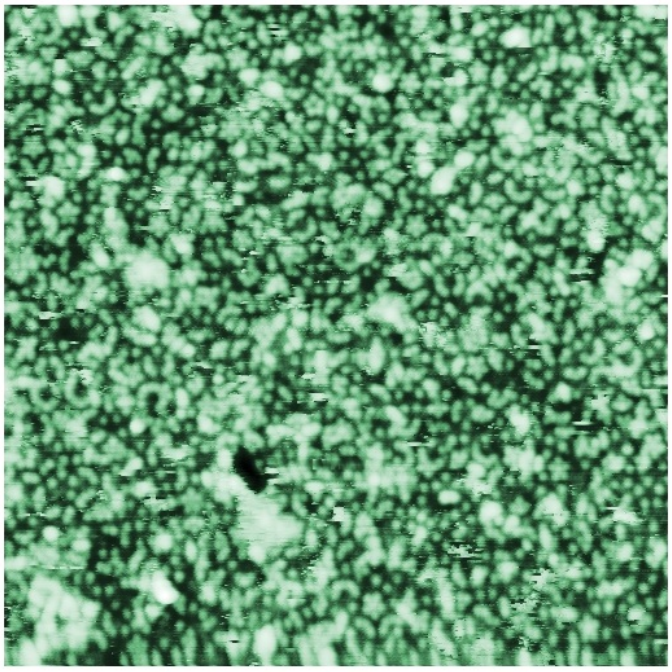

Figure 60: Atomic resolution STM scan of of Bi adsorbed *i*–Ag–In–Yb. 50 nm × 50 nm (V_{bias}= -1.6 V I_T= 0.105 nA) Atomic resolution of 0.90 ± 0.05 ML of Bi.

The image in Figure 60 shows atomic resolution of 0.90 ± 0.05 ML of Bi. Here a large proportion of the decagonal rings are only partially complete. The monolayer is composed of two different surface motifs, a pentagonal cluster (Figure 61 a)) and a larger decagonal ring (Figure 61 d)). The cluster, made of five Bi atoms in a pentagonal arrangement, has an edge length of 0.6 nm. There are two different orientations of this cluster at the surface, rotated by 36° relative to one another. The decagonal ring forms with a pentagon first, as shown in Figure 61 b), with an edge length of 1.0 nm. It is common for half of this ring to form before the rest of the ring is completed (Figure 61 c)). The complete, regular decagon has a diameter of 1.6 nm. The scaling between the size of these common features is $\sim\tau$.

8.3.2 Discussion and conclusions

STM has shown that the first monolayer of Bi on *i*–Ag–In–Yb grows in a pseudomorphic fashion. This growth is the same as that observed for Bi depostion at other high–symmetry quasicrystal surfaces [76, 160].

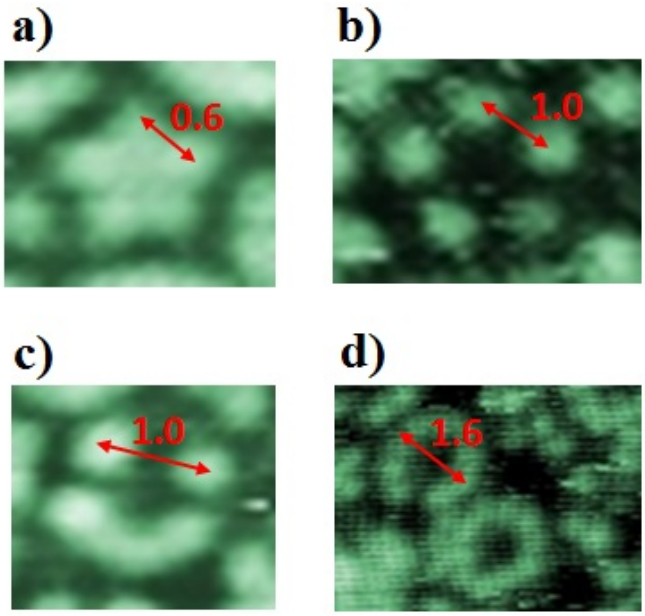

Figure 61: Atomic resolution STM scans of clusters of Bi adsorbed *i*–Ag–In–Yb. Distances marked are in nanometres (nm). a) Smaller pentagonal cluster b) Larger pentagonal cluster, which is a precursor to the decagonal ring formed at this surface c) Common 'half-filled' decagonal ring d) Complete and almost complete decagonal rings of Bi.

The system has some similarities with the growth of other heavy, p–block elements on this surface [83, 84]. Sb, Pb and Bi all have low surface free energies. The 1.0 nm edge length pentagon is approximately the same size as the pentagonal clusters of Pb and Sb that have been experimentally observed to form at this surface. This suggests the same adsorption site for the feature for all three adsorbates. In theoretical studies of Pb adsorption the preferred adsorption site (with the lowest potential energy) was calculated as a five–fold coordinated site between three In and two Yb atoms [161].

Overall the Bi layer has a higher surface density than the Sb and Pb layers. Sb and Pb did not show a further filling in of the 1.0 nm edge length cluster to form the decagonal rings of 1.6 nm. Also, the 0.6 nm pentagon was not as common for Sb adsorption and does not occur in the first Pb layer.

8.4 Cu growth on *i*-Ag–In–Yb and on Bi/*i*–Ag–In–Yb

8.4.1 Introduction

This section reports the experimental investigation with scanning tunnelling microscopy (STM), of the epitaxial growth of Cu on the fivefold surface of the *i*–Ag–In–Yb quasicrystal. We observed the growth from sub-monolayer to multilayer coverage. The growth of Cu on the Bi pseudomorphic monolayer on this substrate is also briefly studied for comparison. Bi forms a pseudomorphic overlayer which is less dense than the quasicrystal surface layer. The Bi overlayer may reduce the reactivity of Cu to certain chemical species at the surface. Bi has a low surface free energy relative to Cu and can act as a surfactant.

Pre–deposition of species with lower surface energy on a substrate has been shown to promote epitaxial, layer–by–layer growth in homoepitaxy and heteroepitaxy experiments. One role of a surface–active agent (or surfactant) is its ability to reduce surface free energy by 'floating' on the surface. The mechanism by which a surfactant discourages 3–D growth of an adsorbate is analysed in [162]. The effect of surfactant mediated growth was first shown in the formation of crystalline, epitaxial layers of germanium (Ge) on silicon (Si) using arsenic (As) as a surfactant [163].

Surfactant atoms are accommodated at high–coordination sites on the surface (i.e. step edges and kinks at islands/terraces) thus reducing the surface free energy of the substrate. Adsorbate atoms diffuse over the surface further as the most energetic sites are occupied with surfactant atoms. The adsorbed atoms can exchange positions with the surfactant atoms at the surface high adsorption energy sites and hence are incorporated into the film so that they continue the growth of islands laterally. Surfactant atoms situated at defects reverse the potential barrier at steps to suppress island growth; they reduce the Ehrlich–Schwoebel barrier [162]. This barrier is an important kinetic constant that inhibits inter-layer diffusion of adatoms due to reduced bonding coordination at surface step edges.

8.4.2 Results

Cu growth on *i*–Ag–In–Yb

After the first Cu deposition of 0.19 ML (Figure 62 a) and b)) the majority of the clusters of Cu atoms (highlighted in white) are one atom high, at a measured

height of 0.129 ± 0.013 nm. The average radius of the clusters is 1.22 ± 0.23 nm but many cases of individually adsorbed Cu atoms are present. With further deposition of Cu to a total coverage of 0.28 ML (Figure 62 c) and d)) the average height of the clusters increased slightly to 0.15 nm. The order in the FFT is less apparent now, a ring corresponding to a distance of 1.3 nm is the most prominent compared to the other 10–fold rings. It is clear that the bias dependency of the substrate structure imaged is still present after deposition of around 0.28 ML of Cu.

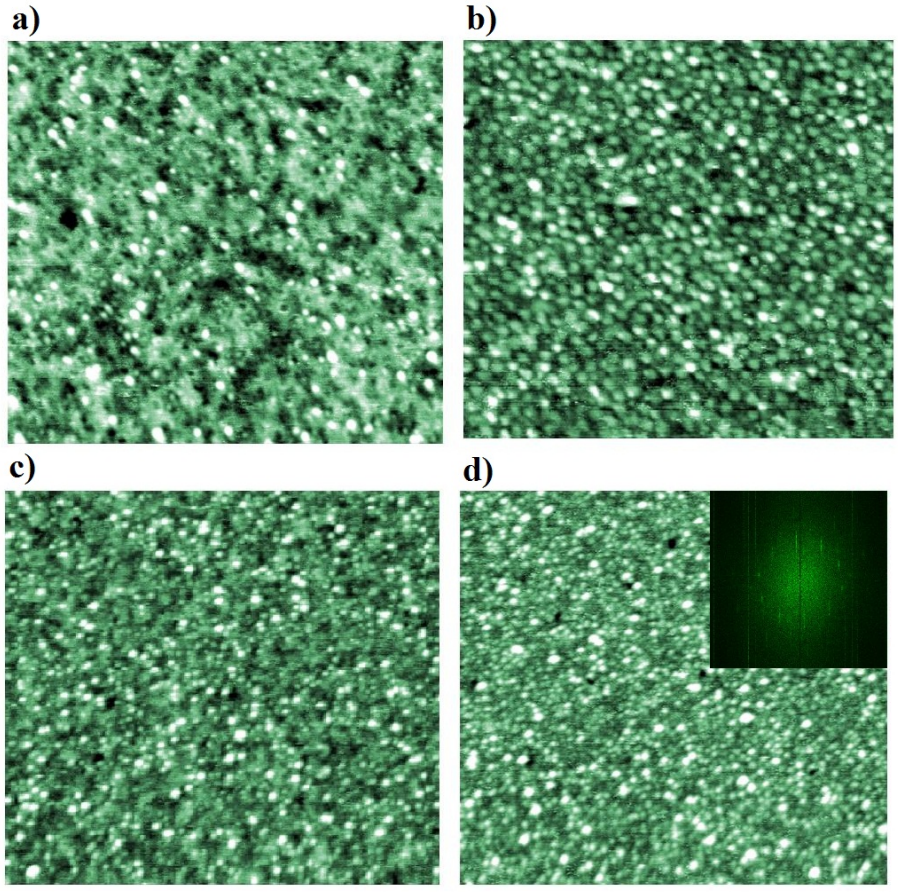

Figure 62: The initial Cu clusters (shown in white) imaged at the surface of *i*–Ag–In–Yb on the resolved substrate features. a) 75 × 66 nm 0.19 ± 0.06 ML +1.2 V Holes 1.7 +/- 0.1 nm b) 75 nm × 66 nm 0.19 ± 0.06 ML -1.1 V c) 120 × 106 nm 0.28 ± 0.08 ML of Cu. V_{bias}= +1.2 V d) 120 × 106 nm 0.28 ± 0.08 ML V_{bias}= -1.2 V Inset: FFT of a negative bias image of this coverage with the distance of the high symmetry rings marked in nm.

Figure 63 displays FFT filtered and merged images of scans with a low sub-monolayer amount of Cu deposited. At negative bias the Cu adsorbs mostly atop

the Ag/In protrusions. For positive bias the Cu is seen to adsorb inside and on the edges of the Yb rings. Individual cases of Cu adsorbed on the protrusions at negative bias are shown in Figure 64. In Figure 64 a) one can see the Cu growing on top of a curve of protrusions and on 4 of the 5 protrusions in a pentagon arrangement of the protrusions in Figure 64 b). Figure 64 c) shows Cu adsorbed on some of the protrusions that are arranged in a pentagon. Here one of the pentagons of protrusion features with an individual Cu atom adsorbed at its centre. This region of the surface is compared to a similar region in the isostructural model of i–CdYb in Figure 65 b). From comparing the group of surface clusters with the Cu adsorbed one can see that the Cu atom is adsorbed at a high symmetry coordination site. An atom at the centre of this feature is above a pentagon of Yb atoms and surrounded by five Ag/In pentagons.

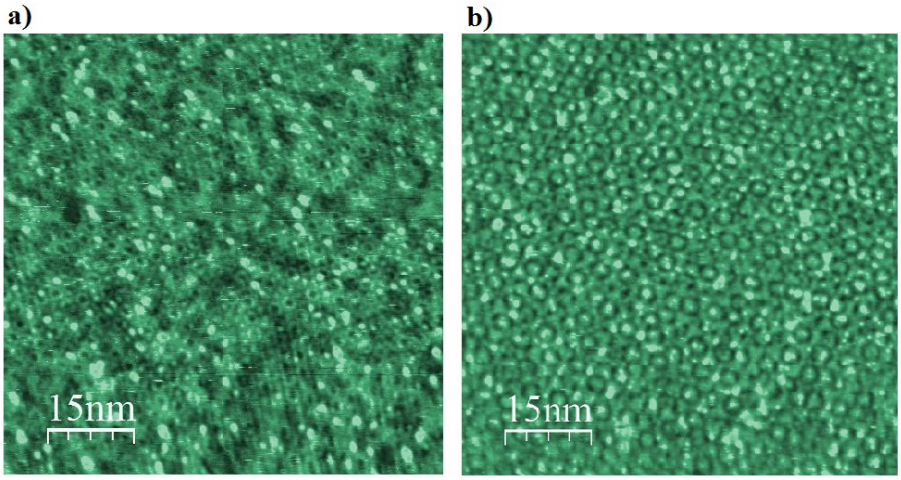

Figure 63: Images of ∼0.08 ML of Cu on the surface. High symmetry feature are filtered from the FFT and merged with the original image to highlight where the Cu is adsorbed relative to the repeating substrate feature. a) 75 × 75 nm V_{bias}= -1.2 V b) 75 × 75 nm V_{bias}= +1.2 V bias

At a calculated coverage of 0.51 ML a terrace with lower coverage was also found as displayed in Figure 66 a) and b). The coverage on this terrace is ∼0.05 ML. In the positive bias image of Figure 66 a) the hole diameter varies in the range 1.4 – 2.9 nm. There are many distinct cases of Cu atoms adsorbed on top of the Ag/In protrusions in Figure 66 b). Figure 66 c) shows a typical image from this total deposition corresponding to 0.51 ML, where there are no identifiable substrate features clearly imaged. Nonetheless, two distinct 10 spot rings were observed in the FFT of this image. The average Cu cluster diameter for this coverage has increased

to a measured value of 5.05 nm with a much larger spread σ= 1.31 nm. The average height has increased to 0.20 nm with σ= 0.06 nm.

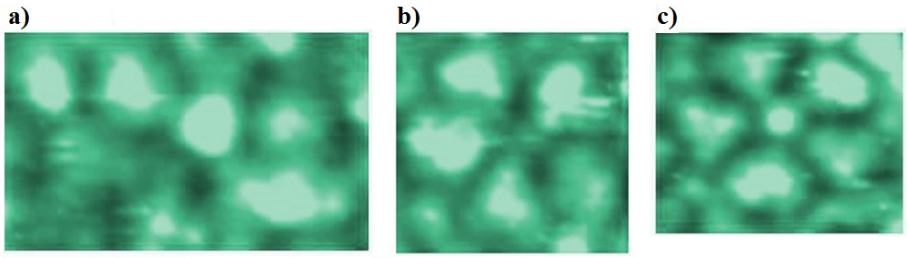

Figure 64: a), b) and c) Examples of Cu adsorbed on top of the round substrate protrusions. Negative bias images. Cu is highlighted in lighter green.

At a coverage of ∼0.92 ML the cluster size has visibly increased laterally and vertically (see Figure 36 d)), supporting a 3-D growth mode of Cu epitaxially grown on this surface. The average cluster diameter measured is 5.25 nm with a spread of ± 1.39 nm. The average height of the clusters has increased to 0.37 nm σ= 0.10 nm. Images where the substrate has been masked out still have 10–fold order. There are two rings of ordered spots in the FFT from images with a greater length scale than 100 nm.

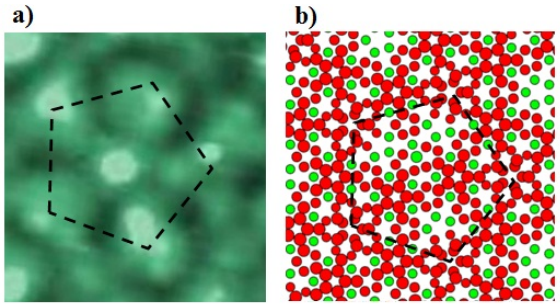

Figure 65: Left–hand side: Surface model of a termination of the *i*–Cd–Yb atomic structure showing a similar group of clusters as in the right–hand side of the image. Red: Cd or Ag/In Green: Yb Right–hand side: Negative bias image. Cu highlighted in lighter green. Cu is adsorbed on top of the round substrate protrusions. An individual Cu atom is adsorbed at the centre of the pentagon of round protrusions.

At a coverage of around 1.5 ML the average cluster size has increased to 5.31 nm with σ= 1.90 nm. The average cluster height has roughly doubled to 0.49 nm σ= 0.18 nm. The FFTs from various scale images show no apparent order.

Figure 67 a) and b) display the clustered surface at the higher coverages of around 2.5 ML and 4 ML respectively. The clusters appear larger both laterally and vertically. There is an increased range of cluster sizes; the heights of the clusters varies from 0.26 nm – 0.65 nm and the diameter from 2.6 nm – 5.3 nm. No order is observed in the FFTs of images at these coverages.

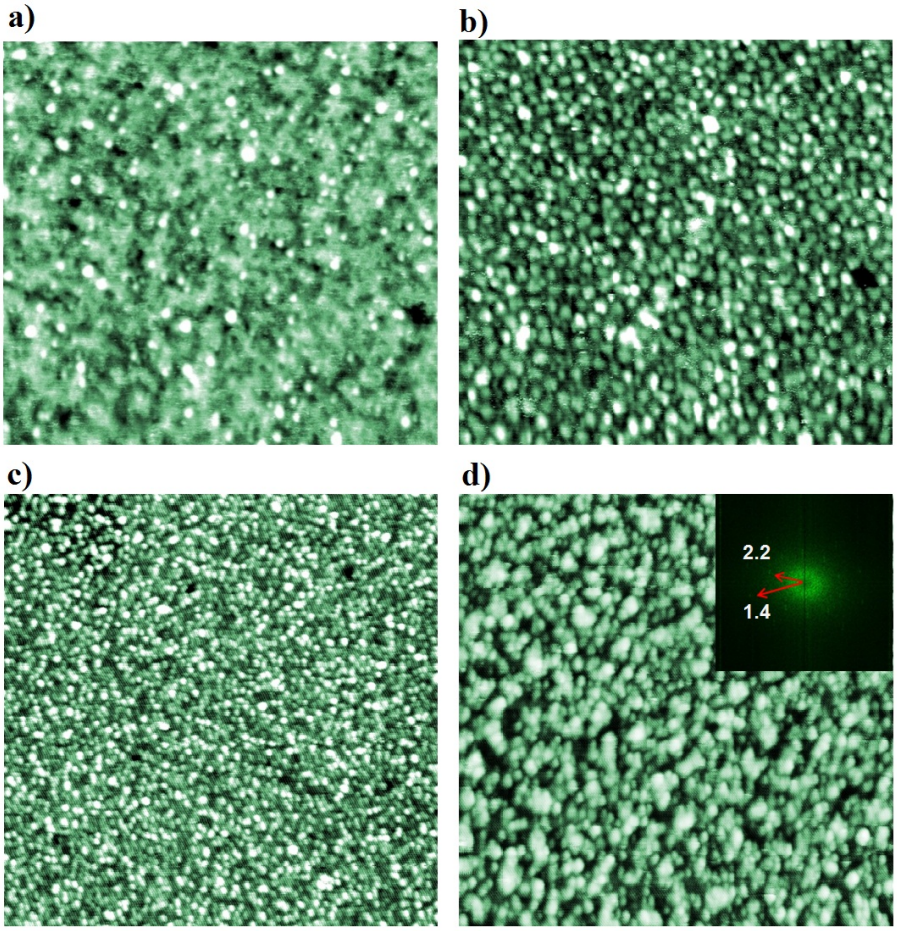

Figure 66: STM images of Cu adsorbed on *i*–Ag–In–Yb at various coverage. a) 75 nm × 69 nm V_{bias}= +1.2 nm b) 75 nm × 69 nm -1.2 nm c) 250 nm × 250 nm 0.51 ± 0.07 ML coverage of Cu. V_{bias}= -2.6 V d) 0.92 ± 0.02 nm 100 nm × 100 nm. The variation in size and irregularity of the clusters is more apparent. Inset: FFT of d). Two faint rings of equally spaced 10 spots in the FFT. The distances these rings correspond to are 2.2 nm and 1.4 nm.

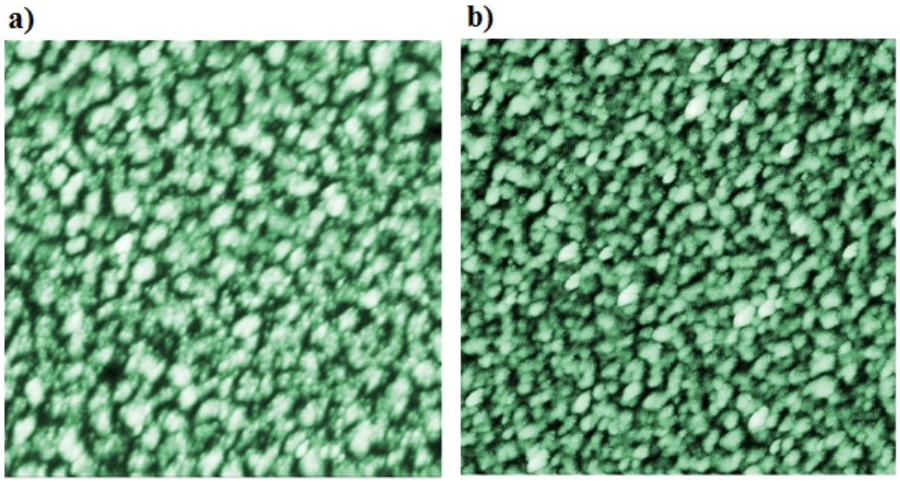

Figure 67: STM images showing multilayer coverage of Cu clusters on *i*–Ag–In–Yb. a)∼2.5 ML 120 nm × 120 nm V_{bias}= +1.1 V b) ∼ 4 ML 200 nm × 200 nm V_{bias}= +1.1 V)

Cu growth on the quasicrystalline Bi monolayer on *i*–Ag–In–Yb

Prior to deposition of Cu a quasicrystalline Bi monolayer was grown on the *i*–Ag–In–Yb surface. Upon deposition of 0.41 ± 0.07 ML of Cu many of the Bi features were simultaneously imaged as can be seen in Figure 68 a) and b). The heavier Bi atoms do not act as a surfactant and hence do not improve the wetting of Cu on the substrate. The average Cu cluster diameter at this coverage is 3.50 nm with a spread of 0.99 nm, indicating that the clusters are marginally smaller and uniform in size compared to a similar coverage Cu on the clean substrate. The average cluster height is slightly larger compared to deposition on the clean surface at 0.253 nm and with a spread of 0.095 nm. There is a clear ring in the FFT corresponding to 1.3 nm. Upon masking out the Bi layer no order was seen in FFTs of the Cu layer.

At multilayer coverage, a disordered arrangement of clusters was observed and the overall surface roughness had increased. Figure 68 c) shows the surface with the irregular shaped, disordered clusters present at a coverage of ∼1.5 ML.

8.4.3 Discussion

The initial layer of Cu islands is close to one monolayer thick. STM images suggest that Cu adsorbs on repeating surface features which are imaged as round protrusions

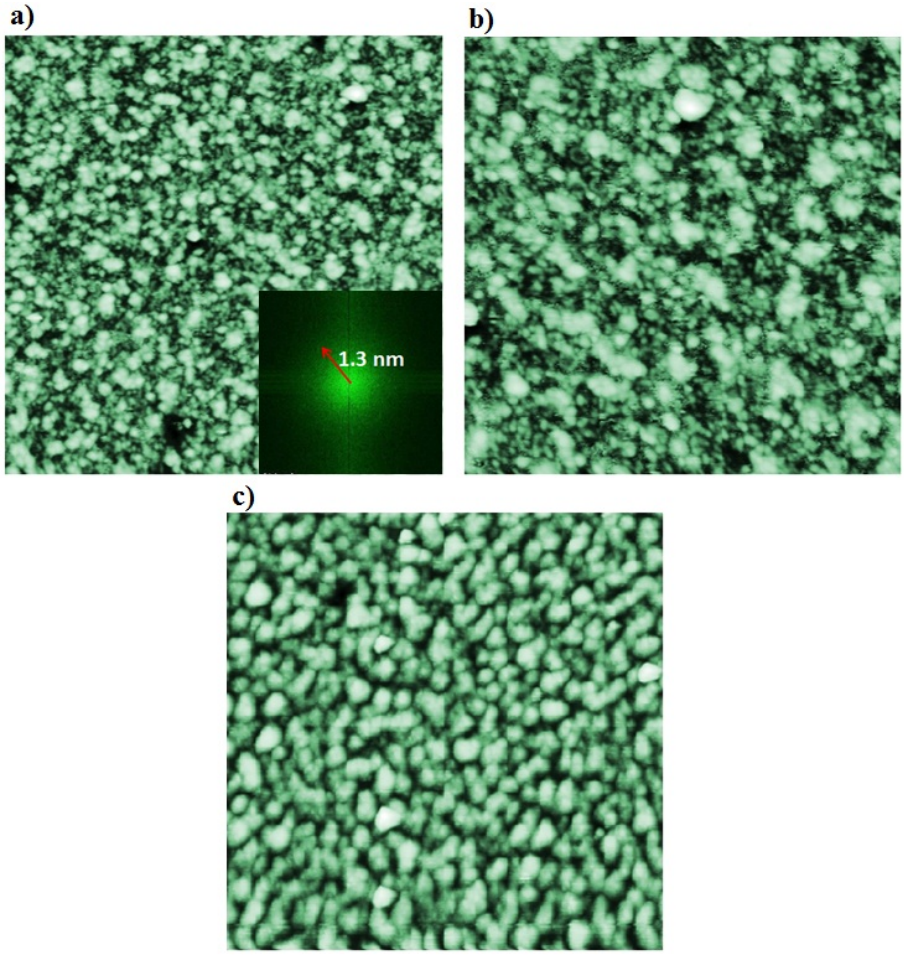

Figure 68: STM images of Cu growth on a quasicrystalline Bi ML formed on i–Ag–In–Yb. a) 75 nm × 75 nm 0.41 ± 0.07 ML of Cu. Inset: FFT of this image with the real space distance to the high symmetry ring marked. b) 50 nm × 50 nm 0.41 ± 0.07 ML c) 120 nm × 120 nm ∼1.5 ML

at negative sample bias. The high symmetry FFTs given by images of the Cu layer at ∼0.9 ML supports nucleation of the Cu at a certain ordered sites on the substrate. From the height of the islands it can be concluded that the next layer of Cu starts to adsorb before the first layer is complete.

The Bi layer did not act as a surfactant for the Cu which supports a strongly bound overlayer of Bi. The resulting Cu layer on the Bi monolayer was clustered and appeared very similar to the layer on the clean quasicrystal surface.

Cu and Ag are both fcc with a lattice parameter mismatch of 24%. Cu on Ag(111) showed epitaxial island growth [164]. LEED patterns showed twinning in the Cu islands. An ordered, smooth bi–layer of Cu formed proceeded by 3–D island

growth [165].

Cu shows a similar disordered layer–by–layer growth on other quasicrystal surfaces. For the initial growth of Cu on *i*–Al–Cu–Fe STM showed growth of a layer of islands one atom in height [166]. Cu deposited on Al–Pd–Mn also displayed almost layer–by–layer growth. At coverages above ∼4 ML the film reorders to epitaxial domains composed of aperiodic rows of a vicinal Cu surface [73, 167] (as described in section 3.2). The islands of Cu in the current system are smaller than the nucleated islands in these two cases.

8.4.4 Conclusions

It can be concluded that the preferred growth mode is Volmer–Weber type for Cu on *i*–Ag–In–Yb on a mediating Bi layer as well as on the clean surface. The first layer of Cu nucleates at quasicrystalline ordered sites. This layer is followed by 3–D growth, which is similar to growth on Ag(111) and other quasicrystal surfaces.

9 Molecular adsorption studies on the fivefold surface of *i*–Ag–In–Yb

9.1 Introduction

This chapter describes experiments where the molecules pentacene and carbon-60 were deposited from vapour onto the high-symmetry surface of *i*–Ag–In–Yb and onto adsorption systems using Ag–In–Yb as a substrate. The same single grain sample with a size of 11.7 mm × 10.6 mm was used for all experiments.

9.2 Experimental Details

The flat, clean surface of a sample with nominal composition *i*–$Ag_{42}In_{42}Yb_{16}$ was prepared as described in Chapter 8. The base pressure of the chamber was 9 × 10^{-11} mbar and the sample was kept at room temperature throughout.

Pentacene powder was evaporated from a simple filament evaporator at a temperature of 390 ± 5 K. Bi was evaporated from a Mo crucible with an e-beam evaporator (same as that used in Chapter 8). Pure C_{60} powder was evaporated from a pyrex tube with a tungsten filament wrapped around it. The molecules were evaporated at a temperature of 470 – 500 K. An Omicron VT-STM instrument was used to acquire scans of the surface at varying coverage.

9.3 Pentacene growth on *i*–Ag–In–Yb

9.3.1 Introduction

This section presents an experimental study of pentacene grown at the five–fold surface of *i*–Ag–In–Yb. There are only a few previous surface and adsorption studies of this high–symmetry surface. Pseudomorphic overlayers of Pb and Sb have been grown at this surface and observed with STM [83, 84]. Molecular adsorption studies at this surface are limited to oxygen [168] and C_{60} dosing [92], where both adsorbates formed disordered overlayers.

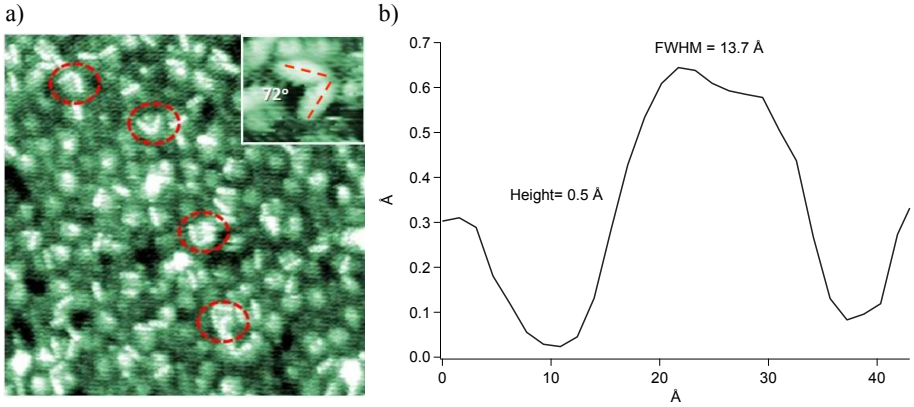

Figure 69: a) 50 nm × 60 nm V_{bias}= -1.1 V High resolution STM image showing 0.16 ± 0.04 ML of pentacene b) Profile along the long molecular axis of one adsorbed molecule. The measured height and full width half maximum (FWHM) are marked.

9.3.2 Results

At doses of pentacene of ∼0.2 ML or less the Ag/In protrusions (the terminated rhombic triacontrahedral clusters from the bulk) of the substrate are imaged simultaneously with the molecules at negative sample bias. These surface features are larger and therefore more easily identifiable, than the features at positive bias. Figure 69 a) shows a section of the surface with 0.16 ± 0.04 ML of pentacene present where the round protrusions are coloured green. The dimensions of the white oblong shapes in this image correspond to individual pentacene molecules adsorbed intact at the surface. Figure 69 b) shows a line profile along the length of one of the molecules. From the height and width of the molecule it was concluded that it is adsorbed with the carbon rings parallel to the surface. The molecules were resolved for a range of tip–sample bias voltage (V_{bias}) of -1.7 – +1.4 V. There was no submolecular resolution for the range of scanning parameters used: for example, the charge density across the molecule in the line profile of Figure 69 b) is quite uniform.

A repeating feature of two molecules adsorbed end–to–end at an angle of 72° relative to one another is observed in the images. These features are highlighted by dashed red rings in Figure 69 a). The feature is even seen to occur in as low a coverage as 0.05 ± 0.02 ML. One such '2–molecule' cluster, with the angle between the longer molecule axis of each marked, is displayed in the top–right inset of Figure 69 a). The angle between the orientation of each molecule is related to five–fold

symmetry (360/5 = 72°). The appearance of clusters and five–fold ordering of pentacene at low, submonolayer coverage suggests that the molecules adsorb at high symmetry sites on the substrate.

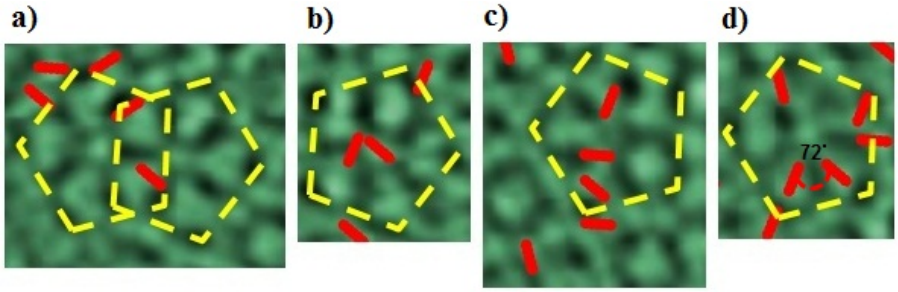

Figure 70: STM images of pentacene on *i*–Ag–In–Yb highlighting the substrate detail and adsorption sites of pentacene at negative bias. Pentacene molecules are marked in red. a) The two different orientations of the pentagon of clusters at 36° to each other. b) Image showing that pentacene adsorbs on top of and at the sides of the round clusters in different orientations. c) Image showing that pentacene adsorbs on top of and at the sides of the round clusters. d) A pentagon of protrusions showing a '2–molecule' clusters adsorbed directly on top of two neighbouring clusters.

High symmetry features were filtered from the FFTs of images at negative bias where the underlying Ag/In surface protrusions were imaged with pentacene molecules. These were then merged with the original images to highlight where pentacene had adsorbed relative to the substrate features. Molecules were found adsorbed at the sides of and on top of the Ag/In substrate protrusions. A few of examples are displayed in Figure 70 a)–d). The pentagons of substrate clusters are marked with a yellow pentagon and the positions of the molecules have been marked with red oblong shapes. A '2–molecule' cluster is present in Figure 70 d) which has been marked by the angle of 72° between the two molecules. The two molecules in this cluster are situated on top of neighbouring round protrusions.

In several images at positive bias filtering the symmetry features from the FFT exposed detail of the Yb rings at the surface. When merged with the original images it was revealed that many of the pentacene molecules were positioned with their ends next to small round holes with a diameter of 0.4 ± 0.1 nm. These holes surround the larger 1.8 nm rings in the FFT filtered image. Figure 71 a) shows an example of one of the filtered images. The red box on the left highlights a position where 3 molecules have adsorbed with their ends next to neighboring 0.4 nm holes as though

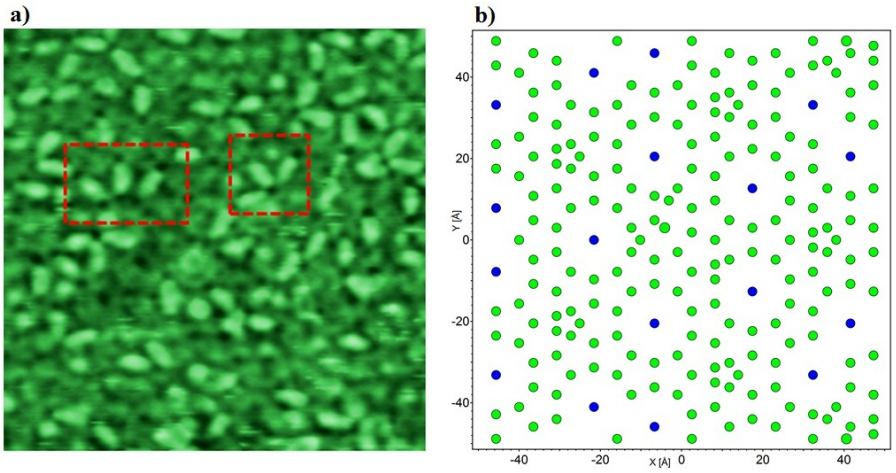

Figure 71: a) (21nm × 21 nm) V_{bias}= 0.4 V ±0.4 ML of pentacene on *i*–Ag–In–Yb. The high symmetry features have been filtered from the FFT and merged with the original image. The boxed areas in red mark areas where several molecules have adsorbed with both ends next to 0.4 nm holes. b) Model of a surface termination of five–fold surface of *i*–Cd–Yb with only the Yb atoms shown. The centres of the truncated RTH clusters are marked also. Yb= Green cluster centre= Blue.

they avoid the holes. The boxed area on the right shows a cluster where 3 molecules have nucleated at a single hole. These holes can be identified from the surface model of the Yb atoms in the isostructural *i*–Cd–Yb displayed in Figure 71 b). The blue cluster centres marked are surrounded by a 1.8 nm Yb ring of 10 atoms. This ring can be further extended to 10 interpenetrating pentagons of atoms with a vertice to opposite edge distance of 0.4 nm.

In general, the substrate resolution is greatly reduced when greater than ∼0.2 ML of pentacene is present. Only some exposed Yb rings are imaged at positive bias. A couple of these rings are shown in Figure 2 a) with a measured diameter of 1.8 nm. Figure 72 b) shows a typical image from 0.38 ± 0.06 ML of adsorbed pentacene. The most conspicuous feature in the STM images is an isolated, repeating cluster containing three molecules. Constant angles related to pentagonal symmetry are measured between the molecules marked in Figure 73 a). Many '2–molecule' clusters are observed also. The '3–molecule' cluster is an extension of the '2–molecule' cluster leading to an almost complete triangle of pentacene molecules. At a coverage of 0.6 ML there is a much greater density '3 molecule' clusters as highlighted by the dashed red squares in Figure 73 b).

Figure 74 a) shows a larger scale image of 0.50 ± 0.06 ML of pentacene on

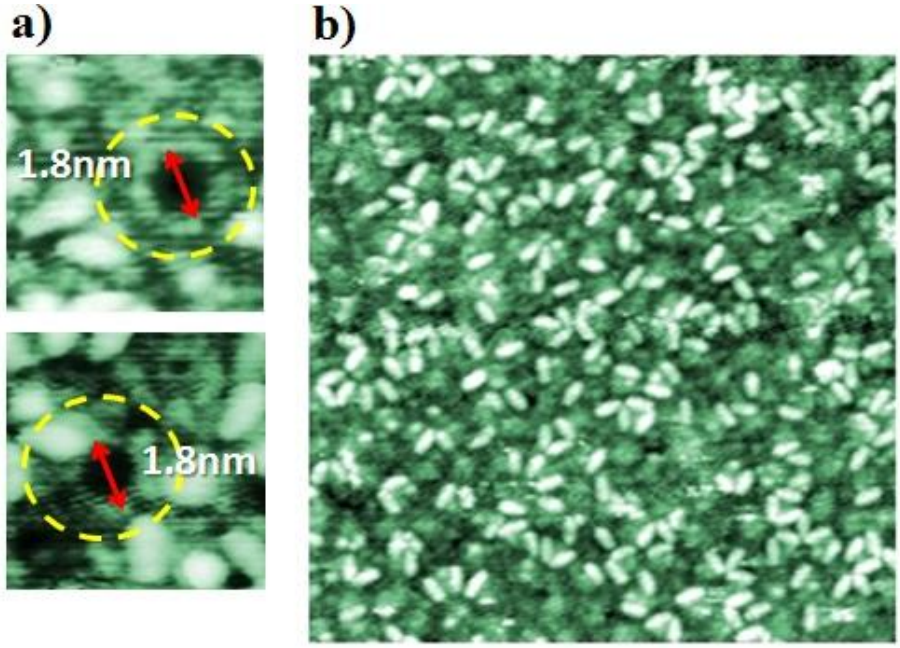

Figure 72: a) Two examples of Yb–rings imaged from the substrate at positive bias V_{bias}= +0.4 V, after the deposition of 0.38 ± 0.06 ML of pentacene. b) 40 nm × 40 nm 0.38 ± 0.06 ML V_{bias}= -0.74 V

the quasicrystal surface. A 10–fold FFT is observed after height filtering out the substrate features with an appropriate mask. There is significant orientational order of the molecules' long axes relative to each other. The histogram in Figure 74 b) shows the relative orientations measured from 397 molecules. The average angle between cluster centres is 36 ± 5°.

The complete monolayer is imaged clearly with many '3-molecule' clusters still observable – see Figure 75 a). Close to a monolayer coverage many molecules align side–by–side, in the same orientation. The total surface density of the molecules measured from applying a watershed algorithm to images is 2.7 × 10^{-13}molecules cm^{-2}. It is noticeable that a proportion of molecules have adsorbed at a common nucleation point at 72° to one another. In several cases this cluster of molecules is complete with 5 molecules, an individual example of this feature is shown in Figure 75 b). We have termed these features 'star' clusters. Many partial 'star' clusters can be identified in the monolayer. Examples of partial 'stars' with at least 3 consecutive arms have been circled in Figure 75 a).

Another apparent formation of several molecules is partial decagonal rings as

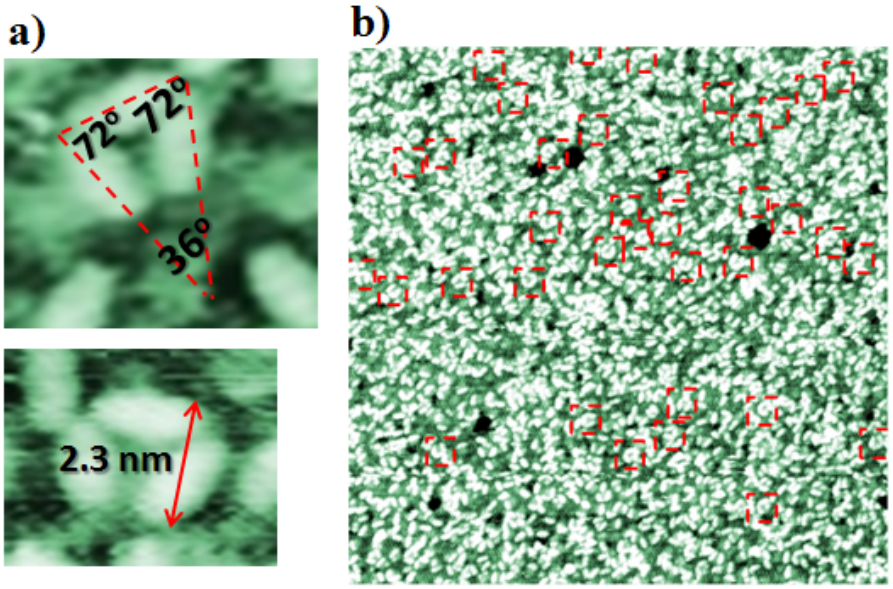

Figure 73: a) Two individual '3–molecule' clusters with their dimensions marked. b) 95 nm × 95 nm V_{bias}= -1.6 V 0.6 ML of pentacene. Dashed red squares mark the positions of the '3–molecule' clusters. The dashed red circle marks a complete star cluster.

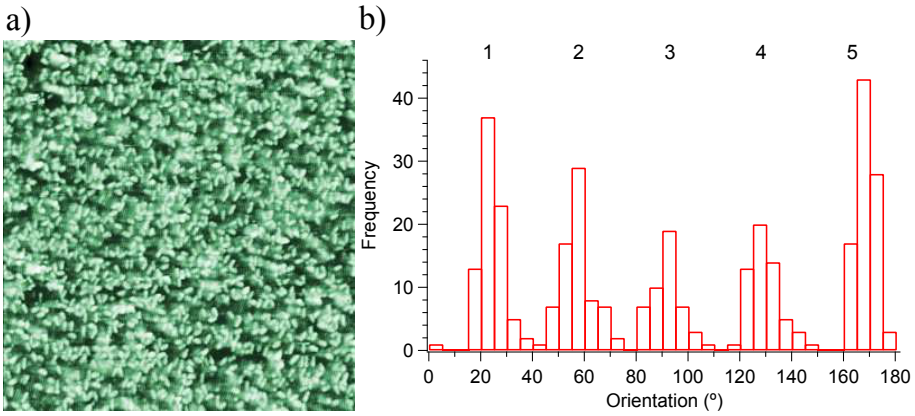

Figure 74: a) 80 nm × 80 nm V_{bias}= -0.95 V 0.50 ± 0.06 ML of pentacene. b) Histogram of the orientations of the long molecular axis of pentacene molecules adsorbed on the *i*–Ag–In–Yb quasicrystal. The measurements are acquired from images with 0.38 – 0.50 ML of pentacene deposited. The clusters are numbered 1–5.

highlighted in Figure 76 a). Here several molecules have adsorbed end-to-end with 36° between the orientation of their long axes for consecutive molecules. This feature – composed of 3 or 4 molecules, – is only observed at monolayer coverage. At lower coverage there are examples of two molecules adsorbed end–to–end at 36° as

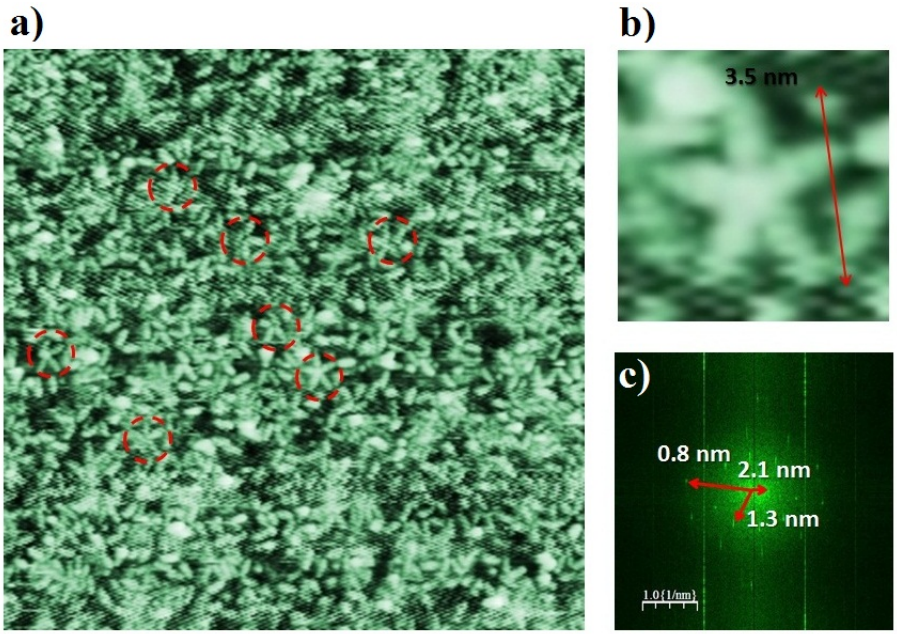

Figure 75: a) 1.0 ± 0.1 ML 60 nm × 60 nm V_{bias}= -0.69 V b) Individual, complete 'star' cluster with its diameter marked. c) FFT from a large scale STM image of a complete ML of pentacene on *i*–Ag–In–Yb

shown in Figure 76 b). If this partial ring was extended it would form a decagon of pentacene as highlighted from extending the partial decagonal rings in Figure 76 c). By measuring the distance between the ends of partial rings and extrapolating the actual ring the diameter of such rings was found to be 6.3 ± 0.3 nm. This would be quite a large molecular structure and shows that the variation of the length scales of the substrate features that influence the molecules adsorption. This measured diameter corresponds to an edge length of 1.9 nm which is large than the measured length of an isolated molecule of 1.5 nm. This suggests a small gap of ∼0.2 nm either side of each molecule when adsorbed next to each other in a partial ring. Figure 76 d) shows the a structural model of the 5-fold surface of *i*–Cd–Yb which is isostructural to *i*–Ag–In–Yb. The 1.3 nm clusters are indicated by blue rings. The 6.3 nm diameter ring of pentacene is depicted by blue ovals. The suggested adsorption site for the ring is around the pentagon of five of the 1.3 nm protrusions. The pentacene is adsorbed on the edges of the larger Yb rings and between smaller, top-layer clusters of Ag/In.

A clear FFT with 10–fold rotational symmetry is obtained from larger scale images of a single terrace with a monolayer present. An FFT from one of these

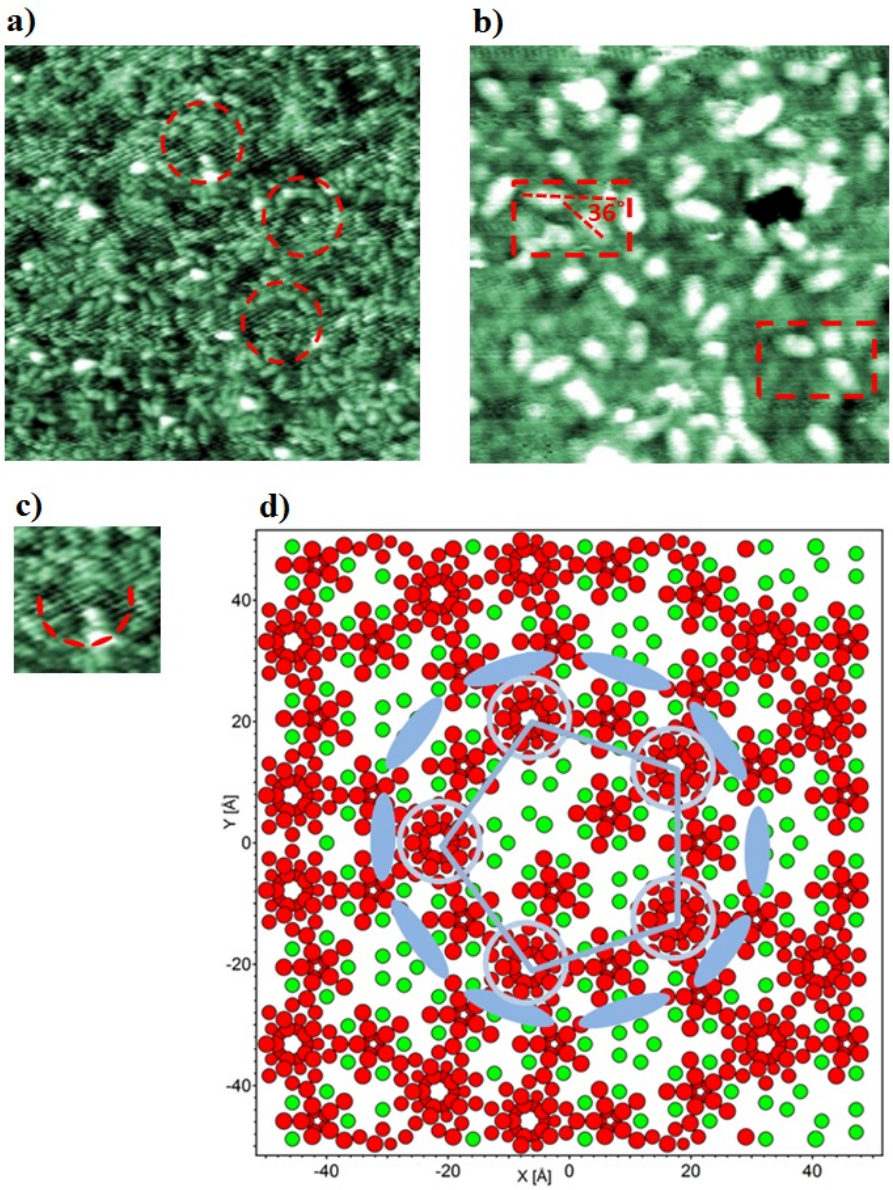

Figure 76: Example of partial rings of pentacene adsorbed on *i*–Ag–In–Yb. a) 40 nm × 40 nm ∼1.0 ML b) 16 nm × 16 nm 0.45 ML of pentacene c) An example of one of partial ring of pentacene extended with red ovals as other molecules to help visualise it as part of a decagon. d) Surface model of the isostructural CdYb quasicrystal used to determine the possible adsorption site of ring. Cd/(Ag/In)= Red Yb= Green. The 6.3 nm ring of pentacene is represented by 10 blue ovals. The 1.3 nm diameter clusters are marked and the 2.3 nm edges of a pentagon of clusters are marked.

images is shown in Figure 75 c) where several rings of 10 distinct spots are obtained. The equivalent, real space, radial distances between the rings have been marked. The distances of ∼1.3 nm and ∼2.1 nm are close to distances observed in FFTs from the clean surface. The ratio of the radial distances to the rings is approximately equal to the golden mean ($\tau = 1.61803$). This ratio is synonymous with icosahedral quasicrystalline order and indicates positional ordering of molecules.

Figure 77 a) shows the surface with ∼1.2 ML of pentacene present. The second layer adsorbs in unresolved clumps that inhibit the imaging of the first layer. The height of clusters is consistent with a second flat layer of pentacene. Some isolated, individual molecules were discerned in the second layer. A couple of examples of these molecules are shown in Figure 77 b). They appear to be in a flat geometry much like the first layer. At 1.7 ML a faint, large 10–fold FFT ring is still observed in the FFT of terrace images. No ordered LEED pattern from the pentacene was observed from 1 ML, 1.2 ML or 1.7 ML coverages. The ordered LEED pattern from the substrate is observed to gradually fade until just above a ML of pentacene.

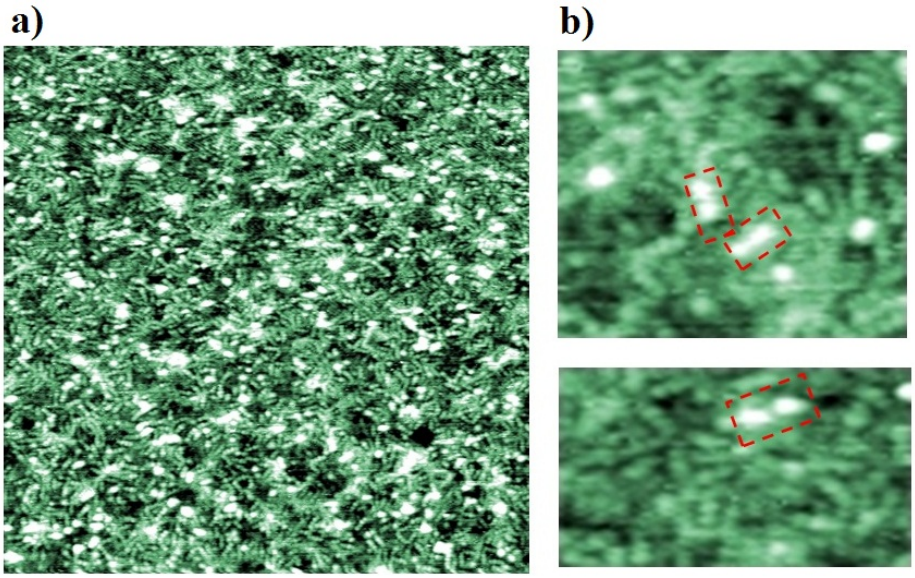

Figure 77: a) ∼1.2 ML of pentacene 60 nm × 60 nm The second layer is highlighted in white. b) Cases of individual pentacene molecules in the second layer. The molecules are highlighted in white and boxed in red.

9.3.3 Discussion

The pentacene/Ag(111) system has been previously investigated with density functional theory (DFT) [107] and near–edge x-ray absorption fine structure (NEXAFS) [169], x–ray photoelectron spectroscopy (XPS), low energy electron diffraction (LEED), high resolution electron energy loss spectroscopy (HREELS), and scanning tunnelling microscopy (STM) [170]. NEXAFS evidenced that the first layer is chemisorbed flat with slight tilt of 10° [169]. STM and LEED suggested a disordered first layer then ordered multilayers that are influenced by steps at the surface [170]. In contrast, DFT showed a specific, energetically preferred site for first layer pentacene with the molecules aligned along the Ag rows at the surface [107]. It was concluded that the molecule–surface interaction was quite weak.

The molecules have the same adsorption geometry as on other ordered, metal surfaces; adsorbed flat with the phenyl rings parallel to the surface. The constant charge density across the profile of molecule for the range of tunnelling conditions used suggests that there is no distortion of the electronic or atomic structure of the molecule. Such an observation suggests that there is a not a large amount of charge transferred between the molecule and substrate, in agreement with deposition on crystalline Ag [107].

From the filtered images of a submonolayer of pentacene one can determine that there are several different adsorption sites as the molecules are present on top of and inbetween the truncated RTH clusters at the surface.

The quasicrystalline order observed in FFTs of images of half a monolayer of pentacene with the substrate masked out signifies a highly ordered film. The histogram shows how the majority of anisotropic molecules lie in several distinct orientations related to 5–fold symmetry. These results indicate that the positions of the energetically favoured adsorption sites are aperiodically distanced from each other and that the linear molecules can only adsorb at certain orientations within them.

The second layer molecules show that the thin film growth continues layer–by–layer. There is no evidence that this second layer is ordered with this technique. Bulk–like periodic, thin film phase growth may proceed beyond these layers. The change in structure is not so abrupt between the quasicrystal and bulk molecule phase due to the quasicrystalline molecular layer. These layers could then act as a successful interface for surface coating and electrical transport applications.

Overall, one can see that pentacene prefers to adsorb along high symmetry directions of the substrate and at 72° to one another when touching. This result indicates that the correct balance of substrate–adsorbate and adsorbate–adsorbate interactions are present to lead to selective site adsorption. It also indicates that at room temperature the molecules are able to overcome barriers to surface diffusion and hence reach the high surface energy sites. If there were little influence of the substrate on the incident molecules an incommensurate or disordered layer would be expected. The smaller, attractive van der Waals forces between the molecules may contribute to the formation of the 2–molecule, 3–molecule and star clusters with the molecules inclined to lying end–to–end.

9.3.4 Summary

Pentacene adsorbed on Ag–In–Yb has been shown to be a strong candidate for a complete quasiperiodic molecular overlayer. STM shows clear 10–fold orientational order in the complete monolayer, with many aggregates of several molecules in structure with pentagonal symmetry. FFTs of the images from the first layer indicate high positional ordering of the molecules.

9.4 C_{60} growth on the quasicrystalline Bi monolayer on *i*–Ag–In–Yb

9.4.1 Introduction

In this study STM was used to monitor the local growth of a monolayer of C_{60} on a quasicrystalline Bi surface layer formed on *i*–Ag–In–Yb. The reader is referred to Section 3.4 for an introduction to C_{60} and a short review on epitaxial growth of C_{60}. There have been extensive studies on C_{60} growth at quasicrystal surfaces. The molecule has been shown to adsorb in a disordered fashion on *i*–Ag–In–Yb [92] and *d*–AlNiCo [91]. A τ–scaled relationship was observed between the relative positions of C_{60} deposited on the *i*–Al–Pd–Mn surface at low coverage, suggesting some preferred adsorption sites [93]. There is greater ordering of the molecules when the surface is passivated with a quasicrystalline overlayer. Periodic, hexagonal close packed (hcp) structured domains have been produced on quasicrystalline Bi [150] and on a Pb monolayer [80].

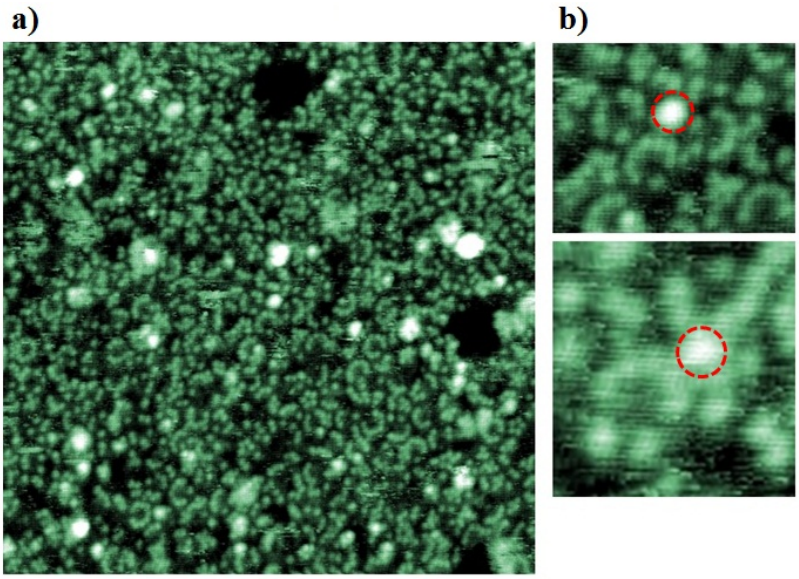

Figure 78: a) 50 nm × 50 nm 0.05 ± 0.01 ML of C_{60} Tip-sample bias -1.1 V b)Examples of C_{60} showing isolated molecules adsorbed between decagonal rings. The C_{60} molecules are highlighted in white and encircled with red rings.

9.4.2 Results

Atomic resolution from the quasicrystalline Bi adlayer is more easily achievable at the surface after the deposition of a minimal amount of C_{60}. This is perhaps due to the a C_{60} molecule attaching itself to the end of the tip in an orientation so that the tunnelling occurs through a single C atom thus improving the resolution. Such resolution is displayed in Figure 78 a), where the C_{60} is highlighted in white. The molecules are mostly imaged as round protrusions with a diameter of ∼1 nm and a height of ∼0.26 nm above the Bi layer. In many images at this coverage individual molecules were observed positioned between partial decagonal rings of Bi. A couple of these cases are shown in Figure 78 b). FFT filtered and merged images also showed that the molecules were positioned on the bridge between the rings of Bi.

At a higher coverage of C_{60} many triangular clusters and 'curves' of 3 – 4 molecules were present at the surface. Such features are highlighted by dashed red rings and boxes in the STM image of Figure 79 a). Pentagonal and decagonal angles between molecules' positions are measured as in the images of Figure 79 b). These features are partial pentagons and decagonal rings of C_{60}. The right–hand image of Figure 79 c) shows an almost complete pentagonal cluster of molecules and the

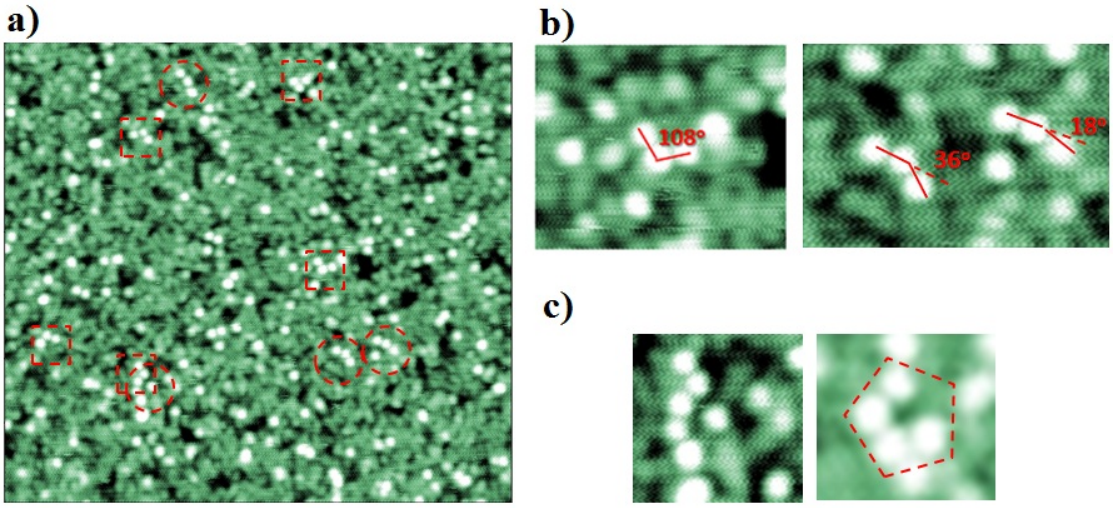

Figure 79: a) 80 nm × 72 nm 0.08 ML of C_{60} V_{bias} +1 V b) Closely adsorbed curves of C_{60} at the surface. c) Clusters with pentagonal angles between their relative positions. A partial decagonal ring of molecules and a partial pentagon cluster of molecules.

left–hand side shows the most complete decagonal motif found at the surface. The ordering of the molecules into clusters with geometries inherent to quasicrystalline order shows that the Bi monolayer influences the adsorption of the molecules.

The local ordering of C_{60} does not persist at higher coverages. At 0.21 ML (Figure 80 a)) high resolution of the Bi layer is still attained and quasicrystalline order is still apparent in FFTs of images at this coverage.

At 0.36 ML the Bi is still resolved and some curves and triangles of molecules can be identified (see Figure 80 b)). Even so, the FFTs of images from this coverage show no clear order. The height at which the molecules protrude above the surface varies between 0.4 - 0.6 nm. By 0.59 ML (Figure 80 c)) of C_{60} the Bi layer was not imaged and the molecules showed no order. The near completed monolayer was disordered and had a RMS roughness of 0.052 nm. The layer is one molecule high although the height of the molecules adsorbed at the surface varies.

9.4.3 Conclusions

Growth of C_{60} on a quasicrystalline Bi layer, at room temperature, leads to the formation of a disordered layer. The intermolecular interaction is not strong enough

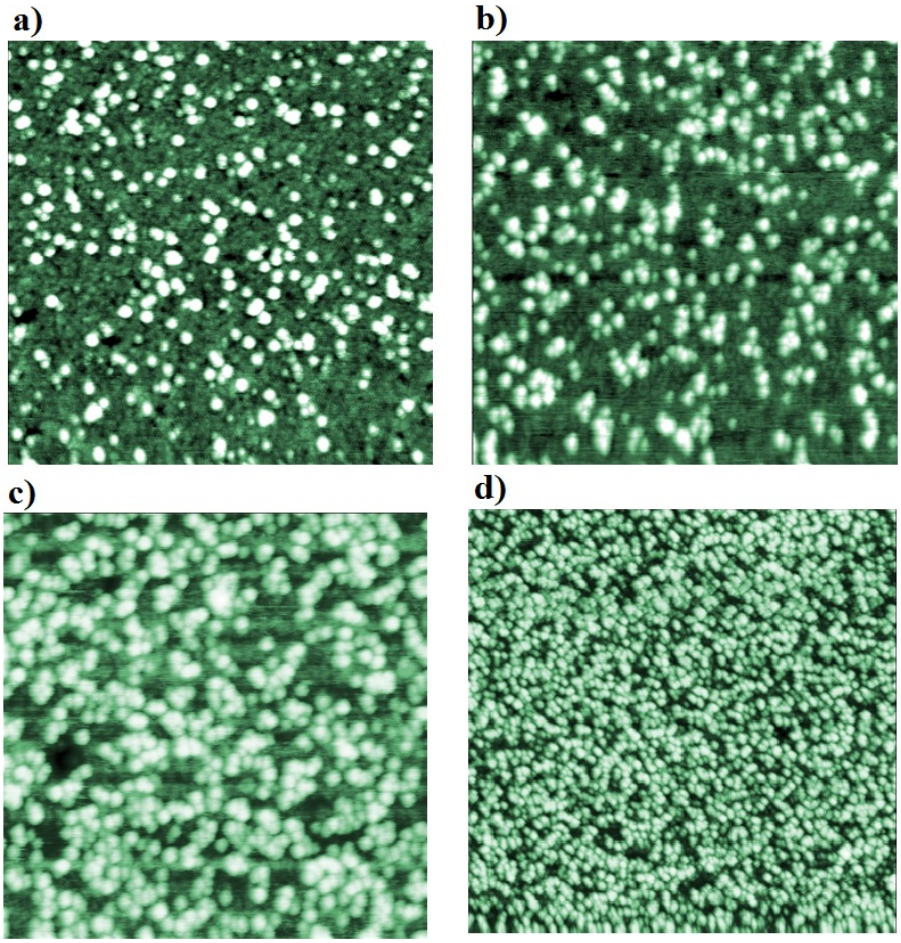

Figure 80: Image of C_{60} adsorbed on a Bi monolayer on *i*–Ag–In–Yb at various coverages. a) 80 nm × nm 0.21 ML of C_{60} b) 60 nm × 60 nm 0.36 ML c) 60 nm × 60 nm 0.59 ML of C_{60}. There is no clear resolution of substrate features at this coverage. Root–mean squared (RMS) roughness 0.079 nm d) 150 nm × 150 nm 0.83 ML of C_{60}. The layer formed is disordered. RMS roughness 0.052 nm.

relative to the molecule–surface forces to cause a periodic, close–packed structure to form. This system is similar to growth of C_{60} on the clean surface of *i*–Ag–In–Yb. The ordered, partial clusters and evidence for adsorption between the decagonal Bi rings suggest that the reactivity of the surface has decreased relative to the clean surface. The varying heights of the molecules above the surface suggests several different adsorption sites.

10 Summary and future work

This work has contributed to the advancement of the understanding of surface reactions, heteroepitaxial growth and elucidating thin film structures at quasicrystal surfaces using surface science techniques. The thesis also demonstrates that scanning tunnelling microscopy is a very useful technique for directly imaging features at such complex aperiodic surfaces.

The semi–metal Bi and the aromatic molecule pentacene formed the most successful epitaxial layers on icosahedral quasicrystals. This conclusion is drawn from this work and the previous literature involving these adsorbates. Minimal amounts or the complete absence of epitaxial growth was observed for pentacene on *i*–Al–Pd–Mn, pentacene/ Bi/*i*–Al–Pd–Mn, C_{60} on Bi /*i*–Ag–In–Yb and Cu on Ag–In–Yb systems. Varying degrees of epitaxial growth was evident for Bi/Al–Pd–Mn, pentacene on Cu/*i*–Al–Pd–Mn and pentacene on *i*–Ag–In–Yb. We can see a large variation between the growth mode of Cu and pentacene on Ag–In–Yb, and the same species on Al–Pd–Mn. The difference in epitaxial growth at the surfaces of these icosahedral quasicrystals is likely to be due to different sized features at the surface (laterally and vertically) and the individual chemical reactivity of different elements in the surface. Larger molecules complicate the adsorption further and make it difficult to determine the adsorption site with STM alone.

Summary of metal growth

XPS verified a Stranski–Krastanov growth mode of Bi on *i*–Al–Pd–Mn and the relative stability of the Bi monolayer under the crystalline Bi islands. The structure of the different Bi allotropes at the surface was confirmed with atomic resolution STM. The formation of each allotrope was found to be dependent on the Bi flux and coverage. Increasing the Bi flux for deposition was found to increase the nucleation density of the rectangular islands inhibiting the transformation to the lower energy triangular islands. LEED showed that the larger {111}–rhombohedral islands were aligned with the substrate whereas the {012}–rhombohedral islands were randomly orientated.

A complete pseudomorphic ML of Bi was studied at the surface of *i*–Ag–In–Yb. The monolayer was composed of clusters similar to that found in the growth of other semi–metals at this surface.

STM images of the growth of Cu on *i*–Ag–In–Yb shows irregular clusters that proceeded to grow into a disordered 3–D layer. Analysis of the initial clusters shows that Cu absorbs on the aperiodically arranged, truncated RTH clusters leading to some ordering in first layer before clusters coalesce at higher coverage.

Pentacene adsorption and the quasiperiodic molecular overlayer

The quest for a quasiperiodic molecular layer was extended to studies with acene deposition. This venture was more successful than investigations involving other molecules. Pentacene is highly stable and therefore adsorbs intact at the surface like other aromatic molecules i.e. benzene and C_{60}. Van–der–Waals forces govern intermolecular interactions which are smaller than those for C_{60}. As a result pentacene did not form bulk–like ordered adsorbate domains. Pentacene had a strong reaction at the quasicrystal surfaces, similar to that at other metal surfaces. This gave rise to a 'lying down' adsorption geometry and in some cases distortion of the molecule with the most reactive central aromatic ring bonded to the surface. This sub–molecular distortion was greater for adsorption on Al–Pd–Mn and Bi/Al–Pd–Mn compared to Cu/Al–Pd–Mn and Ag–In–Yb suggesting stronger chemisorption of the molecules on the former substrates.

The structure of an adsorbed pentacene molecule on *i*–Al–Pd–Mn suggested the molecule is chemisorbed at the surface through the central carbon rings. Although at low coverage some closely adsorbed molecules were at pentagonal angles relative to each other the complete layer was disordered. The same growth characteristics were observed for deposition on the quasicrystalline Bi monolayer. There was some evidence of side–by–side ordered rows on the rectangular {100}–pseudocubic islands.

Pentacene formed a periodic structure along the domains of an aperiodic, vicinal Cu multilayer on *i*–Al–Pd–Mn. This incommensurate layer begins to form as molecules attempt to fit laterally across the rows. These rows continue to grow, layer–by–layer directly on top of the first layer molecules.

The project was successful in producing the first molecular quasiperiodic overlayer observed in an experiment. Pentacene deposited on *i*–Ag–In–Yb resulted in epitaxial growth with orientational and positional ordering of the molecules. A large degree of orientational alignment of pentacene along high symmetry directions of the

substrate was evidenced. It was affirmed that there was quasicrystalline order in the complete monolayer.

STM measurements show that the clean, five–fold surface of Al–Pd–Mn and Ag–In–Yb have a very similar root mean squared roughness of around ∼0.017 nm. The component atoms of Ag–In–Yb are all larger than those of the elements in Al–Pd–Mn. Additionally, the surface clusters are slightly larger on Ag–In–Yb compared to Al–Pd–Mn and are closer to the length of a pentacene molecule (∼1.4 nm). For example, the diameter of a 'white flower' on Al–Pd–Mn is 1 nm whereas the round protrusions on Ag–In–Yb are 1.3 nm. The relatively larger 5–fold features at the surface of Ag–In–Yb compared to Al–Pd–Mn may be a major contributing factor to the epitaxial growth of pentacene at these surfaces. The size of these high–symmetry features and micropores on the Ag–In–Yb surface may be able to accommodate a complete pentacene molecule in a certain position leading to five–fold, epitaxial growth. The high-symmetry Al–Pd–Mn features may be too small to influence the adsorption geometry of the molecules significantly, leading to disordered growth.

Modified growth by a pseudomorphic Bi layer

Overall, an interfacial Bi layer had little influence on the growth mode at the surface. For the systems examined the layer had no effect or a worsening effect for the order in pentacene and Cu growth. There was a small improvement for C_{60} ordering. Some partial local clusters possessing 5– or 10–fold symmetry formed at low submonolayer coverage which were absent in a similar study on the clean surface.

Future work

The current project work will be extended to include an STM and LEED study of pentacene on the pseudomorphic Pb layer on *i*–Al–Pd–Mn. The Pb layer shows a high degree of order after annealing. Such a study would be interesting for comparison with the influence of a Bi layer on the growth of epitaxial overlayer. C_{60} forms larger domains on this Pb surface compared to on Bi suggesting a smaller influence on incident molecules.

To complete the Bi layer studies of pentacene, C_{60} and Cu adsorption requires pentacene adsorption on Bi/*i*–Ag–In–Yb to be similarly investigated for comparison.

It would be beneficial to measure the tribology and electrical properties of a quasiperiodic pentacene layer as there is no research on the properties of such quasiperiodically ordered, organic semiconducting thin layers.

It would be interesting to see if similar epitaxial phenomena occur on i–Al–Cu–Fe as it is the cheapest quasicrystal to produce and hence future possible applications of thin organic films would be more commercially feasible.

References

[1] D. Schechtman, I. Blech, D. Gratias, and J. W. Cahn. Metallic Phase with Long-Range Orientational Order and no Translational Symmetry. *Phys. Rev. Lett.*, 53:1951 – 1953, 1984.

[2] J. M. Dubois. *Useful Quasicrystals*. World Scientific Publishing Company; 1st edition, 2003.

[3] B. Grushko and T.Ya. Velikanova. Stable and metastable quasicrystals in Al-based alloy systems with transition metals. *Journal of Alloys and Compounds*, 367:58 – 63, 2004.

[4] N. Wang, H. Chen, and K. H. Kuo. Two-Dimensional Quasicrystal with Eightfold Rotational Symmetry. *Phys. Rev. Lett.*, 59:1010 – 1013, 1987.

[5] L. Bendersky. Quasicrystal with One-Dimensional Translational Symmetry and a Tenfold Rotation Axis. *Phys. Rev. Lett.*, 55:1461 – 1463, 1985.

[6] T. Ishimasa, H. U. Nissen, and Y. Fukano. New Ordered State Between Crystalline and Amorphous in Ni-Cr Particles. *Phys. Rev. Lett.*, 55:511 – 513, 1985.

[7] L. Bindi, P. J. Steinhardt, N. Yao, and P. J. Lu. Natural Quasicrystals. *Science*, 324:1306 – 1309, 2009.

[8] L. Bindi, J. M. Eiler, Y. Guan, L. S. Hollister, G. MacPherson, P. J. Steinhardt, and N. Yao. Evidence for the extraterrestrial origin of a natural quasicrystal. *Proceedings of the National Academy of Sciences of the United States of America*, 109:1396 1401, 2012.

[9] J. M. Dubois. New prospects from potential applications of quasicrystalline materials. *Materials Science and Engineering*, 294 - 296:4 – 9, 2000.

[10] B. Grunbaum and G.C. Shephard. *Tilings and Patterns*. W.H. Freeman and Co Ltd, 1986.

[11] J. Ledieu, A.W. Munz, T.M. Parker, R. McGrath, R.D. Diehl, D.W. Delaney, and T.A. Lograsso. Structural study of the five-fold surface of the $Al_{70}Pd_{21}Mn_9$ quasicrystal. *Sur. Sci.*, 433:666 – 671, 1999.

[12] P. Kramer, Z. Papadopolos, and H. Teuscher. Tiling theory applied to the surface structure of icosahedral AlPdMn quasicrystals. *J. Phys.: Condens. Matter*, 11:2729 – 2748, 1999.

[13] A.i Yamamoto. Crystallography of Quasiperiodic Crystals. *Acta Cryst.*, 52:509 – 560, 1996.

[14] M. de Boissieu, H. Takakura, C. Pay Gómez, A. Yamamoto, and A. P. Tsai. Structure determination of quasicrystals. *Phil. Mag.*, 87:2613 – 2633, 2006.

[15] Cesar. P. Gómez and S. Lidin. Comparative structural study of the disordered MCd_6 quasicrystal approximants. *Phys. Rev. B*, 68:024203, 2003.

[16] W. Steurer. Stable clusters in quasicrystals: fact or fiction? *Phil. Mag.*, 86:1105 – 1113, 2006.

[17] L. Beraha, M. Duneau, K. Klein, and M. Audier. Correlated phason jumps involved in plastic deformation of Al-Pd-Mn approximant phases. *Phil. Mag.*, 76:587 – 613, 1997.

[18] Ph. Ebert, M. Feuerbacher, N. Tamura, M. Wollgarten, and K. Urban. Evidence for a Cluster-Based Structure of AlPdMn Single Quasicrystals. *Phys. Rev. Lett.*, 77:3827 3830, 1996.

[19] V. E. Dmitrienko, S. B. Asta'fev, and Maurice Klémanb. Growth, melting, and clustering of icosahedral quasicrystals: Monte Carlo simulations. *Materials Science and Engineering A*, 294:413 – 417, 2000.

[20] A. S. Keys, , and S. C. Glotzer. How do Quasicrystals Grow? *Phys. Rev. Lett.*, 99:1 – 4, 2007.

[21] T. Fujiwara and Y. Ishii. Quasicrystals. *Elsevier*, 3:49 – 54, 2007.

[22] A. P. Tsai, A. Inoues, Y. Yokoyama, and T. Masumoto. New icosahedral alloys with superlattice order in the Al-Pd-Mn system prepared by rapid solidification. *Phil. Mag. Lett.*, 61:9 – 14, 1990.

[23] A.P. Tsai, Y. Yokoyama, A. Inoue, and T. Masumoto. Chemically driven structural change in quasicrystalline Al-Pd-Mn alloys. *J. Non-Crys. Solids*, 150:327 – 331, 1992.

[24] M. Boudard, M. de Boissieu, C. Janot, G. Heger, C. Beeli, H. U. Nissen, H. Vincent, R. Ibberson, M. Audier, and J. M. Dubois. Neutron and X-ray single-crystal study of the AlPdMn icosahedral phase. *J. Phys.: Condens. Matter*, 4:10149, 1992.

[25] M. de Boissieu, P. Stephens, M. Boudard, C. Janot, D. L. Chapman, and M. Audier. Anomalous X-ray diffraction study of the AlPdMn icosahedral phase. *J. Phys.: Condens. Matter*, 6:10725, 1994.

[26] A. Fang, H. Zou, F. Yu, R. Wang, and X. Duan. Structure refinement of the icosahedral AlPdMn quasicrystal using quantitative convergent beam electron diffraction and symmetry-adapted parameters. *J. Phys.: Condens. Matter*, 15:4947 – 4960, 2003.

[27] M. Gierer, M. A. Van Hove, A. I. Goldman, Z. Shen, S.-L. Chang, C. J. Jenks, C.-M. Zhang, and P. A. Thiel. Structural Analysis of the Fivefold Symmetric Surface of the $Al_{70}Pd_{21}Mn_9$ Quasicrystal by Low Energy Electron Diffraction. *Phys. Rev. Lett.*, 78:467 – 470, 1997.

[28] Z. Shen, W. Raberg, M. Heinzig, C. J. Jenks, V. Fournée, M. A. Van Hove, T. A. Lograsso, D. Delaney, T. Cai, P. C. Canfield, I. R. Fisher, A. I. Goldman, M. J. Kramer, and P. A. Thiel. ALEED comparison of structural stabilities of the three high–symmetry surfaces of Al-Pd-Mn bulk quasicrystals. *Sur. Sci.*, 450:1 – 11, 2000.

[29] D. Rouxela, T. H. Caib, C. J. Jenks, T. A. Lograsso, A. Ross, and P. A. Thiel. Structural aspects of the threefold surface of icosahedral Al-Pd-Mn. *Sur. Sci.*, 461:521 527, 2000.

[30] H. J Günther odt T. M. Schaub, D. E. Bürgler and J. B. Suck. Quasicrystalline Structure of Icosahedral $Al_{68}Pd_{23}Mn_9$ Resolved by Scanning Tunneling Microscopy. *Phys. Rev. Lett.*, 73:12551258, 1994.

[31] J. C. Zheng, C. H. A. Huan, A. T. S. Wee, M. A. Van Hove, C. S. Fadley, F. J. Shi, E. Rotenberg, S. R. Barman, J. J. Paggel, K. Horn, Ph. Ebert, and K. Urban. Atomic-scale structure of the fivefold surface of an AlPdMn quasicrystal: A quantitative x-ray photoelectron diffraction analysis. *Phys. Rev. B*, 69:134107, 2004.

[32] B. Unal, C.J. Jenks, and P.A. Thiel. Comparison between experimental surface data and bulk structure models for quasicrystalline AlPdMn: Average atomic densities and chemical compositions. *Phys. Rev. B*, 77:195419, 2008.

[33] M. Krajci, J. Hafner, J. Ledieu, and R. McGrath. Surface vacancies at the fivefold icosahedral Al-Pd-Mn quasicrystal surface: A comparison of ab initio calculated and experimental STM images. *Phys. Rev. B*, 73:024202, 2006.

[34] H. Takakura, C. P. Gomez, A. Yamamoto, M. de Boissieu, and A. P. Tsai. Atomic structure of the binary icosahedral Yb-Cd quasicrystal. *Nature Materials*, 6:58 – 63, 2006.

[35] A. P. Tsai, J. Q. Guo, E. Abe, H. Takakura, and T. J. Sato. A stable binary quasicrystal. *Nature*, 408:537 – 538, 2000.

[36] S. Ranganathan and A. Inoue. An application of Pettifor structure maps for the identification of pseudo-binary quasicrystalline intermetallics. *Acta Materialia*, 54:3647 – 3656, 2006.

[37] J. Q. Guo and A. P. Tsai. Stable icosahedral quasicrystals in the Ag-In-Ca,Ag-In-Yb, Ag-In-Ca-Mg and Ag-In-Yb-Mg system. *Phil. Mag. Lett*, 82:349 – 352, 2002.

[38] Y. Muro, T. Sasakawa, T. Suemitsu, T. Takabatake, R. Tamura, and S. Takeuchi. Thermoelectric properties of binary Cd-Yb quasicrystals and Cd_6Yb. *Jpn. J. Appl. Phys.*, 41:3787 – 3790, 2002.

[39] Y. K. Kuo, K. M. Sivakumar, H. H. Lai, C. N. Ku, S. T. Lin, and A. B. Kaiser. Thermal and electrical transport properties of Ag-In-Yb quasicrystals: An experimental study. *Phys. Rev. B*, 72:054202, 2005.

[40] H. R. Sharma, M. Shimoda, K. Sagisaka, H. Takakura, J. A. Smerdon, P. J. Nugent, R. McGrath, D. Fujita, S. Ohhashi, and A. P. Tsai. Structure of the fivefold surface of the Ag-In-Yb icosahedral quasicrystal. *Phys. Rev. B*, 80:121401, 2009.

[41] H. R. Sharma, M. Shimoda, S. Ohhashi, and A. P. Tsai. First UHV surface studies of single-grain icosahedral Ag-In-Yb quasicrystal. *Phil. Mag.*, 87:2989 – 2994, 2007.

[42] Y. Ishii and T Fujiwara. Hybridization mechanism for cohesion of Cd-based quasicrystals. *Phys. Rev. Lett.*, 87:206408, 2001.

[43] K. Oura, A. V. Zotof, and A. A. Saranin. *Surface Science: An Introduction.* Springer-Verlag New York, LLC, 2003.

[44] C. J. Jenks and P. A. Thiel. Quasicrystals:A Short Review from a Surface Science Perspective. *Langmuir*, 14:1392 – 1397, 1998.

[45] J. Young Park, D. F. Ogletree, M. Salmeron, C. J. Jenks, P. A. Thiel, J. Brenner, and J. M. Dubois. Friction Anisotropy: A unique and intrinsic property of decagonal quasicrystals. *J. Mater. Res.*, 23:1488 – 1493, 2008.

[46] E. G. McRae, R. A. Malic, T. H. Lalonde, F. A. Thiel, H. S. Chen, and A. R. Kortan. Observation of Quasicrystal surface order and disordering by Low Energy Electron Diffraction. *Phys. Rev. Lett.*, 65:883 – 886, 1990.

[47] R. McGrath, J. Ledieu, and R. D. Diehl. A search for order: studies of clean quasicrystal surfaces and their use as templates for the formation of nanoscale aperiodic systems. *Prog. Surf. Sci.*, 75:131 – 145, 2004.

[48] E. Bauer and J. H. van der Merwe. Structure and growth of crystalline superlattices: From monolayer to superlattice. *Phys. Rev. B*, 33:3657 – 3671, 1986.

[49] C. Argile and G.E. Rhead. Adsorbed layer and thin film growth modes monitored by Auger Electron Spectroscopy. *Sur. Sci. Reports*, 10:277 – 356, 1989.

[50] M. Shimoda and H. R. Sharma. Sputter–induced crystalline layers and epitaxial overlayers on quasicrystal surfaces. *J. Phys.: Condens. Matter*, 20:310301 – 315208, 2008.

[51] A. Makhotkina, S. N. Yakunina, A. Yu. Seregina, D. S. Shaiturab, M. B. Tsetlinb, and E. Yu. Tereshchenkoa. Investigation of the Formation of Quasicrystalline $Al_{70}Pd_{20}Re_{10}$ Phase in situ during Annealing. *Crystallography Reports*, 56:871 – 874, 2011.

[52] H. R. Sharma, M. Shimoda, and A. P. Tsai. Quasicrystal surfaces: structure and growth of atomic overlayers. *Advances in Physics*, 56:403 – 464, 2007.

[53] J. A. Smerdon. The various modes of growth of metals on quasicrystals. *J. Phys.: Condens. Matter*, 22:433002, 2010.

[54] B. Bolliger, V. E. Dmitrienko, M. Erbudak, R. Luscher, and H.-U. Nissen. Epitactic textures of fcc Al on icosahedral Al-Pd-Mn quasicrystal. *Phys. Rev. B*, 3:052203, 2001.

[55] M. Shimoda, T. J. Sato, A. P. Tsai, and J. Q. Guo. Epitaxial crystalline film with pseudo-tenfold symmetry formed by Au-deposition on a decagonal $Al_{72}Ni_{12}Co_{16}$ quasicrystal. *Phys. Rev. B*, 62:11288 – 11291, 2000.

[56] V. Fournée, T. C. Cai, A. R. Ross, T. A. Lograsso, J. W. Evans, and P. A. Thiel. Nucleation and growth of Ag films on a quasicrystalline AlPdMn surface. *Phys. Rev. B*, 67:033406, 2003.

[57] M. Shimoda, T. J. Sato, A.-P. Tsai, and J.Q. Guo. Epitaxial film growth on a decagonal $Al_{72}Ni_{12}Co_{16}$ quasicrystal. *Surf. Sci.*, 507-510:276 – 280, 2002.

[58] M Shimoda, J Q Guo, T J Sato, and A P Tsai. Epitaxial film growth of Au-Al alloy on a quasiperiodic surface of icosahedral $Al_{72}Pd_{19.5}Mn_{8.5}$. *J. App. Phys.*, 40:6073 – 6076, 2001.

[59] M. Shimoda. Thin metal films on quasicrystalline surfaces. *Progress in Surface Science*, 75:87 – 108, 2004.

[60] T. C. Q. Noakes, P. Bailey, M. Draxler, C. F. McConville, A. R. Ross, T. A Lograsso, L. Leung, J. A. Smerdon, and R. McGrath. Film growth arising from the deposition of Au onto an i-Al-Pd-Mn quasicrystal: a medium energy ion scattering study. *J. Phys.: Condens. Matter*, 18:5017 – 5027, 2006.

[61] F. Hippert, P. Monod, R. Bellissent, and F. Vigneron. Magnetic properties of quasicrystals. *Journal de Physique*, 49:12, 1988.

[62] K. Saito, S. Matsuo, H. Nakano, T. Ishimasa, and M. Mori. Magnetic an electrical properties of a single-grained AlPdMn icosahedral Quasicrystal. *Journal of the physical society of Japan*, 63:1940 – 1947, 1994.

[63] R.A. Dunlap, R.C. O'Handley, M.E. McHenry, and V. Srinivas. Magnetic Properties of Quasicrystals: Effects of Disorder on Fe Magnetic Moment Formation. *Struct. Chem.*, 2:501 – 505, 1989.

[64] R. Lifshitz. Magnetic quasicrystals: what can we expect to see in their neutron diffraction data? *Materials Science and Engineering*, 294:508 – 511, 2000.

[65] Anuradha Jagannathan and Attila Szallas. Antiferromagnetism in two-dimensional quasicrystals. *Z. Kristallogr.*, 224:53 – 55, 2009.

[66] Y. Weisskopf, R. Luscher, and M. Erbudak. Structural modifications upon deposition of Fe on the icosahedral quasicrystal Al-Pd-Mn. *Surface Science*, 578:35 – 42, 2005.

[67] L.H. Wearing, J.A. Smerdon, L. Leung, T.A. Lograsso, A.R. Ross, and R. McGrath. Iron deposition on the five-fold surface of the icosahedral Al-Pd-Mn quasicrystal. *Surface Science*, 601:3450 – 3455, 2007.

[68] L.H. Wearing, J.A. Smerdon, L. Leung, T.A. Lograsso, A.R. Ross, and R. McGrath. Iron deposition on the tenfold surface of the $Al_{72}Ni_{11}Co_{17}$ decagonal quasicrystal. *J. Phys.: Condens. Matter*, 20:015005, 2008.

[69] S. Burkardt, M. Erbudak, J.-N. Longchamp, and Y. Weisskopf. Co nanocrystallites on an icosahedral Al-Pd-Mn quasicrystal. *Philos. Mag.*, 88:2111 – 2116, 2008.

[70] J. A. Smerdon, J. Ledieu, J. T. Hoeft, D. E. Reid, L. H. Wearing, R. D. Diehl, T. A. Lograsso, A. R. Ross, and R. McGrath. Adsorption of cobalt on the tenfold surface of *d*-$Al_{72}Ni_{11}Co_{17}$ and on the fivefold surface of i-$Al_{70}Pd_{21}Mn_9$. *Phil. Mag.*, 86:841 – 847, 2006.

[71] Y. Weisskopf, M. Erbudak, J.-N. Longchamp, and T. Michlmayr. Ni deposition on the pentagonal surface of an icosahedral AlPdMn quasicrystal. *Sur. Sci.*, 600:2594 – 2599, 2006.

[72] A. K. Shukla, R. S. Dhaka, S. W. D. Souza, M. Maniraj, S. R. Barman, K. Horn, Ph. Ebert, K. Urban, D. Wu, and T. A. Lograsso. Manganese adlayers on i-Al-Pd-Mn quasicrystal: growth and electronic structure. *J. Phys. Condens. Matter*, 21:405005, 2009.

[73] J. Ledieu, J. T. Hoeft, D. E. Reid, J. A. Smerdon, R. D. Diehl, N. Ferralis, T. A. Lograsso, A. R. Ross, and R. McGrath. Copper adsorption on the fivefold $Al_{70}Pd_{21}Mn_9$ quasicrystal surface. *Phys. Rev. B*, 72:035420, 2005.

[74] J. A. Smerdon, J. Ledieu, R. McGrath, T. C. Q. Noakes, P. Bailey, M. Draxler, C. F. McConville, T. A. Lograsso, and A. R. Ross. Characterization of aperiodic and periodic thin Cu films formed on the five-fold surface of i-Al_70Pd_21Mn_9 using medium-energy ion scattering spectroscopy. *Phys. Rev. B*, 74:035429, 2006.

[75] K. Pussi, M. Gierer, and R.D. Diehl. The uniaxially aperiodic structure of a thin Cu film on fivefold i-Al-Pd-Mn. *J. Phys. Condens. Matter*, 21:474213, 2009.

[76] K. J. Franke, H. R. Sharma, W. Theis, P. Gille, Ph. Ebert, and K. H. Rieder. Quasicrystalline Epitaxial Single Element Monolayers on Icosahedral Al-Pd-Mn and Decagonal Al-Ni-Co Quasicrystal Surfaces. *Phys. Rev Lett.*, 89:156104, 2002.

[77] J. Ledieu, L. Leung, L. H. Wearing, R. McGrath, T. A. Lograsso, D. Wu, and V. Fournée. Self-assembly, structure, and electronic properties of a quasiperiodic lead monolayer. *Phys. Rev. B*, 77:073409, 2008.

[78] J. Ledieu, M. Krajci, J. Hafner, L. Leung, L. H. Wearing, R. McGrath, T. A. Lograsso, D. Wu, and V. Fournée. Nucleation of Pb starfish clusters on the five-fold Al-Pd-Mn quasicrystal surface. *Phys. Rev. B*, 79:165430, 2009.

[79] M. Krajci, J. Hafner, J. Ledieu, V. Fournée, , and R. McGrath. Quasiperiodic Pb monolayer on the fivefold i-Al-Pd-Mn surface: Structure and electronic properties. *Phys. Rev. B*, 82:085417, 2010.

[80] J.A. Smerdon, L. Leung, J.K. Parle, C.J. Jenks, R. McGrath, V. Fournée, and J. Ledieu. Formation of a quasicrystalline Pb monolayer on the 10-fold surface of the decagonal AlNiCo quasicrystal. *Sur. Sci.*, 602:2496 – 2501, 2008.

[81] H. R. Sharma, M. Shimoda, A. R. Ross, T. A. Lograsso, and A. P. Tsai. Real-space observation of quasicrystalline Sn monolayer formed on the fivefold surface of icosahedral AlCuFe quasicrystal. *Phys. Rev. B*, 72:045428, 2005.

[82] A. K. Shukla, R. S. Dhaka, S. W. DeSouza, S. Singh, T. A. Lograsso D. Wu, M. Krajci, J. Hafner, K. Horn, and S. R. Barman. Quasiperiodic layers of free-electron metals studied using electron diffraction. *Phys. Rev. B*, 79:134206, 2009.

[83] H.R. Sharma, J.A. Smerdon, P.J. Nugent, M. Shimoda, H. Takakura, S. Ohhashi, A.P. Tsai, and R. McGrath. Quasicrystalline Pb film formed on the Fivefold Surface of a Primitive Type Icosahedral Quasicrystal. *to be published*.

[84] P.J. Nugent, V.R. Dhanak, M. Shimoda, C. Cui, R. McGrath, A. P. Tsai, and H. R. Sharma. Growth of the Sb thin film on the fivefold surface of the i-Ag-In-Yb quasicrystal. *to be published*.

[85] J. Ledieu, P. Unsworth, T.A. Lograsso, A.R. Ross, and R. McGrath. Ordering of Si atoms on the fivefold Al-Pd-Mn quasicrystal surface. *Phys. Rev B*, 73:012204, 2006.

[86] T. Cai, J. Ledieu, R. McGrath, V. Fourneé, T. Lograsso, A. Ross, and P. Thiel. Pseudomorphic starfish: nucleation of extrinsic metal atoms on a quasicrystalline substrate. *Surf. Sci.*, 526:115 – 120, 2003.

[87] R. McGrath, J. Ledieu, E.J. Cox, S. Haq, R.D. Diehl, C.J. Jenks, I. Fisher, A.R. Ross, and T.A. Lograsso. Quasicrystal surfaces: potential as templates for molecular adsorption. *J. Alloys and Compounds*, 342:432 – 436, 2002.

[88] W. Setyawan, R.D. Diehl, and S. Curtarolo. Structures and Topological Transitions of Hydrocarbon Films on Quasicrystalline Surfaces. *Phys. Rev. Lett.*, 102:055501, 2009.

[89] J. Ledieu, V.R. Dhanak, R.D. Diehl, T.A. Lograsso, D.W. Delaney, and R. McGrath. Sulphur adsorption on the five-fold surface of the *i*-$al_{70}pd_{21}mn_9$. *Surf. Sci.*, 512:77 – 83, 2002.

[90] J.T. Hoeft, J. Ledieu, S. Haq, T.A. Lograsso, A.R. Ross, and R. McGrath. Adsorption of benzene on the five-fold surface of the i-$Al_{70}Pd_{21}Mn_9$ quasicrystal. *Phil. Mag.*, 86:869 – 874, 2006.

[91] E.J. Cox, J. Ledieu, V.R. Dhanak, S.D. Barrett, C.J. Jenks, I. Fisher, and R. McGrath. An STM and SXPS study of the interaction of c60 with the ten-fold surface of the $Al_{72}Ni_{11}Co_{17}$ quasicrystal. *Surf. Sci.*, 566-568:1200 – 1205, 2004.

[92] P.J. Nugent, J.A. Smerdon, R. McGrath, C. Cui M. Shimoda, A.P. Tsai, and H.R. Sharma. Step-terrace morphology and reactivity to C_{60} of the five-fold icosahedral AgInYb quasicrystal. *Phil. Mag.*, 91:2862 – 2869, 2011.

[93] J. Ledieu, C. A. Muryn, G. Thornton, R. D. Diehl, T. A. Lograsso, D. W. Delaney, and R. McGrath. C_{60} adsorption on the quasicrystalline surface of $Al_{70}Pd_{21}Mn_9$. *Sur. Sci.*, 472:89 – 96, 2001.

[94] J.A. Smerdon, J.K. Parle, L.H. Wearing, L. Leung, T.A. Lograsso, A.R. Ross, and R. McGrath. C_{60} adsorption on an aperiodically modulated Cu surface. *Phys.: Conference Series*, 226:012006, 2010.

[95] P. von Rague Schleyer, M. Manoharan, H. Jiao, and F. Stahl. The Acenes: Is There a Relationship between Aromatic Stabilization and Reactivity? *Org. Lett.*, 3:3643 – 3646, 2001.

[96] G. Portella, J. Poater, J. M. Bofill, P. Alemany, and M. Sola. Local aromaticity of [n]Acenes, [n]Phenacenes, and [n]Helicenes (n) (1-9). *J. Org. Chem.*, 70:2509 – 2521, 2005.

[97] R.G. Endres, C.Y. Fong, L.H. Yang, G. Witte, and Ch. Wöll. Structural and electronic properties of pentacene molecule and molecular pentacene solid. *Computational Materials Science*, 29:362 – 370, 2004.

[98] T. Sekitani, U. Zschieschang, H. Klauk, and T. Someya. Flexible organic transistors and circuits with extreme bending stability. *Nature Materials*, 9:1015 – 1022, 2010.

[99] Z. Bao. Polymers for Microelectronics and Nanoelectronics. 874:1 – 14, 2004.

[100] C. L. Fan, T. H. Yang, and C. Y. Chiang. Performance Degradation of Pentacene-Based Organic Thin-Film Transistors Under Positive Drain Bias Stress in the Atmosphere. *IEEE Electron Device Letters*, 31:887 – 889, 2010.

[101] L. Fumagalli, M. Binda, I. Suarez Lopez, D. Natali, M. Sampietro, S. Ferrari, L. Lamagna, and M. Fanciull. Multi layer structure for encapsulation of organic transistors. *Organic Electronics*, 10:692 – 695, 2009.

[102] F.-J. Meyer zu Heringdorf, M.C. Reuter, and R.M. Tromp. The nucleation of pentacene thin films. *Appl. Phys. A*, 78:787 – 791, 2004.

[103] H. Klauk, M. Halik, U. Zschieschang, F. Eder, G. Schmid, and C. Dehm. Pentacene organic transistors and ring oscillators on glass and on flexible polymeric substrates. *App. Phys. Lett.*, 82:4175, 2003.

[104] P. G. Schroeder, C. B. France, J. B. Park, and B. A. Parkinson. Energy level alignment and two-dimensional structure of pentacene on Au(111) surfaces. *J. App. Phys.*, 91:3010 – 3014, 2002.

[105] V. Corradini, C. Menozzi, M. Cavallini, F. Biscarini, M. Grazia Betti, and C. Mariani. Growth morphology and electronic structure of 2D ordered pentacene on the Au(110)-(1 × 2) surface. *Sur. Sci.*, 532 - 535:249 – 254, 2003.

[106] K. Lee and J. Yu. Ab initio study of pentacene on Au(001) surface. *Surface Science*, 589:8 – 18, 2005.

[107] E. Mete, I. Demiroğlu, M. Fatih Danişman, and Şinasi Ellialtoğlu. Pentacene multilayers on Ag(111) surface. *J. Phys. Chem. C*, 114:2724 2729, 2010.

[108] M. Simeoni, S. Picozzi, and B. Delley. An ab-initio study of pentacene on aluminum (1 0 0) surface. *Sur. Sci.*, 562:43 – 52, 2004.

[109] X. Sun, T. Suzuki, Y. Yamauch, M. Kurahash, Z.P. Wang, and S. Entani. Ab initio study of pentacene on the Fe(100) surface. *Surface Science*, 602:1191 – 1198, 2008.

[110] S. Lukas, G. Witte, and Ch. Wöll. Novel Mechanism for Molecular Self-Assembly on Metal Substrates: Unidirectional Rows of Pentacene on Cu(110) Produced by a Substrate-Mediated Repulsion. *Phys. Rev. Lett.*, 88:028301, 2002.

[111] J. Lagoute, K. Kanisawa, and S. Fölsch. Manipulation and adsorption-site mapping of single pentacene molecules on Cu(111). *Phys. Rev. B*, 70:245415, 2004.

[112] K. S. Yong, Y. P. Zhang, S. W. Yang, P. Wu, and G. Q. Xu. Chemisorption of pentacene on Si(111)-7 × 7 studied via Scanning Tunneling Microscopy and Density Functional Theory. *J. Phys. Chem. C*, 111:4285 – 4293, 2007.

[113] H.W. Liu, A.Al-Mahboob, Y.Fujikawa, N.Fukui, T.Hitosugi, T. Hashizume, Q.K.Xue, and T.Sakurai. Pentacene growth on graphite investigated by low-energy electron microscope. *Journal of Crystal Growth*, 312:967 – 970, 2010.

[114] J. Smerdon, M. Bode, N. Guisinger, and J. Guest. Monolayer and bilayer pentacene on Cu(111). *Phys. Rev. B*, 84:5436, 2011.

[115] T. Schwieger, X. Liu, D. Olligs, M. Knupfer, and Th. Schmidt. Orientation and electronic properties of pentacene molecules on SiO_2 and GeS(0001) studied using x-ray absorption spectroscopy. *J. App. Phys.*, 96:5596 – 5600, 2004.

[116] J. Filo and M. Putala. Semiconducting Organic Molecular Materials. *J. Electrical Engineering*, 61:314 – 320, 2010.

[117] S. Kobayash, T. Takenobu, A Fujiwara S Mor and, and Y Iwasa. C_{60} thin-film transistors with high field-effect mobility, fabricated by molecular beam deposition. *Sci. and Tech. of Adv. Mat.*, 4:371 – 375, 2003.

[118] J. I. Pascual, J. Gómez-Herrero, D. Sánchez-Portal, and H.-P. Rust. Vibrational spectroscopy on single C_{60} molecules: The role of molecular orientation. *J. Chem. Phys.*, 117:9531 – 9534, 2002.

[119] P. W. Murray, M. Ø . Pedersen, E. Lægsgaard, I. Stensgaard, and F. Besenbacher. Growth of C_{60} on Cu(110) and Ni(110) surfaces: C_{60} -induced interfacial roughening. *Phys. Rev B*, 55:9360 – 9363, 1997.

[120] K.i Iizumi, K. Saiki, and A. Koma. Investigation of the interaction between a C_{60} epitaxial film and a Si(111)-7 $\times$ 7 surface by electron energy loss spectroscopy. *Surf. Sci.*, 518:126 – 132, 2002.

[121] G. K. Wertheim and D. N. E. Buchanan. Interfacial reaction of C_{60} with silver. *Phys. Rev. B*, 50:11070 – 11073, 1994.

[122] M. Pedio, M.L. Grilli, C. Ottaviani, M. Capozi, C. Quaresima, P. Perfetti, P. A. Thiry, R. Caudano, and P.Rudolf. Inverse photoemission studies of C_{60} on Au(110). *Journal of Electron Spectroscopy and Related Phenomena*, 76:405 – 409, 1995.

[123] C. Cepek, A. Goldoni, and S. Modesti. Chemisorption and fragmentation of C_{60} on Pt(111) and Ni(110). *Phys. Rev. B*, 53:7466 – 7472, 1996.

[124] A. J. Maxwell, P. A. Brühwiler, D. Arvanitis, J. Hasselstroöm, M. K.-J. Johansson, and N. Martensson. Electronic and geometric structure of C_{60} on Al(111) and Al(110). *Phys. Rev. B*, 57:.7312 – 7326, 1998.

[125] J.T. Sadowski, R.Z. Bakhtizin, A.I. Oreshkin, T. Nishihara, A. Al-Mahboob, Y. Fujikawa, K. Nakajima, and T. Sakurai. Epitaxial C_{60} thin films on Bi(0001). *Surf. Sci.*, 601:136 – 139, 2007.

[126] Kurt J. Lesker and Company. Turbomolecular Pumps and Drag Pumps: Technical Notes. http://www.lesker.com.

[127] D. P. Woodruff and T. A. Delchar. *Modern techniques of surface science - second edition*. Cambridge University Press, 1994.

[128] CasaXPS. www.casaxps.com.

[129] R. D. Diehl, J. Ledieu, N. Ferralis, A. W. Szmodis, and R. McGrath. Low-energy electron diffraction from quasicrystal surfaces. *J. Phys.: Condens. Matter*, 15:63 – 81, 2003.

[130] J. C. A. Huang. Self-assembly nanostructures probed by scanning tunneling microscopy. *Appl. Phys. Lett.*, 89:221915–221917, 2006.

[131] G. Binnig and D. P. E. Smith. Single tube three dimensional scanner for scanning tunneling microscopy. *Rev. Sci. Instrum.*, 57:1688 – 1689, 1986.

[132] A. R. Kortan, R. S. Becker, F. A. Thiel, and H. S. Chen. Real-Space Atomic Structure of a Two-Dimensional Decagonal Quasicrystal. *Phys. Rev. Lett.*, 64:200 – 203, 1990.

[133] H. R. Trebin. *Quasicrystals: Structure and Physical Properties*. John Wiley and Sons, 2006.

[134] J. A. Smerdon, J. K. Parle, L. H. Wearing, T. A. Lograsso, A. R. Ross, and R. McGrath. Nucleation and growth of a quasicrystalline monolayer: Bi adsorption on the five-fold surface of i-$Al_{70}Pd_{21}Mn_9$. *Phys. Rev. B*, 78:075407, 2008.

[135] H. R. Sharma, V. Fournée, M. Shimoda, A. R. Ross, T. A. Lograsso, P. Gille, and A. P. Tsai. Growth of Bi thin films on quasicrystal surfaces. *Phys. Rev. B*, 78:155416, 2008.

[136] V Fournée and P A Thiel. New phenomena in epitaxial growth: solid films on quasicrystalline substrates. *J. Phys. D: Appl. Phys.*, 38:83 – 106, 2005.

[137] J. F. Moulder. *Handbook of x-ray photoelectron spectroscopy.* ULVAC-PHI, 1995.

[138] S. Doniach. Many-Electron Theory of Nondirect Transitions in the Optical and Photoemission Spectra of Metals. *Phys. Rev. B*, 2:3898 – 3905, 1970.

[139] P. Klapetek, D. Necas, and C. Anderson. Gwyddion http://gwyddion.net/, 2009 – 2011.

[140] J. A. Smerdon, J. K. Parle, L. H. Wearing, T. A. Lograsso, A. R. Ross, and R. McGrath. Nucleation and growth of pseudomorphic monolayers on quasicrystal surfaces. *J. Phys.: Condens. Matter*, 20:314005, 2008.

[141] Thomas M. Schaub, Daniel E. Bürgler, H. J. Güntherodt, and J. B. Suck. Investigation of the icosahedral quasicrystal $Al_{68}Pd_{23}Mn_9$ by LEED and STM. *Z. Phys. B*, 96:93 – 96, 1994.

[142] T. Nagao, J. T. Sadowski, M. Saito, S. Yaginuma, Y. Fujikawa, T. Kogure, T. Ohno, Y. Hasegawa, S. Hasegawa, and T. Sakurai. Nanofilm Allotrope and Phase Transformation of Ultrathin Bi film on Si(111)-7 $\times$ 7. *Phys. Rev. Lett.*, 93:105501, 2004.

[143] P. Hofmann. The surfaces of Bi: structural and electronic properties,. *Prog. Surf. Sci.*, 81:191 – 245, 2006.

[144] Fournée V, Ross A. R, Lograsso T. A., Thiel P. A., Y. Ishii ed .E Belin-Ferré, M. Feuerbacher, and D. J. Sordelet (Warrendale: Materials Research Society. Quasicrystals 2003- Preparation, Properties and Applications. *Materials Research Society Symp. Proc.*, 805:281 – 6, 2004.

[145] N. Ferralis, K. Pussi, E. J. Cox, M. Gierer, J. Ledieu, I. R. Fisher, C. J. Jenks, M. Lindroos, R. McGrath, and R. D. Diehl). Structure of the tenfold *d*-Al-Ni-Co quasicrystal surface. *Phys. Rev. B*, 69:153404, 2004.

[146] S. A. Scott, M. V. Kral, and S. A. Brown. A crystallographic orientation transition and early stage growth characteristics of thin Bi films on HOPG. *Surf. Sci.*, 587:175 – 184, 2005.

[147] T. Suzuki, S. Picozzi, and B. Delley. The chemisorption of pentacene on Si(001)- 2 $\times$ 1. *Surf. Sci.*, 600:5092 – 5103, 2006.

[148] J. Z. Wang, J. T. Sadowski, Z. H. Xiong, Y. Fujikawa, Q. K. Xue, and T. Sakurai. Comparative studies of pentacene and perfluoropentacene grown on a Bi(0001) surface. *Nanotechnology*, 20:95704, 2009.

[149] C. B. France, P. G. Schroeder, and B. A. Parkinson. Direct observation of a widely spaced periodic row structure at the pentacene/Au(111) interface using scanning tunneling microscopy. *Nano. Letters*, 2:693 – 696, 2002.

[150] J. A. Smerdon, N. Cross, V. R. Dhanak, H. R. Sharma, K. M. Young, T. A. Lograsso, A. R. Ross, and R. McGrath. Structure and reactivity of Bi allotropes on the fivefold icosahedral AlPdMn quasicrystal surface. *J. Phys.: Condens. Matter*, 22:345002, 2010.

[151] C. Morin, D. Simon, and P. Sautet. Trends in the Chemisorption of Aromatic Molecules on a Pt(111) Surface: Benzene, Naphthalene, and Anthracene from First Principles Calculations. *J. Phys. Chem. B*, 108:12084 – 12091, 2004.

[152] C. Morin, D. Simon, and P. Sautet. Chemisorption of Benzene on Pt(111), Pd(111), and Rh(111) Metal Surfaces: A Structural and Vibrational Comparison from First Principles. *J. Phys. Chem. B*, 108:5653 – 5665, 2004.

[153] G. Kresse and J. Hafner. Norm-conserving and ultrasoft pseudopotentials for first-row and transition elements. *J. Phys. Condens. Matter*, 6:8245 – 8257, 1994.

[154] G. Kresse and J. Joubert. From ultrasoft pseudopotentials to the projector augmented-wave method. *Phys. Rev. B*, 59:1758 – 1775, 1999.

[155] P.E. Blöchl. Projector augmented-wave method. *Phys. Rev. B*, 50:17953 – 17979, 1994.

[156] V. Fournée, J. Ledieu, T. Cai, and P. A. Thiel. Influence of strain in Ag on Al(111) and Al on Ag(100) thin film growth. *Phys. Rev. B*, 67:155401, 2003.

[157] L. Gavioli, M. Fanetti, M. Sancrotti, and M. G. Betti. Long-range-ordered pentacene chains assembled on the Cu(119) vicinal surface. *Phys. Rev. B*, 72:1 – 5, 2005.

[158] J. Götzen, S. Lukas, A. Birkner, and G. Witte. Absence of template induced ordering in organic multilayers: The growth of pentacene on a Cu(221) vicinal surface. *Sur. Sci.*, 605:577 – 581, 2011.

[159] H.R. Sharma et al. To be published.

[160] V. Fournée, H. R. Sharma, M. Shimoda, A. P. Tsai, B. Unal, A. R. Ross, T. A. Lograsso, , and P. A. Thiel. Quantum Size Effects in Metal Thin Films Grown on Quasicrystalline Substrates. *Phys. Rev. Lett.*, 95:155504, 2005.

[161] K. Nozawa and Y.i Ishii. Theoretical studies on clean and adsorbed surfaces of Ag-In-Yb. *Phil. Mag.*, 91:2913 – 2919, 2010.

[162] I. Markov. Kinetics of surfactant-mediated epitaxial growth. *Phys. Rev. B*, 50:11271 – 11274, 1994.

[163] M. Copel, M. C. Reuter, E. Kaxiras, and R. M. Tromp. Surfactants in Epitaxial Growth. *Phys. Rev. B*, 63:632 – 635, 1989.

[164] C. T. Horng and R. W. Vook. The initial epitaxy of Cu on (111) Ag films. *J. Vac. Sci. Technol.*, 11:140 – 143, 1974.

[165] M. J. Gibson and P. J. Dobson. Observations of the epitaxial growth of nickel and copper on (111) silver. *J. Phys. F: Metal Phys.*, 5:864 – 872, 1975.

[166] H.R. Sharma, M. Shimoda, V. Fournée, A.R. Ross, T.A. Lograsso, and A.P. Tsai. First steps in the growth of Cu thin films on the five-fold surface of the icosahedral Al-Cu-Fe quasicrystal. *App. Surf. Sci.*, 241:256 – 260, 2005.

[167] K. Pussi, M. Gierer, and R. D. Diehl. The uniaxially aperiodic structure of a thin Cu film on fivefold*i*-Al-Pd-Mn. *J. Phys.: Condens. Matter*, 21:474213, 2009.

[168] P. J. Nugent, G. Simutis, V. R. Dhanak, R. McGrath, M. Shimoda, C. Cui, A. P. Tsai, and H. R. Sharma. Surface oxidation of the icosahedral Ag-In-Yb quasicrystal. *Phys. Rev. B*, 82:014201, 2010.

[169] M. Pedio, B. Doyle, N. Mahn, A. Giglia, F. Borgatti, S. Nannarone, S. K. M. Henze, R. Temirov, F.S. Tautz, L. Casalis, R. Hudej, M. F. Danisman, and B. Nickel. Growth of pentacene on Ag(111) surface: A NEXAFS study. *Applied Surface Science*, 254:103 – 107, 2007.

[170] M. Eremtchenko, R. Temirov, D. Bauer, J. A. Schaefer, and F. S. Tautz. Formation of molecular order on a disordered interface layer: Pentacene/Ag(111). *Phys. Rev. B*, 72:115430, 2005.

Project Publications

◇ "Structure and reactivity of Bi allotropes on the fivefold icosahedral AlPdMn quasicrystal surface" J. A. Smerdon, N. Cross, V. R. Dhanak, H. R. Sharma, K. M. Young, T. A. Lograsso, A. R. Ross and R McGrath J. Phys.: Condens. Matter 22 345002 (2010)

◇ "XPS study of adsorption and desorption of a Bi thin film on the five-fold icosahedral Al-Pd-Mn surface" K. M. Young; N. Cross; J. A. Smerdon; V. R. Dhanak; H. R. Sharma; T. A. Lograsso; A. R. Ross; R. McGrath Philosophical Magazine 1478-6435 (2011)

◇ "Scanning tunneling microscopy study of Pn adsorption on aperiodic surfaces" K.M. Young, H.R. Sharma, R. McGrath, J.A. Smerdon, M. Lahti and K. Pussi" (In preparation.)

◇ "Pentacene growth on *i*-AgInYb: An epitaxial, quasiperiodic molecular overlayer" K. Young, J. Smerdon, H. R. Sharma, C. Cui A-. P. Tsai and R. McGrath (In preparation.)

◇ "Various Bi Allotropes Formed on Quasicrystal Surfaces: Templates for Adsorption of C_{60} and Pentacene Molecules" H. R. Sharma, J. A. Smerdon, K. Young and R. McGrath J. Phys.: Condens. Matter (Submitted.)

Other Publications

◇ "Surface characterization of polygrain icosahedral $Al_{70.5}Pd_{21}Re_{8.5}$ quasicrystal by XPS, UPS and STM" R. Tamura, I. M. McLeod, D. Hesp, V. R. Dhanak, T. Nakamura, K. Nishio, K M Young, R. McGrath, H. R. Sharma (Submitted.)

Oral Presentations

◇ CMA Network of Excellence virtual laboratory surfaces meeting 2009 "Characterisation of Bismuth Thin Film Growth On Quasicrystalline AlPdMn"

◇ CMAC Network of Excellence conference 2010 "Adsorption of pentacene on aperiodic surfaces"

◇ CMAC Network of Excellence conference 2011. "Adsorption of pentacene on quasi-periodic surfaces"

◇ CMMP conference 2011 “Epitaxial growth of pentacene on quasi-periodic substrates”

Poster Presentations

◇ Aperiodic ’09 International Conference “Characterisation of Bi growth on the Quasicrystal *i*-AlPdMn”

◇ ICQ11 International Conference “Structure and Stability of Bi Thin Films on the Five-Fold Surface of the Icohsahedral Al-Pd-Mn Quasicrystal”

◇ ISSC IOP Conference 2011 “Pentacene adsorption on quasiperiodic surfaces”

◇ IUCr Congress 2011 “Adsorption of pentacene on quasi-periodic surfaces”